Modelling, Control, and Planning of Microgrids for Power Quality Assurance

by

Ameen Hassan Yazdavar

A thesis
presented to the University of Waterloo
in fulfillment of the
thesis requirement for the degree of
Doctor of Philosophy
in
Electrical and Computer Engineering

Waterloo, Ontario, Canada, 2020

Examining Committee Membership

The following served on the Examining Committee for this thesis. The decision of the Examining Committee is by majority vote.

External Examiner:	Mohammad Shahidehpour Professor, Dept. of Electrical & Computer Engineering, Illinois Institute of Technology
Supervisor(s):	Ehab El-Saadany Professor, Dept. of Electrical & Computer Engineering, Magdy Salama Professor, Dept. of Electrical & Computer Engineering, University of Waterloo
Internal Member:	Mehrdad Kazerani Professor, Dept. of Electrical & Computer Engineering, University of Waterloo
Internal Member:	Ramadan El-Shatshat Professor, Dept. of Electrical & Computer Engineering, University of Waterloo
Internal-External Member:	Jatin Nathwani Professor, Dept. of Civil and Environmental Engineering, University of Waterloo

I hereby declare that I am the sole author of this thesis. This is a true copy of the thesis, including any required final revisions, as accepted by my examiners.

I understand that my thesis may be made electronically available to the public.

Abstract

This thesis considers power quality improvement for microgrids penetrated with nonlinear loads at two levels: 1) at the device level, which is carried out through the distributed generators' (DGs') controllers on a decentralized basis; and 2) at the system level, in the microgrid planning, taking into account the specific features of microgrids, including the lack of a slack bus, droop-based operation of some DGs, and necessity of voltage support provision. Moreover, given that modelling is an inherent part of power quality studies, the thesis focuses on modelling at two levels: 1) at the device level, in the modelling of nonlinear loads and generators that are commonly used in microgrids; and 2) at the system level, in developing a harmonic power flow algorithm suitable for islanded microgrids to quantify the flow of harmonics as well as voltage distortions.

One of the microgrid basic control objectives is to uniformly distribute the loads among different the DGs. For nonlinear loads, their non-fundamental powers should also be evenly shared along with active and reactive powers. The sharing of nonlinear loads among the DGs is always a trade-off between accuracy and voltage quality. The first research point considers a virtual harmonic conductance for each harmonic, as a family of droop characteristics in terms of conductance versus current. Assigning a variable conductance for each harmonic current improves DGs' controllability, thus offering accurate nonlinear load sharing, which is crucial at the near-rated loading, in addition to enhancing the voltage quality. The proposed method also unveils a tuning methodology for the droop characteristics that sets a maximum permissible value for each individual harmonic to comply with international standards. Lastly, a hybrid voltage and current control system is suggested to accurately track the DGs' harmonic conductances designated by the proposed droop characteristics. While the proposed algorithm is capable of accurately distributing common nonlinear loads among DGs, it also enjoys the advantage of supplying local nonlinear loads by their dedicated DGs.

As the second research point, the thesis presents a planning platform that simultaneously determines the locations and sizes of DGs and capacitor banks (CBs) for isolated microgrids with a high penetration of nonlinear loads. The proliferation of nonlinear loads along with the capacitors of CBs or DGs' output filters that are distributed throughout microgrids may cause quasi-resonance and severe voltage distortions. Because these issues are affected by the locations and sizes of DGs and CBs, a harmonic analysis should be considered in the planning. For that purpose, a harmonic power flow tool tailored for planning applications is developed that takes into consideration the specific features of isolated microgrids. Given the necessity of supply continuity for isolated microgrids following a contingency, and the fact that frequency and voltage provision cannot be provided by

renewable DGs, a reliability constraint has been added to the planning algorithm. This constraint increases the probability of building successful islands, and results in a better distribution of dispatchable DGs throughout microgrids.

Developing an effective harmonic power flow tool requires fast and accurate calculations of the harmonics generated by nonlinear elements. As the third research point, the thesis presents a time domain-based method for obtaining all steady-state characteristic and non-characteristic harmonics generated by three-phase diode bridge rectifiers, under unbalanced and distorted supply. The developed model is generic and able to address both continuous- and discontinuous-conduction modes with a single formulation. By introducing a virtual resistance on the rectifier's DC side, the model is extended to accommodate any DC-side filter. Further, a unique analytical Jacobian matrix is developed to guarantee a quadratic convergence for the iterative part of the proposed method. The effectiveness of the proposed method for harmonic analysis is confirmed through a comparative evaluation with time-domain simulations using PSCAD/EMTDC.

As the fourth research point, the thesis proposes an accurate harmonic power flow algorithm for islanded microgrids, taking into account their specific features, i.e., the droop-based operation of DGs, lack of a slack bus and the fact that islanded microgrids are based on voltage-controlled DGs. The algorithm is a sequential one that repeats fundamental and harmonic power flow algorithms in sequence until convergence is achieved. The fundamental power flow takes into account the fact that islanded microgrids are formed based on voltage-controlled DGs, as well as the droop-based operation of these DGs. On the other hand, the harmonic power flow is based on Nodal analysis in which the microgrid's nonlinear loads constitute its current source vector and the rest of the elements are modelled within its admittance matrix. The model used for nonlinear loads considers the mutual interactions of different harmonics. The model for voltage-source-converter interfaced DGs is based on a transfer function technique, and allows incorporating different control layers. The effectiveness of the control algorithm has been proven through comparative studies with time domain simulations.

Acknowledgements

First and foremost, I would like to thank Allah, the most gracious, the most merciful, whose guidance lead me this far.

I would like to express my sincere gratitude to my supervisors, Prof. Ehab El-Saadany and Prof. Magdy Salama, for their continuous support, insightful discussions and constructive feedback throughout my Ph.D. studies. I am truly honored that I have been supervised by them.

My appreciation and thanks are also offered to my Ph.D. committee members: Prof. Mehrdad Kazerani, Prof. Ramadan El-Shatshat, and Prof. Jatin Nathwani from University of Waterloo and Prof. Mohammad Shahidehpour from Illinois Institute of Technology, for their invaluable comments and feedback on my research.

During my Ph.D., I constantly received the excellent guidance and advice of Dr. Maher Azzouz. He is a perfect mentor, and I would like to express my gratitude to him.

My respect and appreciation are also extended to my friends and colleagues, Dr. Abdelsalam Eajal, Dr. Amir Ameli, soon-to-be-Dr. Aram Kirakosyan, Dr. Haytham Abdelrahman, and Dr. Mostafa Shaaban, with whom I had the pleasure of fruitful and constructive technical discussions.

My family always receive my deepest gratitude and eternal love. My special gratitude and love goes to my dearest parents, Reza and Zohreh, my beloved wife Tahereh, my darling daughter Tasnim, my sister Fatemeh, and my brother Hossein, for all their endless love, support, and encouragement.

Dedication

To my dearest parents, Reza and Zohreh;
to my beloved wife, Tahereh;
to my darling daughter, Tasnim;
to my sister, Fatemeh;
and to my brother, Hossein;
in recognition of your endless love, support, and encouragement.

Table of Contents

List of Tables

List of Figures

Nomenclature

Control

$S_{N,i}$	Non-fundamental apparent power for the i^{th} DG.
$S_{N,i}^{req}$	The required non-fundamental power to be supplied by the i^{th} DG.
$\Delta S_{N,i}$	The sharing error of non-fundamental apparent power for the i^{th} DG.
$\Delta S_{N,i,j}$	The non-fundamental power sharing error between the i^{th} and j^{th} DGs.
$\omega_{cut,h}$	The cutoff bandwidth of a proportional-resonant controller.
K_{pv}, K_{rh}	The proportional and resonant gains of a proportional-resonant controller.
H	Signal decomposer transfer function.
H_{gain}	The adaptive gain of current limiter.
$G_{DG,i,h}^{max}, G_{DG,i,h}^{min}$	The maximum and minimum harmonic conductance of the i^{th} DG at the h^{th} order harmonic.
$R_{DG,i,h}^{max}$	The maximum attainable value for each harmonic resistance.
$V_{DG,i,h}^{max}, I_{DG,i,h}^{max}$	The maximum harmonic voltage and current limits.
$I_{sys,h}^{max}$	The maximum system demanding value for the h^{th} order harmonic current.

$I_{std,j,h}$	The upper current limit of the j^{th} load feeder for the h^{th} order harmonic.
$I_{rated,load,j}$	The rated current of the j^{th} load feeder.
$I_{oi,h}$	The h^{th} order harmonic current of the i^{th} DG.
k	The system nonlinear loading factor.
$Z_{net,h}, Z_{feeder,i,h}$	Network harmonic impedance and feeder impedance.
$Z_{DG,i,h}$	The h^{th} order harmonic impedance of the i^{th} DG.
$R_{feeder,i}, L_{feeder,i}$	Feeder impedance components.
R_{v1}, L_{v1}	The virtual resistance and inductance at the fundamental frequency.
n	The number of load feeders.
$V_{oi,1}$	The fundamental voltage of the i^{th} DG.
$V_{pcc,1}$	The fundamental component of the PCC voltage.
V_0, V^*	The nominal and DG reference voltage amplitudes.
ω_0, ω^*	The nominal and reference angular frequencies.
P_{av}, Q_{av}	DG supplied active and reactive powers.
D_p, D_q	The droop coefficients.
ω_c	The cutoff frequency of the low-pass filter used to calculate the average values of active and reactive powers.
$i^*_{o\alpha\beta,H}, i^{**}_{o\alpha\beta,H}$	The reference values for total harmonic currents before and after the current limiter.
PCC	Point of common coupling.
THD_{PCC}	The voltage THD at the PCC.
R_{sce}	Short circuit ratio.
$MSOGI$	Multiple second-order generalized integrators.

FLL	Frequency-locked loop.

Planning

b	Index for bus.
s_g, s_l, s_c	Indices for generation, load, and configuration states.
s_g, s_l, s_c	Indices for generation, load, and configuration states.
s	Index for combined states of wind-power generation and load.
s^R	Index for combined states of generation-load-network model.
s^M	Index for state corresponding to maximum wind-power generation and load.
bk	Index for feeder between buses b and k.
y, day, hr	Indices for year, day, and hour.
t	Index for time $[y, day, hr]$.
db, wb, cb	Indices for candidate buses of diesel generators, wind turbines and capacitor banks.
dr, wr, cr	Indices for available ratings of diesel generators, wind turbines and capacitor banks.
$\mathcal{S}^B$	Set of all buses.
$\mathcal{S}^{IB}$	Set of buses in an island.
$\mathcal{S}^C$	Set of all system configurations.
$\mathcal{S}^S$	Set of system states.
$\mathcal{S}^{DB}, \mathcal{S}^{WB}, \mathcal{S}^{CB}$	Sets of candidate buses for diesel generators, wind turbines, and capacitor banks.
$\mathcal{S}^{DR}, \mathcal{S}^{WR}, \mathcal{S}^{CR}$	Sets of available ratings for diesel generators, wind turbines, and capacitor banks.
$\mathcal{S}^G, \mathcal{S}^L, \mathcal{S}^C$	Sets of system generation, load, and configuration states.

$C^C_{dr}, C^C_{wr}, C^C_{cr}$	Capital costs of diesel generators, wind turbines, and capacitor banks.
M^C_{dr}, M^C_{wr}	Maintenance costs of diesel generators and wind turbines.
F^C	Fuel cost.
H^R	Heat rate.
K^P	Allowed penetration for renewable DGs
$P^{max}_{dr}, P^{min}_{dr}$	Max. and min. active power limits of diesel generator dr.
Q^{max}_{dr}	Max. reactive power limit of diesel generator dr.
m^P_{dr}	$\omega - P$ droop gain of diesel generator dr.
m^Q_{dr}	$V - Q$ droop gain of diesel generator dr.
S_{dr}, S_{cb}	Ratings of diesel generator dr and capacitor bank cb.
$\Delta\omega^{per}$	Permissible frequency drop.
ΔV^{per}	Permissible voltage drop.
ω^{nom}, V^{nom}	Nominal frequency and voltage.
V^{max}, V^{min}	Permissible bus max. and min. voltages.
$LOLE^U$	Upper limit for $LOLE$.
N^B	Number of buses.
$\Pr_s$	Probability of state s.
$THD^{V,U}, IH^{V,U}$	Upper limits for voltage THD and IH.
$P_{wr,t,s}$	Power injected by wind turbine wr, at time t for state s.
$P_{dr,t,s}, Q_{dr,t,s}$	Active and reactive powers of diesel generator dr, at time t for state s.
$P^I_{b,t,s}, Q^I_{b,t,s}$	Active and reactive powers injected by network into bus b, at time t for state s.

$P^L_{b,t,s}, Q^L_{b,t,s}$	Active and reactive powers of bus b load, at time t for state s.
$LOLE$	Loss of load expectation.
V, δ	Bus voltage magnitude and phase angle.
Y_{bk}, θ_{bk}	Admittance magnitude and angle between buses b and k.
$x_{db,dr}$	Binary variable for installing diesel generator dr at candidate bus db.
$x_{wb,wr}$	Binary variable for installing wind turbine wr at candidate bus wb.
$x_{cb,cr}$	Binary variable for installing capacitor bank cr at candidate bus cb.
$y_{cb,cr,s}$	Binary variable for switching capacitor bank cr at candidate bus cb for state s.
$THD^V_{b,t,s}, IH^V_{b,t,s}$	THD^V and IH^V of bus b, at time t for state s.
$\mathbf{P^L}, \mathbf{Q^L}$	The vectors of load active and reactive powers.
$\tilde{\mathbf{V}}_\mathbf{1}, \tilde{\mathrm{I}}_\mathbf{1}$	The vectors of fundamental voltage and current phasors.
ω	System frequency.
$I_{h,spec}, \theta_{h,spec}$	The magnitude and phase angle of the h^{th} harmonic order obtained from the nonlinear loads' database.
I_1, θ_1	The magnitude and phase angle of the fundamental current phasor.
$\tilde{\mathrm{I}}_\mathbf{h}$	The vector of harmonic current phasor.
$\tilde{\mathbf{Y}}_\mathbf{h}$	The harmonic bus admittance matrix at different harmonic orders.
Re, Im	Operators returning the real and imaginary parts.
$V_{b,1}$	The voltage magnitude of bus b obtained from the fundamental power flow.
$DFIG$	Doubly fed induction generator.
GSC	Grid side converter.

G_{PI}	Transfer function of a PI controller.
F	Feed-forward gain.
RSC	Rotor side converter.
ω_r	Rotor speed.
$X, f_X(x)$	Random variable and its probability density function.
$\mathbf{F}$	Vector including power mismatch equations for all buses.
$\mathcal{X}^{\mathbf{PF}}$	Vector comprising magnitudes and angles of bus voltages as well as the network frequency.

Modelling-1

$\mathbf{\Delta}$	Vector containing η_i and γ_i angles.
$\mathbf{J}$	The Jacobian matrix.
DCM, CCM	Discontinuous and continuous conduction modes.
f_i, g_i	Mismatch equations giving switching instants.
p_h, q_h	Coefficients of a fictitious differential equation returning a harmonic.
R_{inf}	A large virtual resistance introduced at the rectifier output.
V_h, ϕ_h	The magnitude and phase angle of the h^{th} order harmonic of the supply voltage.
$\tilde{\mathbf{X}}$	Augmented state-space vector.
$\mathbf{X}$	The state-space vector.
$\gamma_i, \gamma_i + \eta_i$	Switching instants.
R_{on}, R_{off}	Resistors represent a diode being on and off in the piecewise linear model.
$\mathbf{A}^{\mathbf{cir,cir}}_{\mathbf{on,i}}, \mathbf{A}^{\mathbf{cir,cir}}_{\mathbf{off,i}}$	Matrices relating the circuit state variables together for on and off modes.

$\mathbf{A}^{\mathbf{cir,sup}}_{\mathbf{on,i}}, \mathbf{A}^{\mathbf{cir,sup}}_{\mathbf{off,i}}$	Matrices relating the circuit state variables to supply state variables for on and off modes.
$\mathbf{A}^{\mathbf{har,har}}$	Matrix relating the harmonic state variables together.
$\mathbf{A}^{\mathbf{sup,sup}}$	Matrix relating the supply state variables together.
$\mathbf{A_{on,i}}, \mathbf{A_{off,i}}$	State transition matrices.
$\mathbf{C_{f,i}}, \mathbf{C_{g,i}}$	Row vectors used in constructing mismatch equations.
$\mathbf{H_{fg}}$	Vector containing mismatch equations.
$\mathbf{X_{cir}}, \mathbf{X_{sup}}, \mathbf{X_{har}}$	Vectors including circuit, supply and harmonic state variables.
$\tilde{\mathbf{A}}_{\mathbf{on,i}}, \tilde{\mathbf{A}}_{\mathbf{off,i}}$	The state transition matrices of augmented system.

Modelling-2

ω	Microgrid operating frequency.
$\tilde{\mathbf{I}}^{\mathbf{N.L}}_{\mathbf{1}}$	Vector containing nonlinear loads' fundamental currents.
$\tilde{\mathbf{V}}_{\mathbf{1}}, \tilde{\mathbf{I}}_{\mathbf{1}}$	Vectors including the fundamental voltages and currents of all buses.
$\mathbf{P_1}$ and $\mathbf{Q_1}$	Vectors of fundamental active and reactive powers.
$P^I_{b,1}, P^{DG}_{b,1}, P^L_{b,1}$	Fundamental active power contributions of the network, DG, and load at bus b.
$Q^I_{b,1}, Q^{DG}_{b,1}, Q^L_{b,1}$	Fundamental reactive power contributions of the network, DG, and load at bus b.
$\mathcal{S}^B$	Set including all microgrid buses.
$V_{b,1}, \delta_{b,1}$	The magnitude and phase angle of bus b fundamental voltage.
$Y_{bk,1}, \theta_{bk,1}$	The magnitude and phase angle of the fundamental admittance between bus b and bus k.
ω^{nom}, V^{nom}	The nominal system frequency and voltage.
m^P_b, m^Q_b	The slopes of frequency-active power and voltage-reactive power droop characteristics.

P_b^{L0}, Q_b^{L0}	The nominal values for the active and reactive powers of the load at bus b.
α, β	The load active and reactive power exponents for dependence on voltage.
K_{pf}, K_{qf}	The coefficients for active and reactive power dependence on frequency.
$\mathcal{S}^{LB}$	Set including linear loads' buses.
$\mathcal{X}^{\mathbf{PF}}$	Vector comprising the magnitudes and angles of bus-voltages as well as the network frequency.
$\mathbf{F}$	Vector including power mismatch equations for all buses.
Re, Im	Operators returning the real and imaginary parts.
$\tilde{\mathbf{Y}}_{\mathbf{h}}^{\mathbf{Bus}}$	Harmonic bus admittance matrix.
$\tilde{\mathbf{I}}_{\mathbf{h}}$	Harmonic current source equivalent of nonlinear loads.
$\tilde{\mathbf{V}}_{\mathbf{h}}$	Microgrid bus harmonic voltages.
VSC	Voltage source converter.
v_o, v_{vsc}	The voltages of the LC filter and VSC.
i_{Lf}	The current of the filter inductor.
i_o	DG line current.
V_o^*, I_{lf}^*	The references for the voltage and current loops.
G_V, G_I	The controllers' transfer functions for the voltage and current loops.

Chapter 1

Introduction

1.1 Preface

The dramatic growth in the demand for electricity over the last decade on the one hand, and the economic and environmental issues related to electricity generation in large power plants on the other hand, have made the application of DGs an appealing option for distribution systems. The use of DGs in distribution systems has changed their passive nature. Distribution systems, which were once characterized by their unidirectional power flow, have been converted to bidirectional power flow systems, called active distribution systems (ADN).

Among different operating paradigm for integrating DGs, microgrids, in which clusters of DGs and loads are paralleled, provide a more reliable and efficient paradigm. Microgrids may be operated in two modes: grid-connected and islanded. In the grid-connected mode, the microgrid DGs are controlled and operated in the same manner as the DGs of ADNs. In the islanded mode, the basic control objective is to achieve accurate power sharing while maintaining voltages and frequencies close to their nominal values.

Nonlinear loads constitute a significant percentage of distribution system loads. Compact florescent lamps, PCs, TVs, and battery chargers are important single-phase nonlinear loads. Electric arc furnaces and heaters along with the line commutator converters, which are appearing in variable speed drive (VSD) applications, are among the most important three-phase nonlinear loads. VSDs are also found in air conditioning systems, pumps, compressors, and elevators. The current trend in the growth of nonlinear loads is expected to continue due to present intensive interests in improving energy efficiency. On the other

hand, some renewable energy resources, due to their nature, require a voltage source converter (VSC) for enery transfer to the grid. Such VSCs are introducing another source of nonlinearity to distribution systems.

The proliferation of nonlinear loads and generators in distribution networks results in harmonic pollution, one of the most significant power quality problems. Conventional distribution systems are designed to be operated at a single and constant frequency. However, the increasing use of non-linear loads can cause additional losses, poor power factors, reduced equipment life spans, and interference with communication, control and protection systems.

VSC-based DGs can be used for power quality improvement because of their high bandwidth. DGs' controllers have already been employed for resonance damping, harmonic compensation, non-fundamental power sharing, and the compensation of the negative sequence components of voltages and currents. As mentioned above, one of the basic control requirements in microgrids is the uniform sharing of active and reactive powers among different DGs. In the case of nonlinear loads, the current harmonics should also be shared in proportion with the DGs' capacities. Similar to the linear load sharing, the uniform distribution of nonlinear loads can be done either through decentralized or communication-based methods. While decentralized techniques enjoy simplicity and lower costs, communication-based techniques can offer higher control quality.

To quantify microgrid voltage and current distortions caused by the nonlinear loads, a harmonic analysis should be carried out. This analysis is crucial for the proper design of distribution systems, including sizing distribution transformers and cables, as well as setting protective relays. Further, this analysis can be used to estimate the possible error in the sharing of non-fundamental powers. Another potential application for the harmonic analysis is in the development of a communication-based supervisory controller for the accurate sharing of non-fundamental powers.

In addition to grid-connected and islanded modes for microgrid operation, isolated microgrids can also be found in off-grid regions such as remote communities, mines and military centers. High energy costs and environmental aspects have made isolated microgrid an appropriate solution. Optimal DG placement, in general, is necessary to achieve a microgrid's potential benefits with respect to its high investment cost. However, isolated microgrid planning requires its special features to be considered within the planning. These special features include the necessity of providing voltage support for isolated microgrids by some of the DGs, which to satisfy reliability constraints should be distributed throughout the microgrids. These DGs are operated based on droop characteristics. The droop-based operation impacts the flow of active and reactive powers as well as the voltage profile, and

needs a different power flow algorithm to incorporate these impacts into the planning formulation. Further, droop-based operation causes an error in the sharing of reactive power among DGs. This error is affected by DGs' locations and their feeder impedances, and thus, should be considered in the planning. Moreover, if a microgrid has been penetrated with nonlinear loads, harmonic analysis should be carried out to ensure the voltage distortion constraints are met. In the presence of capacitor banks, this requirement becomes more crucial. The harmonic analysis should also be tailored for isolated microgrids.

1.2 Motivation and Objectives

1.2.1 Microgrid Control

Among different operating regimes for DGs, microgrids, in which clusters of DGs and loads are paralleled, provide a more reliable and efficient paradigm. To achieve these features in islanding, equal sharing of active and reactive powers should be mandated within the main control objectives of microgrids. Likewise, the harmonic contents of nonlinear loads, which could be a significant portion of their apparent power, must be shared uniformly. Without uniform sharing, some DGs may be overloaded whereas others are lightly loaded. In this situation, in order to avoid tripping of the overloaded DGs, the system designer should consider the prospective maximum sharing error as the extra DG capacity, which conflicts with the optimal allocation of resources.

shaping the DGs' output impedances is the general solution applied for even sharing of nonlinear loads. However, there is an inherent trade-off between accurate sharing and voltage quality. In Chapter 3, a technique is proposed to achieve a better trade-off between sharing and voltage quality. This technique is based on obtaining an upper limit for each current harmonic, and uses a family of droop characteristics in terms of harmonic conductance versus harmonic current. The application of these droop characteristics also improves the voltage quality compared to the case in which constant harmonic conductances are used. To achieve the best performance from these proposed droop characteristics, an optimal tuning method is presented, which is based on a harmonic power flow algorithm. The mathematical formulation of the harmonic power flow algorithm and the optimization-based technique used for tuning the droop characteristics are provided in the same chapter.

On the other hand, thanks to the high bandwidth of DGs' controllers, the voltage-source-converter-interfaced DGs can be used as active filters, compensating the nonlinear

loads at their terminals. Thus, when it comes to a microgrid with local and common nonlinear loads, DGs' controllers are expected to compensate their local nonlinear loads, and share the common ones. However, it is challenging to do both tasks at the same time. In Chapter 3, a controller is proposed to address this challenge.

1.2.2 Microgrid Planning

Optimal DG placement allows improving the network performance in several ways, including system losses, voltage profile, and supply reliability. The problem of DG placement in power distribution network has a rich literature. However, the microgrid behaviour of DGs under islanded or isolated modes of operation has received less attention in the planning literature. In particular, when it comes to isolated microgrids penetrated with nonlinear loads, to the best of the author's knowledge, no research can be found.

In isolated microgrids, some of DGs are operated based on the droop characteristics. Unlike grid-connected microgrids in which the frequency and voltage are dictated by the main grid, application of droop characteristics for islanded/isolated microgrids causes the frequency and voltage to deviate from their nominal values by load variations. This effect should be considered in the planning of islanded/isolated microgrids. Further, nonlinear loads produce current harmonics that may cause severe voltage distortion. Suitable placement of the DGs can alleviate this issue. Thus, appropriate microgrid planning should also consider the flow of current harmonics.

On the other hand, applying capacitor banks (CBs) as the cheapest source of reactive power has a long history in distribution systems. Therefore, dedicating DGs as the only source of reactive power does not seem to be an economical solution for microgrids. In fact, the presence of CBs along with DGs should be expected. To maximize the benefits, the DGs and CBs should be simultaneously sited and sized in the planning. Moreover, the presence of capacitors would worsen the voltage distortion caused by nonlinear loads, since the capacitors affect the flow of harmonic currents that may lead to resonance or quasi-resonance. This necessitates to include a voltage distortion constraint in the planning of microgrids penetrated with nonlinear loads.

Chapter 4 proposes the idea of planning for isolated microgrids penetrated with nonlinear loads so as to simultaneously site and size the DGs and the CBs. The proposed planning method relies on a harmonic power flow algorithm that takes into account the specific features of isolated microgrids, and checks a power quality constraint in terms of total harmonic distortion of bus voltages.

1.2.3 Microgrid Harmonic Analysis

Microgrid harmonic analysis should be carried out to quantify the flow of non-fundamental powers, and to determine voltage and current distortions. Obtaining the steady-state operating point of a power network comprising nonlinear elements has already been developed in the literature. However, the previously proposed harmonic power flow algorithms have not considered specific features of islanded microgrids, i.e., the droop-based behavior of DGs, the fact that there is no slack bus, and the presence of converter-based DGs having several cascade control layers. In addition, the previous algorithms have important limitations for accompanying accurate nonlinear load models.

First, the lack of a slack bus affects the fundamental components of currents, which in turn, impacts on the flow of harmonics in islanded microgrids due to the dependence of harmonic currents on their fundamental components. Further, the droop-based operation of DGs leads to the network frequency changing from its nominal value, and affects the harmonics generated by DGs and nonlinear loads. Additionally, many DGs are connected to microgrids' networks through voltage source converters (VSCs) with several cascade control loops. The controllers generally applied for voltage-controlled DGs in islanded microgrids includes a power loop, which provides the reference for a voltage loop, and a current loop as the most inner loop. The effect of such controllers should be modelled in a harmonic power flow algorithm developed for microgrids. Moreover, given that accurate power flow algorithms usually suffer from narrow convergence region, an appropriate model for nonlinear loads should be developed and integrated to power flow algorithms so that in addition to being accurate, improve the convergence.

The core of a microgrid harmonic analysis is the modelling of the microgrids' nonlinear generators and loads. Microgrid nonlinear generators essentially comprise the above-mentioned VSC-interfaced DGs. In this thesis, the harmonic modelling of microgrids' nonlinear generators are conducted in several chapters. Chapter 3 presents the harmonic modelling of DGs with hybrid controllers of voltage and current. The harmonic modelling of back to back converters used in doubly fed induction generators are studied in Chapter 4. Chapter 6 considers energy-storage-based DGs with cascade controllers of voltage and current that are used for the provision of frequency and voltage support in islanded/isolated microgrids.

As for the nonlinear loads, microgrids include a whole spectrum of single-phase and three-phase nonlinear loads. Among them, three-phase power electronic devices, regarding their ratings, have a significant contribution in the harmonic generation. Also, three-phase diode bridge rectifiers constitute the most important nonlinear loads among the three-phase power electronic devices. An accurate model for all nonlinear loads, including

three-phase diode bridge rectifiers, must consider the mutual interactions of different harmonics. Further, a qualified model should be faster than that of the time-domain-based packages, such as PSCAD/EMTDC, which are characterized by integrating the system differential equations until reaching the steady state point. Additionally, the derivation of one harmonic should be independent of the derivation of other harmonics. Moreover, in the case of unbalanced systems, the model must consider the complexities relevant to the negative-sequence-component in the voltage, such as the presence of third harmonic multipliers even for three-phase three-wire systems.

Chapter 5 presents a comprehensive model for harmonic analysis of three-phase diode bridge rectifiers under distorted and unbalanced supply considering the afore-mentioned specifications. Chapter 6 proposes a harmonic power flow algorithm for islanded microgrids that includes accurate models for nonlinear loads and DGs. The model used for nonlinear loads is based on the one developed in Chapter 5, and the model applied for DGs takes into account the control structures that are typical of voltage-controlled DGs.

1.2.4 Thesis Organization

The rest of this thesis is organized as follows:

- Chapter 2 provides a necessary background in the modelling, control, and planning of microgrids for power quality assurance, in addition to a survey on the related works.
- Chapter 3 presents a decentralized-control technique to evenly share non-fundamental powers among distributed generators and to improve the voltage quality.
- Chapter 4 is dedicated to the development of a platform for optimal planning of distributed generators and capacitor banks in isolated microgrids with nonlinear loads.
- Chapter 5 proposes a comprehensive model for the harmonic analysis of three-phase diode bridge rectifiers under unbalanced and distorted supply.
- Chapter 6 presents an accurate harmonic power flow algorithm for islanded microgrids taking into account their specific features.
- Chapter 7 highlights the thesis contributions and provides insights for the future works on the improvement of microgrid power quality.

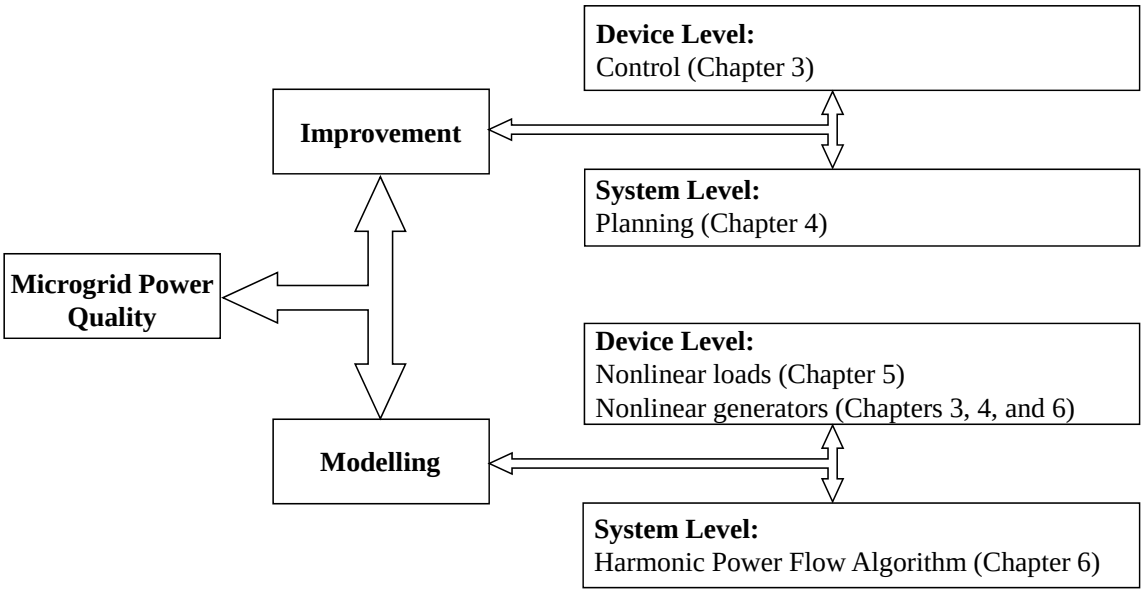

Figure 1.1: Thesis organization.

A summary of the thesis organization and the relations of different chapters are given in Figure 1.1. As can be seen, the thesis considers microgrid power quality improvement at two levels: 1) at the device level, in control (Chapter 3); and 2) at the system level, in planning (Chapter 4). Moreover, given the importance of the modelling in power quality studies, this thesis also concentrates on the modelling at two levels: 1) at the device level, in the modelling of nonlinear loads (Chapter 5) as well as generators (Chapters 3, 4, and 6); and 2) at the system level, in the development of a harmonic power flow algorithm (Chapter 6).

Chapter 2

Background and Literature Review

2.1 Microgrid Control

2.1.1 Background

2.1.1.1 Current-Controlled DG versus Voltage-Controlled DG

Microgrids, as a cluster of loads and distributed generators (DGs), can be operated in grid-connected and islanded modes. Many DGs are connected to microgrids' network through voltage source converters (VSCs), and thus, the VSCs' controllers must cover both the operational modes.

In the grid-connected mode, VSCs' controllers are in charge for injecting determined active and reactive powers, while considering power quality constraints. The determined active and reactive powers specify the reference of VSCs' current loops [1,2], and therefore, current-controlled DGs are conventionally applied.

In the islanded mode, the control system should supply the load demand under well-regulated voltage and frequency, while maintaining accurate power sharing among different DGs. To achieve this goal, droop characteristics in terms of frequency-active power and voltage-reactive power are employed to specify the reference of VSCs' voltage loops, and therefore, voltage-controlled DGs are applied [1, 2].

2.1.1.2 Communication-based versus Decentralized Control

Communication-based control techniques are able to provide excellent voltage regulation and accurate power sharing [3]. They are generally categorized as concentrated [4], master/slave [5], and distributed [6] controllers. Concentrated controllers consist of common synchronization signals and current-sharing modules that detect the total loads and determine each DG portion. While offering the best sharing quality, for both transients and steady state, concentrated controllers need the highest communication bandwidth among different communication-based techniques. Master/Slave controllers have one main DG in the voltage-controlled mode, and the rest of the DGs are operated in the current-controlled mode. Master/Slave controllers do not need synchronization as all DGs are connected to the main DG through a communication link. The drawback of this technique is its dependence on a master unit, which represents a single point of failure. In contrast, distributed controllers do not require any central controller since instead of relying on global information, they merely require data transfer among the adjacent units, which can be performed through a low bandwidth communication link [7].

Regardless of the advantages obtained by communication-based controllers, they add to the cost of the system. Also, there are some concerns regarding the reliability and expandability of communication-based controllers since distance communication lines can be readily affected by environmental noise. Considering such issues, decentralized techniques [8] based on droop characteristics have been proposed and developed. While avoiding the complexity and cost of communication-based controllers, they suffer from reactive and non-fundamental power sharing errors. These errors are mainly due to different and unknown line impedances and the fact that conventional droop characteristics do not consider sharing of harmonic currents generated by nonlinear loads [7].

2.1.2 Literature Review

2.1.2.1 Decentralized Control

Given the high bandwidth of VSC-based DGs, they have been extensively applied in the literature for power quality improvement. The existing techniques in the literature include, direct control of voltage distortion [9], indirect voltage control by harmonic compensation [10], [11], resonance damping [12], hybrid control of voltage and current [2], [13], hierarchical voltage quality improvement [14], and unbalanced load compensation and nonlinear load sharing [15–22]

A droop characteristic in terms of conductance versus harmonic power (G-H) was proposed in [15] to share harmonic powers in an islanded microgrid. The application of this algorithm is limited to DGs with L-type filters, since the algorithm is based on the control of inverter current.

In [16], a proportional-resonant (PR) controller was introduced along with a resistive virtual output impedance to achieve an acceptable performance as a trade-off between accuracy in harmonic current sharing and voltage distortion. The proposed method assumed a single fixed value for the DG virtual output resistance at all harmonics, leading to a limited performance at high nonlinear loading and in particular when line impedances are considerably mismatched. In [17], a modified version of the method suggested in [16] was proposed on a centralized basis.

Alternatively, a decentralized controller with distinct virtual resistance and negative inductance at each harmonic was presented in [23]. Considering different harmonic resistances can improve the DG controllability over the sharing error, whereas fixed values of virtual resistance may conflict with the standard harmonic limits at high nonlinear loading. A control method based on disturbance injection in terms of active power was proposed in [19]. Based on the accuracy of the typical frequency-active power droop characteristic, the virtual harmonic inductances were controlled to improve the nonlinear load sharing. Nonetheless, a portion of the DG capacity should be devoted to the active power disturbance, prohibiting the full utilization of the DG capacity.

In [20], a negative virtual harmonic impedance was proposed for nonlinear load sharing. However, the idea was not evaluated for lines with both resistive and inductive components. As the nonlinear load-sharing problem is caused by the mutual impacts of both inductive and resistive components of the lines, separate manipulation of those components by virtual negative values may not completely address all line impedance scenarios, which may hinder efficient tuning. To deal with nonlinear load sharing, the authors of [21] proposed a combination of repetitive and deadbeat control and the method in [22] offered a programmable harmonic resistance. However, the feasibility of compensating local nonlinear loads in those control techniques was not validated.

2.1.2.2 Communication-based Control

A centralized approach was proposed in [14] to enhance the voltage quality at sensitive load buses and to improve the nonlinear load sharing. The control structure consists of primary and secondary controllers. The primary controller is the droop-based local controller of the DGs equipped with virtual impedance for sharing of nonlinear loads. The primary

controller is able to improve the nonlinear load sharing at the expense of increasing the harmonic distortion. A central controller, called here a secondary controller, is applied to improve the voltage distortion of sensitive load buses, by manipulating the virtual impedance of primary controller. To reduce the required bandwidth of the communication link, the voltage harmonics of the sensitive load buses are transformed to the dq components through Park transformation. The issue with this controller is the transformation error caused by the difference in voltage angles of different buses, since the angle of each DG bus voltage is used for dq transformation.

The authors in [18] introduced another hierarchical control strategy to improve nonlinear load sharing and power quality. The control framework consists of a droop-based primary controller and an agent-based distributed secondary controller. The primary controller comprises a V-I droop characteristic that generates the voltage reference of each DG for accurate sharing of the load current. However, the secondary controller compensates for voltage distortion. A GPS timing technology is applied to synchronize the local reference angles. The proposed droop characteristic is based on one adaptive droop characteristic and accordingly is not able to consider different contributions of different harmonics.

2.1.2.3 Conclusion on Microgrid Control

This thesis has focused on decentralized control schemes because of the relatively higher costs of communication-based controllers, and the issues that can be assigned to the reliability of such controllers. Microgrid's literature has realized the fact that similar to active and reactive powers, the non-fundamental power must also be shared evenly among different DGs. However, the current literature, which is essentially based on the shaping of DGs' harmonic resistances, has the following limitations. First, the different levels of different harmonics have not been taken into account. Second, no tuning method has been proposed so far that allows selecting virtual harmonic resistances. Third, the current control topologies are not able to compensate the harmonic content of local nonlinear loads while sharing the common ones. Chapter 3 presents a decentralized controller to address these limitations.

2.2 Microgrid Planning

2.2.1 Planning Background

Optimized distribution system planning and operation entails optimal DG placement. Although proper DG placement can improve power network performance in terms of voltage profile, energy loss reduction, power quality, and reliability, inappropriate DG placement may cause extra losses and costs. Thus, a comprehensive planning considering all contributing factors, including the network objectives and constrains while counting for different DG technologies, load types and time variations, is inevitable [24].

The objective function of microgrid planning can be single or multi-objective. The most common single-objective functions are: 1) minimization of the power or energy loss; 2) meeting certain reliability requirements such as expected energy not supplied (EENS); 3) minimization of cost; 4) maximization of profit; 5) minimization of voltage drops; and 6) maximization of loadability; 7) deferral of upgrade investments; and 8) maximization of DG penetration [24].

In general, optimizing one objective could negatively impact other objectives. Therefore, the planning problem must be considered multi-objective in order to consider several objectives at the same time. The simultaneous consideration of several objectives can be carried out through the weights, where multi objectives are converted into a single objective function. However, there are two issues with the application of weight factors. First, the optimal solution can be severely affected by the weight coefficients. The other issue is due to the fact that different objectives have different units and ranges. To alleviate such drawbacks, evolutionary algorithms, e.g. $\epsilon-$constant method can be used which is able to identify the Pareto-optimal region [25].

The most common constraints applied for planning are power balance equations, bus voltage limits, in addition to short circuit level, reliability constraints, and total harmonic distortion for the system voltages. The details of load model considered in the planning depends on the type of conducted studies. The models applied in the literature vary vastly from one level, multi-level, and time varying load to probabilistic and fuzzy models. The planning outputs or decision variables are usually DG location, size, number, and technology type, e.g. wind, solar, diesel, and fuel cell [26].

Methodologies applied for planning are categorized as analytical, numerical and heuristic methods. Analytical planning methods have the advantage of easy implementation and fast execution. However, making some simplifying assumptions are inevitable in analytical methods and accordingly, the results are only indicative. On the other hand, numerical

methods offer more flexibility in terms of counting the practical aspects of power systems. The nonlinear programming and sequential programming are among the most popular methods for optimal DG placement. Also, exhaustive search method guarantees finding the global optimum, although this method is computationally expensive for large scale systems. Eventually, the heuristic methods such as genetic algorithm (GA) and particle swarm optimization (PSO) are usually robust and provide near optimal solutions for large and complex DG placement problems [24].

2.2.2 Literature Survey

A lot of work has already been carried out for the allocation of DGs in distribution systems (ADNs). Table 2.1 illustrates some of the previous literatures on the DG allocation problem, including their objective functions, constraints, decision variables and methodologies [27–38]. Also, shown in this table is "multi-stage expansion planning" introducing literatures considered the long-term multi-period planning. In spite of numerous research papers studied the problem of DG allocation for ADNs, relatively little works have addressed DG planning for microgrids. However, to achieve microgrid potential benefits with respect to its high investment cost, creating a roadmap for microgrid planning is necessary.

Microgrids, as clusters of loads and distributed generators (DGs), have already been acknowledged by IEEE Std. 1547.4 to maintain the service of critical loads when a supply grid is not available [39]. Continuation of service in such islanded modes can provide significant cost saving. On the other hand, high energy costs and environmental aspects have motivated energy participants to integrate renewable generators into microgrids so that they are rarely seen without renewable generators. Along with grid-connected microgrids, in off-grid regions such as remote communities [40], mines [41], islands [42] and military centers [43], isolated microgrids can be found, in which the issues relevant to fuel transportation are also added to the above motivations for using renewable generators.

Optimal DG placement, in general, is necessary to achieve a microgrid's potential benefits with respect to its high investment cost. Although islanded and isolated microgrids have almost equivalent operational and control requirements, they are different from a planning point of view, mainly due to the short time of microgrid operation in the islanded mode [44]. Accordingly, in the case of grid-connected microgrids, the islanded mode requirements hardly ever become dominant planning constraints. However, an isolated microgrid needs its special features to be considered within the planning. These features include the necessity of providing voltage and frequency support for the microgrid by some of the DGs, essentially by diesel generators [45]. To satisfy the reliability constraints, these

Table 2.1: Summary of DG planning literature review for ADNs.

	Ref. #	[27]	[28]	[29]	[30]	[31]	[32]	[33]	[34]	[35]	[36]	[37]	[38]
Objective Function	Single/Multi Objective	Single	Multi	Single	Multi	Single	Single	Single	Single	Single	Single	Multi	Multi
	Multi-Stage Expansion Planning	No	No	No	No	No	Yes	Yes	Yes	No	No	No	No
	Minimize Power Loss		*	*	*								*
	Minimize Energy Loss					*							
	Minimize Cost						*	*	*	*		*	
	Maximize DG Owner's Profit											*	
	Maximize DG capacity										*		
	Deferrral of Upgrade Investment	*	*										
	Minimize Votage Deviation				*								
	Minimize Votage Deviation				*								*
	Conductor Current Capacity				*								
	Short Circuit				*								
	THD												*
	Resonance Index				*								*
Special Constraints	Reliability		*				*					*	
	Emission		*										
	Voltage Stability											*	
	THD												*
Uncertainty	Load		*			*			*				
	Non-Dispatchable DGs		*			*			*				
Decision Variables	Size	*	*	*	*	*	*	*	*	*	*	*	*
	Location	*	*		*	*	*	*	*	*	*	*	*
	Number	*	*							*			*
	Type					*			*				
	Optimization Methodology	MINLP-MP	GA	Analytical	GA	MINLP-MP	PSO	MILP-MP	MILP-MP	MINLP-MP	MINLP-MP	PSO	PSO
	MILP-MP/MINLP-MP: Mixed integer linear/nonlinear programming solved using mathematical based programming technique. GA : Genetic Algorithm; PSO: Particle Swarm Optimization												

voltage-controlled DGs should be distributed throughout the islolated microgrids, which has not been included so far in the planning. Further, in isolated microgrids, some DGs are operated based on droop characteristics. Unlike grid-connected microgrids, in which the frequency and voltage are dictated by the main grid, application of droop characteristics, frequency-active power and voltage-reactive power, for isolated microgrids causes the frequency and voltage to deviate from their nominal values [46]. As will be explained [Chapter 4], the droop characteristics, especially the voltage-reactive power one, affect the sizes of DGs and should be merged into the planning formulation, which has not been done yet. Moreover, if a high penetration of nonlinear loads exists, harmonic analysis suitable for planning of isolated microgrid should be carried out to ensure the power quality constraints in terms of voltage distortions are met.

On the other hand, capacitor banks (CBs) have always been regarded as the most economic solution for volt/var control and power loss reduction of distribution systems [47]. Considering the reality of modern distribution systems, DGs and CBs coexist, and they share some of their operational tasks. Thus, to maximize the benefits, DGs and CBs must be simultaneously sited and sized. This point has been propounded in [48] for active distribution networks (ADNs); however, a different formulation is required for an isolated microgrid to incorporate its specific features, which has not been addressed in the literature. Additionally, capacitors affect the flow of harmonic currents and may cause resonance and high voltage distortion levels [47]. This fact emphasizes the need for harmonic power flow considerations in the planning of microgrids penetrated with nonlinear loads.

Optimal planning of isolated microgrids has been tackled in a number of studies. The research in [40] carried out the planning for sizing different types of DGs. In [49], a coordinated sizing of energy storage and diesel generators were proposed by applying the discrete Fourier transform. The authors in [50] proposed a long-term planning to size renewable DGs for Canadian remote communities to maximize the communities' social welfare. This work has been ameliorated in [51] by adding energy storage units. In [52], the optimal siting and sizing of renewable DGs and energy storages were studied using a heuristic-moment-matching method to model the uncertainties associated with load demand, wind speed and solar irradiance. The authors in [53] jointly determined the optimal topology, i.e., AC, DC, or hybrid AC/DC, in addition to the optimal sites and sizes of DGs and energy storages. In [54], a planning platform was proposed that determines the optimal year of installation and sizes of energy storages using a decomposition-based approach. The authors in [55] conducted a research on multi-energy isolated microgrids for combined heat and power technologies, considering the security constraint of maintaining sufficient reserve capacity. However, these works included neither the features relevant to the droop-based operation of isolated microgrids, nor the distribution of voltage controlled DGs in

the planning. Moreover, DGs have been considered as the main source of reactive power, and the need for CBs and corresponding harmonic analysis have been ignored.

By contast, incorporating a harmonic power flow in the planning of ADNs has already been suggested. A probabilistic optimal planning for renewable DGs was propounded in [56] to minimize the annual power loss of a typical rural distribution feeder with a high penetration of nonlinear loads. Since this research was performed on an ADN, the specific features of isolated microgrids have not been considered in the planning. The planning objective in [57] is to determine the optimal location and size of current-controlled DGs for a distribution network, considering harmonic and protection limits. The only source of non-linearity investigated in this work are the DGs that are modeled by the harmonic upper limits of international standards. It is shown that the planning solution is affected by considering voltage harmonic constraint. However, the proposed method is not applicable for isolated microgrids, because of the presence of droop-based voltage controlled DG and other non-linearity resources, e.g., variable speed drives or unified power flow chargers of electric vehicles. Moreover, the above works suffer from the application of over-simplified models for inverter-based DGs, such as type III wind turbines, given that these DGs can lead to resonance due to the possibility of mutual interactions between a DG's output filter and control system on the one hand, and the distribution system on the other hand [58,59].

2.2.2.1 Conclusion on microgrid planning

The previous section shows that the planning literature for isolated microgrids has the following gaps. First, there is no prior research considering the impacts of nonlinear loads in the planning of isolated microgrids. It should be underlined that isolated microgrids include some specific features that necessitates different planning formulation from that of grid-connected microgrids and active distribution networks. Second, although there are few works on the planning of active distribution networks (not microgrids) considering the impacts of nonlinear loads, these works have not taken into account the possibility of resonance that can be caused by wind turbines. Third, the importance of making successful islands following a contingency, and accordingly, the need for effective distribution of dispatchable DGs, have not been included in the planning. Chapter 4 proposes a planning platform to address these gaps.

2.3 Microgrid Harmonic Analysis

2.3.1 Harmonic Power Flow

Generally speaking, microgrid harmonic analysis should be carried out to quantify the distortion in voltage and current waveforms at various system buses. Such data are crucial in assisting distribution engineers with the proper selection of k-factor ratings for distribution transformers, conductors' ampacities, voltage/current transformers applied for protection and metering, and in protective relay settings. Further, as will be shown in Chapter 3, for islanded microgrids with nonlinear loads, the non-fundamental power sharing error can be significant. To address this issue, the possible sharing error for islanded microgrids should be investigated. This demands for a suitable tool considering the specific feature of islanded microgrids, and can be used for any arbitrary topology, including multi-bus structures. This tool solves the harmonic power flow (HPF) problem. The solutions of the harmonic power flow problem can be obtained either directly or through iterative methods [60].

The direct method [60], or current injection [61], is based on representing nonlinear loads by several current sources at discrete frequency steps for the particular range of interest. The advantages of this one step method are its simplicity, acceptable accuracy for most electronic loads, and the fact that several nonlinear loads can be handled simultaneously. However, its drawbacks are applying a typical current spectrum, which does not consider the interactions among the network and loads, along with its inaccuracy for arc furnaces as well as resonant electronic converters [61]. To deal with these limitations, iterative harmonic analysis should be used, which are Newton-based techniques, and usually involve a complicated Jacobian matrix [62, 63]. Iterative methods consist of three typical steps [63]. First, non-linear loads are formulated as voltage-dependent current sources, so that at each iteration a fixed harmonic current source represents a nonlinear load. Second, at each iteration, the harmonic current source is updated by using estimated harmonic voltages. Then, the harmonic voltages are obtained from the harmonic currents. Third, more accurate harmonic currents can be computed from these harmonic voltages. Sufficiently small changes in the harmonics currents stop the algorithm. The disadvantages of iterative harmonic analysis methods are their slow and narrow-margin convergence [60].

The authors in [64] introduced the first formulation for harmonic power flow that consists of conventional power flow equations, reformulated to include nonlinear devices. The formulation, called complete HPF, is based on simultaneous solution of power constraints, given by power mismatch equations, and harmonic current balance at all buses, as well as nonlinear load equations describing harmonic currents in terms of harmonic voltages. This

method accuracy is perfect as it allows the power consumption to be updated based on the calculated harmonics. However, this technique might encounter convergence problems for large power systems with many nonlinear loads [65]. As an alternative for complete HPF, the sequential HPF has been introduced by [63] and [66], in which fundamental power flow (FPF) and harmonic power flow algorithms are repeated in sequence until convergence is achieved. The convergence condition is defined by the equality of fundamental voltage magnitudes obtained by FPF and HPF sub-routines. The nonlinear loads are included as P/Q ones in FPF and are updated in each iteration. The sequential power provides superior convergence compared with complete HPF. However, the relatively slow convergence is an issue with all sequential HPF algorithms [65].

2.3.2 Nonlinear Load Modeling

Characterizing and modelling of harmonic generating resources is one of the main steps in harmonic analysis. Among nonlinear loads, three-phase diode bridge rectifiers, due to their extensive application and the significant current harmonics that they generate, are of particular importance [67]. They are often seen as the front-end of a wide range of energy processing units, including variable speed drives (VSDs) [68], DC/DC converters [69], arc furnaces [70], and distributed energy resources [71].

The brute-force time-domain modelling should be regarded as the first modelling method due to their easy programming property [72]. However, to obtain a steady-state solution using the brute-force approach, the system's differential equations must be integrated until the system reaches the steady state, which is computationally expensive. Alternatively, harmonic-domain methods have been proposed in [73–75]. Such methods avoid system transients, and accordingly are more effective. However, they suffer from truncation errors caused by the inherent trade-off between accuracy and the number of harmonics considered in the calculation.

In [76], mathematical models of a three-phase diode bridge rectifier have been derived in the Laplace domain, for continuous conduction mode (CCM) and discontinuous conduction mode (DCM). The current spectra are then obtained using the Laplace to Fourier domain transform. In spite of the accuracy of the developed formulation, the model involves excessive analytical heaviness. Further, the possibility of model extension for an unbalanced supply has not been checked. A time-domain based technique has been introduced in [77]. Instead of integration, the Fourier series multipliers that give a harmonic are obtained through the solution of a first order differential equation, which is added to the system's state-space model for each harmonic of interest. In this model, the turn-on, turn-off, and

commutation angles, or equivalently the switching instants, are obtained based on a sixth-period symmetry. However, the complexities relevant to a nonideal supply have not been addressed. Further, harmonic phase angles need to be included to account for harmonic cancellation effect, when multiple nonlinear loads exist in the network. In addition, the models proposed in [76] and [77] are limited to rectifiers with capacitive (C) filters.

On the other hand, a harmonic analysis approach for thyristor-bridge rectifiers has been proposed using a frequency coupling matrix (FCM) [78]. The matrix is developed by applying converter switching functions, and writing the Fourier series for the current harmonics in terms of the input voltage harmonics. This work has been extended to single-phase and three-phase diode bridge rectifiers [67, 79]. The model has also been used to estimate the harmonic content of electric vehicle charging stations [80]. The main advantage of this modelling technique is that the matrix does not vary with the harmonic conditions. However, due to the fact that the switching instants for diode rectifiers are not exactly calculated, the accuracy of harmonic analysis is compromised.

For stability studies, the input impedance of diode bridge rectifiers has been analytically derived in [81], using small-signal analysis. Nonetheless, small-signal based models are only valid for small perturbations around an operating point. In [82], a dynamic-average-value model has been proposed using multiple reference frame theory. This model allows for considering major harmonics of interest in time-domain studies, while neglecting the switching effect at higher frequencies. This modelling approach is several times faster than the conventional time-domain modelling; however, non-characteristic harmonics have not been considered.

To capture the complete steady-state characteristic and non-characteristic harmonics, two analytical models have been proposed for the CCM [83] and DCM [84] of a three-phase diode rectifier with a capacitive/inductive (LC) filter at the DC side, under both unbalanced and distorted supply. However, the developed models are only formulated for the under-damped mode that corresponds to high X/R ratio, which is not always the case for distribution networks. In addition, the Fourier analysis entails two mathematically-involved and distinct formulations for the CCM and DCM.

In response to the aforementioned shortcomings, this thesis extends the method presented in [77], and proposes a systematic approach to deriving all steady-state harmonics of a three-phase diode bridge rectifier based on a state-space model, under both distorted and unbalanced supply. To provide a quadratic convergence, an analytical Jacobian matrix is developed. Further, the proposed harmonic analysis can accommodate different filter structures at the DC side by introducing a large virtual resistance (R_{inf}), as will be explained. Thanks to the module-wise nature of the state-space model, the developed model

and Jacobian matrix are independent of the rectifier operation mode and filter structure.

2.3.3 Harmonic Modeling of Voltage-Controlled DGs

Modelling of VSCs can be performed either through the transfer function or frequency coupling matrix (FCM). The transfer function is able to provide both steady state and dynamic information, although it is not typically able to provide switching harmonics. The FCM-based techniques only give the steady state relation between the voltage and current harmonics while taking into account the harmonics generated by converter's switching action [85].

The transfer function-based modeling can be applied for obtaining the Thevenin or Norton equivalent harmonic impedance for voltage-controlled and current-controlled DGs, given the DGs' controllers and filter parameters as well as the system operating frequency. A transfer function for voltage-controlled DGs with proportional-integral-derivative controller (PID) was proposed in [86]. The authors in [87] introduced the transfer function-based modeling for voltage-controlled DGs with cascaded voltage and current control loops to study the stability of controllers compensating the negative sequence components of bus voltages. The voltage and current control loops are governed by proportional-resonant controllers (PRs). Transfer functions for current-controlled DGs applied as active harmonic filters have been given by [88], in which a bank of PR controllers has been employed. The authors in [19] extracted the transfer function for hybrid controllers of voltage and current for the voltage-controlled and current-controlled modes of operation.

Similar to AC/DC converters, some works have been dedicated to the FCM model of voltage source converters (VSCs). However, the extraction of the FCM for VSCs is more complicated because of the PWM-based nature of VSCs' switching functions. Unlike the switching functions of AC/DC converters that have few turn-on and turn-off angles, the switching functions of VSCs include a lot of short-period switchings. The research conducted in [85] only considered open-loop VSCs, assuming all switching points of the target waveform are available. The idea is to augment the state space model of a VSC with a ficticous first order differential equation, for each harmonic of interest. Thanks to the invariable structure of the state transition matrix of the augmented-state-space model, the FCM of VSCs is derived. The authors in [89], developed an iterative method to obtain the FCM of closed-loop VSCs. However, the method has not been tested for systems with more than two VSCs. Eventually, in [90], a so called loop-breaking technique has been proposed that is able to deal with multi-converter systems. The method has been tested for a three-VSC system, in which VSCs' currents and DC-side voltages have been

controlled. However, the complexity of the proposed algorithm in the case of controllers applied for VSC-interfaced DGs, i.e., droop characteristics, voltage and inner current loops will be exacerbated.

It is worth nothing that the selection of suitable method for representing VSCs in a harmonic analysis should be based on the switching frequencies of VSCs. In general, the switching frequency of a certain application is determined considering the power and voltage levels. Typically, the switching frequencies of microgrids are relatively high. For medium voltage, [17] amd [91] considered switching frequencies of 6kHz and 2kHz, respectively. For low voltage, [14] and [8] are based on switching frequencies of 10kHz. This may be compared with values typically applied for high power applications [92], in which numbers around 3 to 9 times of the line frequency are proposed. High switching frequencies of microgrids allocate the harmonics at high frequencies. Such high frequency harmonics can be filtered by the DGs' output filters, and accordingly, neglecting the switching harmonics is not a limiting factor. This allows representing VSCs through transfer function methods in a harmonic analysis.

2.3.4 Power Flow for Islanded Microgrids

Islanded microgrids have specific features that should be considered in their power flow formulation. First, the DGs are typically droop based. Second, there is no slack bus. Third, the steady state frequency is not equal to the rated frequency. Fourth, in an islanded microgrids, the DGs are of voltage-controlled type. The authors in [93] formulated both single-phase and three-phase power flow for AC islanded microgrids, taking into account the above-mentioned factors and solved the equations using a Newton-trust region method. The same problem has been solved in [94], using the Newton Raphson method and accordingly, an analytical Jacobian has been provided. The authors in [95] and [96] solved the problem for hybrid AC/DC microgrids using Newton-trust region and Newton Raphson methods, respectively. However, all these works did not consider the attendance of nonlinear loads in microgrids. The penetration of nonlinear loads affects fundamental voltages and currents, and also causes load sharing errors in the islanded mode of operation.

The authors in [97] developed a power flow algorithm considering the influence of harmonic powers that takes into account the specific features of islanded/isolated microgrids. The algorithm is a complete harmonic power flow one that simultaneously solves all power mismatch equations. In this algorithm, the nonlinear loads are modelled using a harmonically coupled matrix. However, this technique is mainly suitable for thyristor-based nonlinear loads, which are not the dominant nonlinear loads in microgrids. Further, in

this algorithm the voltage source converters have been treated as an ideal source, which is not realistic. Moreover, complete harmonic power algorithms are characterized with their convergence issues [65]. Therefore, it is difficult to extend the proposed algorithm to accommodate other nonlinear loads, specially those proposed in [77] and [83].

2.3.5 Conclusion on Microgrid Analysis

The available models in the literature for the harmonic analysis of three-phase diode bridge rectifiers suffer from one or more of the following limitations:

- They are just suitable for the case with C filters.
- Distortion in voltages have not been included.
- Harmonic phase angles, which are required when more than one nonlinear load exists, have not been extracted.
- The effect of unbalanced voltages have not been incorporated.
- A model is based on a limiting assumption for X/R ratio.
- The Jacobian matrix includes terms with the integration of matrix exponential.

Chapter 5 presents a model for harmonic analysis of three-phase diode bridge rectifiers to address the above issues.

On the other hand, the literature requires a tool to solve the harmonic power flow for islanded microgrids. The harmonic power flow should consider the droop-based nature of islanded microgrids, lack of a slack bus, and the presence of voltage-controlled DGs. Further, the model should be able to be combined with the accurate models of nonlinear loads. Considering the convergence criteria, sequential harmonic power flow algorithms are selected in which the fundamental and harmonic power flow algorithms are repeated in sequence until convergence is achieved. Further, due to the typical range of microgrids' switching frequencies, the DGs are modelled using their transfer functions. In addition, to obtain accurate results, the mutual interactions of different harmonics are taken into account. Chapter 6 proposes a harmonic power flow algorithm that includes the above requirements.

Chapter 3

A Decentralized Control Scheme for Enhanced Nonlinear Load Sharing and Power Quality in Islanded Microgrids

3.1 Introduction

The sharing of nonlinear loads among different distributed generation units (DGs) is always a tradeoff between accuracy and voltage quality. This chapter[1] proposes a virtual harmonic conductance for each harmonic as a family of droop characteristics in terms of conductance versus current. Assigning a variable conductance for each harmonic current improves the DG controllability, thus offering accurate nonlinear load sharing, which is crucial at the near-rated loading and enhanced voltage quality. This chapter also unveils a tuning methodology for the droop characteristics that sets a maximum permissible value for each individual harmonic to comply with international standards. Lastly, a hybrid voltage and current control system is suggested to accurately track the DG harmonic conductance designated by the proposed droop characteristics. While the proposed algorithm is capable of accurately distributing common nonlinear loads among DGs, it also enjoys the advantage

[1] A version of this chapter has been published: A. H. Yazdavar, M.A. Azzouz, E. F. El-Saadany, "A Novel Decentralized Control Scheme for Enhanced Nonlinear Load Sharing and Power Quality in Islanded Microgrids", *IEEE Trans. on Smart Grid.*

of supplying local nonlinear loads by their dedicated DGs. A comprehensive performance evaluation assures the effectiveness of the proposed control strategy.

3.2 Contributions

The main contributions of this work can be summarized as follows:

- A family of droop characteristics in terms of harmonic conductance versus harmonic current ($G_h - I_h$) is proposed where each harmonic is characterized by a droop characteristic. This flexible structure allows for improved voltage quality, and better sharing accuracy.
- The problem of nonlinear load sharing is mathematically formulated to determine the maximum nonlinear load sharing error and hereupon to analytically allocate the minimum DG spare power. Therefore, it can reduce the DG investment cost while avoiding the system overloading.
- A tuning methodology is suggested to adjust the droop characteristics. Unlike the previously proposed nonlinear load sharing methods, this method ensures that the system voltage quality complies with the international standards given by [98–100]. Further, an optimization model that employs the developed mathematical formulation is applied for optimal tuning of the proposed $G_h - I_h$ droop characteristics.

3.3 Problem Formulation and Analysis

This section mathematically formulates the harmonic current flow problem to quantify the sharing error and the voltage distortion of islanded microgrids that supply nonlinear loads. This formulation also allows for designing a control system which can tackle the lack of deterministic information about rating and frequency spectrum of nonlinear loading.

Figure 3.1 illustrates a sample microgrid working in autonomous mode to study common load sharing among different DG units. Conventionally, droop characteristics in terms of frequency-active power ($\omega - P$) and voltage-reactive power ($V - Q$) are adopted as a decentralized approach to share loads among DGs in islanding.

In supplying a nonlinear load, the fundamental power is always accompanied by a non-fundamental power which contributes a significant portion of the total power. As

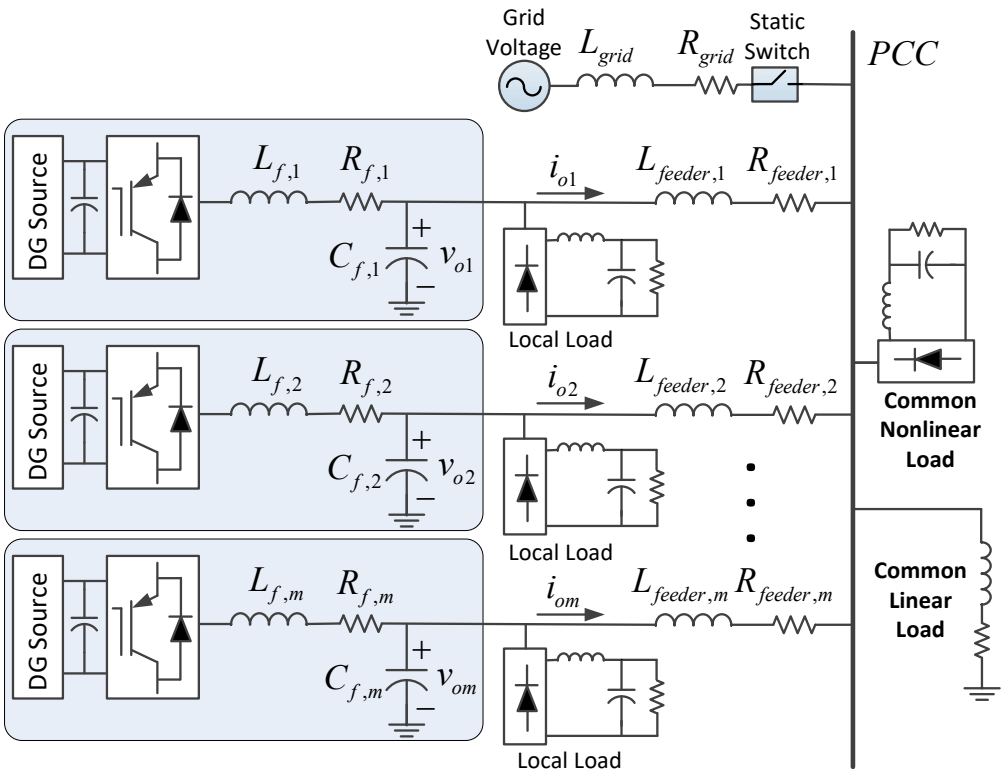

Figure 3.1: m-DG microgrid system.

the conventional droop characteristics have nothing to cope with non-fundamental power sharing, without a proper solution, overloading of certain DGs due to uneven sharing of non-fundamental power is possible. To protect DGs from overloading, the prospective maximum sharing error shall be considered as an extra DG capacity at the design stage, which is cost-ineffective. Alternatively, common nonlinear loads should be evenly distributed between DGs to minimize the sharing error and thus rendering an optimal utilization of the available DG capacity.

To formulate the problem, the equivalent harmonic circuit of the m-DG islanded microgrid is obtained at different harmonics, as shown in Figure 3.2. For generality, the i^{th} DG at the h^{th} order harmonic is represented by its Thevenin equivalent impedance, $Z_{DG,i,h}$, modelling the effect of an impedance shaping method. Without impedance shaping, $Z_{DG,i,h}$ is near zero which is achievable through employing voltage source converter having a bank of PR controllers in the voltage control loop [9]. The nonlinear load is represented by a

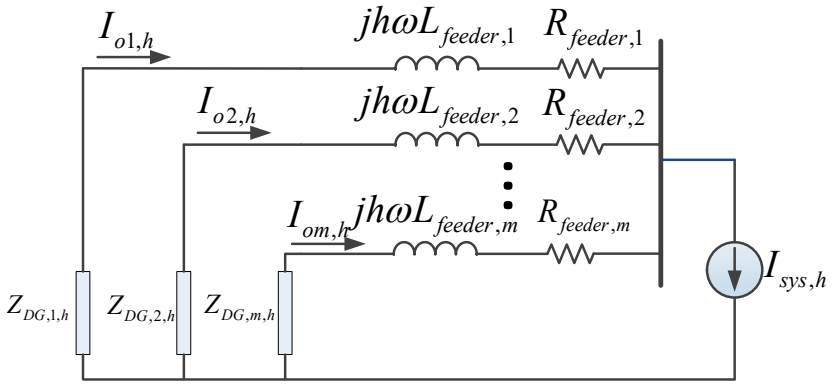

Figure 3.2: The equivalent harmonic circuit of the m−DG microgrid.

current source,$I_{sys,h}$, which is quite accurate up to the harmonic voltage distortion levels of at least 10% [98]. In the formulation, local nonlinear loads are not considered because their harmonic content is compensated by their dedicated DGs according to the proposed control method which will be explained in Section 3.5.

By analyzing the equivalent circuit, the harmonic current in each feeder can be calculated as follows:

$$I_{oi,h} = \frac{Z_{net,h}}{Z_{DG,i,h} + Z_{feeder,i,h}} I_{sys,h} \tag{3.1}$$

where $I_{oi,h}$ and $Z_{DG,i,h}$ are the h^{th} order harmonic current and impedance of the i^{th} DG, respectively; $Z_{net,h}$ and $Z_{feeder,i,h}$ represent the network harmonic impedance and feeder impedance, respectively, i.e.,

$$\frac{1}{Z_{net,h}} = \sum_{i=1}^{m} \frac{1}{Z_{DG,i,h} + Z_{feeder,i,h}} \tag{3.2}$$

$$Z_{feeder,i,h} = R_{feeder,i} + jh\omega L_{feeder,i} \tag{3.3}$$

where $R_{feeder,i}$ and $L_{feeder,i}$ are the feeder impedance components and ω is the system fundamental frequency.

The obtained harmonic currents can be used to calculate the non-fundamental apparent

power for the ith DG, i.e., $S_{N,i}$, using the definition of IEEE standard 1549 [101].

$$S_{N,i} = V_{oi,1}\sqrt{\sum_{h} I_{oi,h}^2} \tag{3.4}$$

where $V_{oi,1}$ and $I_{oi,h}$ are the fundamental voltage and the h^{th} order harmonic current of the i^{th} DG, respectively. Substituting from (3.1) into (3.4), the sharing error of non-fundamental apparent power, $\Delta S_{N,i}$, for the i^{th} DG can be calculated as

$$\Delta S_{N,i} = \underbrace{V_{oi,1}\sqrt{\sum_{h} \left(\alpha_i I_{sys,h}\right)^2}}_{S_{N,i}^{req}} - \underbrace{V_{oi,1}\sqrt{\sum_{h} \left(\left|\frac{Z_{net,h}}{Z_{DG,i,h} + Z_{feeder,i,h}} I_{sys,h}\right|\right)^2}}_{S_{N,i}} \tag{3.5}$$

where $S_{N,i}^{req}$ is the required non-fundamental power to be supplied by the i^{th} DG, $S_{N,i}$ denotes the DG non-fundamental power, and α_i is added to incorporate the effect of different DG ratings and is defined by

$$\alpha_i = \frac{I_{rated,DG,i}}{\sum_{i=1}^{m} I_{rated,DG,i}} \tag{3.6}$$

where $I_{rated,DG,i}$ is the rated current of the i^{th} DG. Accordingly, the non-fundamental power sharing error between the i^{th} and j^{th} DGs can be written as

$$\Delta S_{N,i,j} = \frac{1}{2}\left|\frac{S_{N,i}}{\alpha_i} - \frac{S_{N,j}}{\alpha_j}\right| \tag{3.7}$$

As can be seen from (3.5) and (3.7) $\Delta S_{N,i}$, $\Delta S_{N,i,j}$ and are affected by harmonic currents and feeder impedance mismatch. Also, the voltage THD at the PCC can be written as

$$THD_{PCC} = \frac{1}{V_{pcc,1}}\sqrt{\sum_{h} |Z_{net,h}|^2 I_{sys,h}^2} \tag{3.8}$$

where $V_{pcc,1}$ is the fundamental component of the PCC voltage. The performance indices, given by (3.7) and (3.8), will be used in Section 3.4 to tune and evaluate the proposed $G_h - I_h$ droop characteristics.

To obtain an estimate for the highest possible error, a study is conducted on the microgrid shown in Figure 3.1 with two DGs. The considered DGs have similar ratings and

Table 3.1: Calculation of non-fundamental power sharing error.

rating	worst scenario			
	feeder length (km)	Cable Size (mm^2)	sharing error % (without shaping)	sharing error % (with proposed $R^{max}_{DG,i,h}$)
10 kVA	(0.8,0.1)	(25,4)	9.5	2.5
20 kVA	(1,0.2)	(70,16)	14.9	3.3
30 kVA	(1,0.2)	(120,25)	19.4	4.5
60 kVA	(0.9,0.1)	(240,25)	29.9	4.4

connected via different feeders to the PCC. To determine the highest harmonic currents, the nonlinear load is sized to be equal to the system rated load and its frequency spectrum is governed by the harmonic current limits of International Electrotechnical Commission (IEC) Standard 61000-3-4 [99].

To incorporate the effect of feeder impedance that complies with the worst scenario, feeder cables [41, 102] with different lengths up to the maximum normal length of low voltage distribution feeders are sized and checked for the worst feeder impedance scenario. Table 3.1 shows the DG and feeder specifications as well as the respective sharing errors. It is noted that the sharing error can reach 29.9% of fundamental apparent power which occurs in the case of two 60-kVA DGs connected to the PCC via 0.1 km and 0.9 km feeders.

The general solution employed to cope with the distribution of nonlinear loading is the suitable shaping of the converter output impedance [15–17, 23]. Since the uneven sharing of the nonlinear loads is mainly due to dissimilar distribution feeders, the designed DG harmonic resistance should be high enough to be dominant in contrast with the feeder impedance. From the other side, a high DG harmonic resistance may conflict with the voltage quality. Accordingly, a trade-off between the sharing accuracy and voltage quality is required, and that will be proposed in the next section.

Table 3.2: Harmonic limits for voltage and current.

Harmonic order			3	5	7	9	11	13	THD
Voltage %			5	6	5	1.5	3.5	3	8
Current %	Minimal Rsce [81]	600	40	30	20	14	12	10	57
		350	40	24	15	12	9	8	46
		250	34	18	12	10	8	7	39
		120	25	12	10	7	6	5	29
		33	22	11	7	4	3	2	26

3.4 Proposed DG Impedance Shaping Strategy

3.4.1 Constant Harmonic Resistance

A better trade-off between sharing accuracy and power quality can be approached by assigning specific values for each harmonic resistance. Achieving particular harmonic resistance (or conductance) is possible owing to the frequency selective feature of resonant controllers. However, the design procedure is not straight forward due to the unknown nature of microgrid nonlinear loads from both rating and spectrum views. The fact that the determined resistances should guarantee power quality constraints in supplying unknown nonlinear loads entails determining the maximum attainable value for each harmonic resistance, $R^{max}_{DG,i,h}$.

Calculation of this value requires harmonic voltage and current limits, thus

$$R^{max}_{DG,i,h} = \frac{V^{max}_{DG,i,h}}{I^{max}_{DG,i,h}} \tag{3.9}$$

where $V^{max}_{DG,i,h}$ and $I^{max}_{DG,i,h}$ are the maximum harmonic voltage and current limits, respectively.

Harmonic voltage limits have been developed by international standards [98, 100]. In this chapter, the compatibility levels for harmonic voltage from IEC 61000-2-2 are employed [100], as depicted in Table 3.2. To extract such benchmark for DG harmonic currents, the nonlinear loads should follow the emission limits of international standards [98–100]. The loads' compliance with such regulations leads to an upper limit for each DG harmonic current that will be obtained in this section. In this chapter, the harmonic current limits of IEC 61000-3-4 [99] are used. The standards bring load emission limits versus short circuit ratio (R_{sce}) which incorporates both distribution system short circuit power and

load rated apparent power. For ease of illustration, current harmonic limits for several values of R_{sce} are depicted in Table 3.2.

To utilize the current spectral distribution of Table 3.2, R_{sce} of each load feeder, i.e., emanating for the PCC to supply loads, is required. This value depends on the rating of the load feeder, which is known at the design stage, and the PCC short-circuit power. Thus, the maximum system demanding value for the h^{th} order harmonic current, i.e., $I^{max}_{sys,h}$, can be given by

$$I^{max}_{sys,h} = \frac{\sum_{j=1}^{n} I_{std,j,h} I_{rated,load,j}}{\sum_{j=1}^{n} I_{rated,load,j}} \sum_{i=1}^{m} I_{rated,DG,i} \tag{3.10}$$

where n is the number of load feeders; $I_{rated,load,j}$ is the rated current of the j^{th} load feeder in A; and $I_{std,j,h}$ is the upper current limit of the j^{th} load feeder for the h^{th} order harmonic, in per unit of its fundamental component.

Therefore, by considering the DG current rating as described by (3.6), the maximum harmonic current for each DG can be written as

$$I^{max}_{DG,i,h} = \alpha_i I^{max}_{sys,h} \tag{3.11}$$

Substituting (3.11) into (3.9), the maximum attainable harmonic resistance can be obtained. Using $R^{max}_{DG,i,h}$ in place of $Z_{DG,i,h}$ in (3.1), the sharing error improvement due to DG harmonic resistance shaping can be calculated by (3.7). The results of incorporating $R^{max}_{DG,i,h}$ in the previous study are shown in the last column of Table 3.1.

It should be noted $I_{sys,h}$ used in (3.1), is lower than $I^{max}_{sys,h}$ specified by (3.10). Relating these values can be performed using another multiplier incorporating the effect of system nonlinear load coincidence factor as

$$I_{sys,h} = k I^{max}_{sys,h} \tag{3.12}$$

where k denotes the system nonlinear loading factor.

It is worth nothing although (3.9) is considering the DG terminal, the voltage harmonics at the PCC and other target load buses can also be limited in accordance with the standards at the design stage, since the maximum harmonic currents and feeder impedances are known. The maximum harmonic current limits are determined using (3.10) and the feeder impedances can be extracted from the system data.

3.4.2 Droop-Based Harmonic Conductance

A family of droop characteristics in terms of harmonic conductance versus the root-mean-square (RMS) value of harmonic current is proposed. Two benefits can be achieved by increasing the harmonic conductance when the system nonlinear loading is reduced. First, the voltage quality is improved as can be noted from (3.8). By increasing the harmonic conductance or equivalently decreasing the harmonic resistance, the PCC total harmonic distortion will be decreased. Second, the sharing error of non-fundamental power is reduced. This is due to the direct relation between the harmonic resistance emulated by the droop characteristic and the harmonic current. For feeders with higher harmonic currents, larger harmonic resistances will be given by the droop characteristics and vice versa. This feature of the proposed droop characteristics is toward balancing the total harmonic impedance of different feeders that leads to an enhanced sharing.

The harmonic resistance obtained from each droop characteristic can be written as

$$R_{DG,i,h} = \left(G^{max}_{DG,i,h} - \frac{G^{max}_{DG,i,h} - G^{min}_{DG,i,h}}{I^{max}_{DG,i,h}} I_{oi,h} \right)^{-1} \tag{3.13}$$

where $G^{max}_{DG,i,h}$ and $G^{min}_{DG,i,h}$ are the maximum and minimum harmonic conductance of the i^{th} DG at the h^{th} order harmonic, respectively. Noting that $G^{min}_{DG,i,h}$ corresponds to the inverse of $R^{max}_{DG,i,h}$, i.e., defined by (3.9), thus

$$G^{min}_{DG,i,h} = \frac{1}{R^{max}_{DG,i,h}} \tag{3.14}$$

To exploit the distinctive features of the proposed droop characteristics, $G^{max}_{DG,i,h}$ should be properly tuned. For this purpose, we have to investigate the sharing error and voltage quality indices, i.e., $\Delta S_{N,i,j}$ and THD_{PCC}. Introducing the $G_h - I_h$ droop characteristics has a guaranteed voltage profile improvement by contrast to the constant harmonic conductance approach. Further, $G^{min}_{DG,i,h}$ or equivalently $R^{max}_{DG,i,h}$, has already been tuned by the method proposed in the previous subsection. Thus, for the whole range of the system nonlinear loading, voltage harmonic indices comply with the standard limits. An optimization-based approach is proposed to tune $G^{max}_{DG,i,h}$ with the main objective of minimizing the sharing error at different nonlinear loading levels, defined by k, as follows:

$$F = \min_{G^{max}_{DG,i,h}} \frac{1}{2} \sum_{k \in K} \sum_{j \neq i} \sum_{i} \Delta S_{N,i,j}(k)$$
$$\text{s.t.} \begin{cases} G^{max}_{DG,i,h} \geq G^{min}_{DG,i,h} \\ (4-1)-(4-3) \end{cases} \tag{3.15}$$

where $k \in K$ and K denotes a discrete set comprising values in the range [0, 1].

In this optimization problem, $G^{max}_{DG,i,h}$ should be greater or equal to $G^{min}_{DG,i,h}$ and the current harmonic flow equations described by (3.1)−(3.3) should be also satisfied. The above inequality constrained minimization problem is solved using MATLAB $fmincon$ function to calculate $G^{max}_{DG,i,h}$. The proposed optimization is done off-line and thus can incorporate all possible numbers of DGs at the design stage. It is worth noting that the above objective function indirectly considers different weights for harmonic currents because the harmonic currents follow the standard limits given by Table 3.2. As a result, the values obtained for $I^{max}_{sys,h}$ and $G^{min}_{DG,i,h}$ affect the optimization problem in proportion to the load harmonic spectrum.

3.5 Proposed Control Strategy

Figure 3.3 shows the block diagram of the proposed control strategy that tracks the target values of the DG harmonic conductance. As can be seen, the output current harmonics are controlled to get DG harmonic conductance. Also, to allow DG operation in islanding, its output voltage is regulated. The idea of hybrid voltage and current control has been introduced in [2,13] based on the selective feature of the resonant controllers and is modified here for nonlinear load sharing. Hybrid voltage and current controllers offer the following benefits not available with cascaded voltage-current controllers [16, 17]:

1. Ability to provide harmonic current control and voltage support through one controller.

2. Avoiding probable harsh transients in switching between grid-connected and islanding modes. Such transients are usually inevitable when the DG (i.e., working in current control mode) must change to voltage control mode.

3. Compensating the harmonic currents of local nonlinear loads by their dedicated DGs, without compromising the system performance in sharing common nonlinear loads.

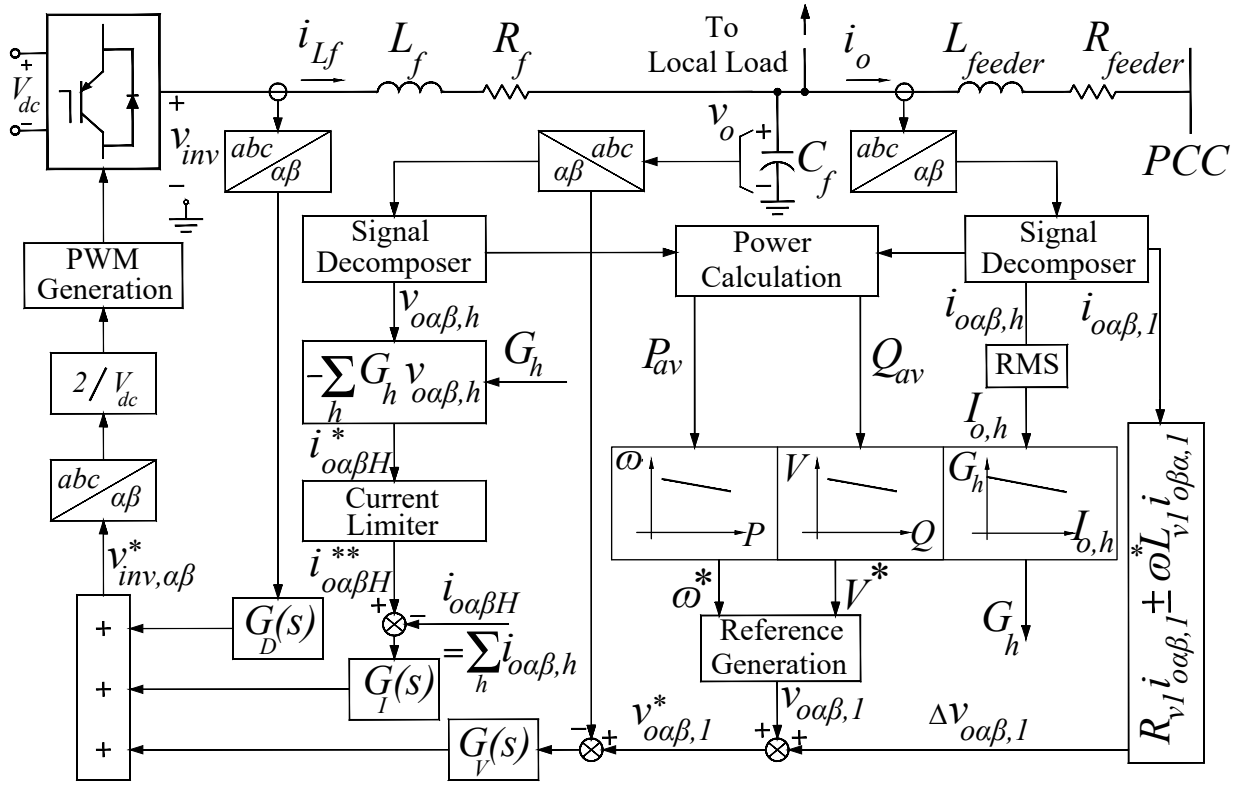

Figure 3.3: Block diagram of control strategy; droop based nonlinear load sharing.

The proposed control strategy adds the proposed $G_h - I_h$ droop characteristics to the basic $(\omega - P)$ and (V−Q) droop characteristics to equally share the fundamental and non-fundamental powers. The controller is implemented in the stationary $\alpha\beta$ reference frame to avoid complex frame transformations and to be equally applicable for single-phase and three-phase systems.

3.5.1 Signal Decomposition

It is required to selectively extract significant harmonics of DG terminal voltage and current. The decomposition method, proposed in [103], is employed for that purpose because of its numerous advantages such as fast response, small memory burden, high accuracy, and inherent ability to furnish in-quadrature signals used in stationary $(\alpha\beta)$ frame [104, 105]. It consists of two basic units: multiple second-order generalized integrators (MSOGI), and frequency-locked loop (FLL). The MSOGI unit is a set composed of several adaptive band-

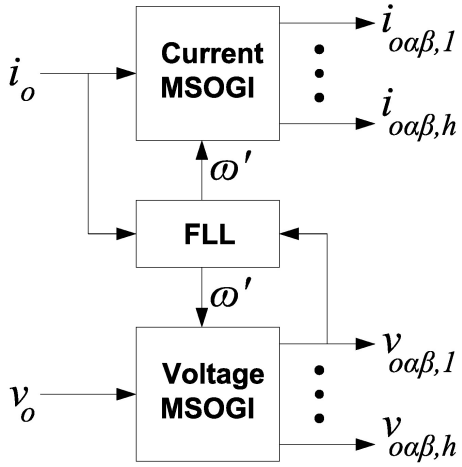

Figure 3.4: Structure of the voltage and current decomposer.

pass filters tuned to different frequencies that work in parallel. The transfer function of each filter is represented by

$$D_h = \frac{\sqrt{2}\,(h\omega')\,s}{s^2 + \sqrt{2}\,(h\omega')\,s + (h\omega')^2} \tag{3.16}$$

where ω' is the tuning frequency which is estimated by the FLL unit. Figure 3.4 shows the structure of the MSOGI-FLL decomposition method. A single unit of FLL, fed by the DG output voltage, is used to extract ω' which tunes the adaptive filters of two MSOGI units used for the voltage and current decomposition.

Based on the extracted harmonics of the DG terminal voltage and current, a hybrid control method is implemented. The schematic diagram of the hybrid control method is demonstrated in Figure 3.3. The output commands of the voltage and current loops are added together to build the converter modulator voltage $v^*_{inv,\alpha\beta}$. The voltage reference, $v^*_{o,\alpha\beta 1}$, is generated based on the conventional $\omega - P$ and V$-$Q droop characteristics, which are expressed by

$$\begin{cases} \omega^* = \omega_0 - D_p\,(P_0 - P_{av})\,; P_{av} = \langle v_{o\alpha,1} i_{o\alpha,1} + v_{o\beta,1} i_{o\beta,1} \rangle \\ V^* = V_0 - D_q\,(Q_0 - Q_{av})\,; Q_{av} = \langle v_{o\alpha,1} i_{o\beta,1} - v_{o\beta,1} i_{o\alpha,1} \rangle \end{cases} \tag{3.17}$$

where ω_0 and ω^* are the nominal and reference angular frequencies, respectively; and V_0 and V^* are the nominal and DG reference voltage amplitudes, respectively; D_p and D_q are the

droop coefficients; P_{av} and Q_{av} are DG supplied active and reactive powers, respectively; the symbol $\langle\rangle$ stands for the average value that is obtained by a first order low-pass filter with the cutoff frequency ω_c as $\frac{\omega_c}{s+\omega_c}$.

$$\begin{cases} \Delta v_{o\alpha,1} = R_{v1} i_{o\alpha,1} + \omega^* L_{v1} i_{o\beta,1} \\ \Delta v_{o\beta,1} = R_{v1} i_{o\beta,1} - \omega^* L_{v1} i_{o\alpha,1} \end{cases} \tag{3.18}$$

where R_{v1} and L_{v1} are the virtual resistance and inductance at the fundamental frequency.

The reference value for each harmonic current is obtained by multiplying its corresponding harmonic terminal voltage by the desired harmonic conductance specified by the proposed algorithm, i.e.,

$$i^*_{o\alpha\beta,h} = -G_h v_{o\alpha\beta,h} \tag{3.19}$$

Accordingly, a combined current reference can be calculated as

$$i^*_{o\alpha\beta,H} = -\sum_h G_h v_{o\alpha\beta,h} \tag{3.20}$$

To ensure DG overload protection, the current reference $i^*_{o\alpha\beta,H}$ is passed through a current limiter before being tracked by the current control loop. Figure 3.5 illustrates the current limiter which adaptively calculates the upper threshold for the rms value of the DG harmonic current $I_{H,lim}$:

$$I_{H,lim} = \sqrt{I^2_{rated} - I^2_C - I^2_{o,1}} \tag{3.21}$$

where I_{rated} is the DG rated current, $I_{o,1}$ is the rms value of fundamental component of the output current, and I_C is the rms value of the filter capacitor current. As shown in Figure 3.5, $I_{H,lim}$ is applied as an upper threshold of dynamic saturation block. The input to this block is I_H which is the rms value of the current reference $i^*_{o\alpha\beta,H}$. Its output $\bar{I}_H$ is determined based on

$$\bar{I}_H = \begin{cases} \bar{I}_H & I_H \le I_{H,lim} \\ I_{H,lim} & I_H > I_{H,lim} \end{cases} \tag{3.22}$$

Then, $\bar{I}_H$ manipulates an adaptive gain H_{gain}, i.e.,

$$H_{gain} = \frac{\bar{I}_H}{I_H} \tag{3.23}$$

Eventually, this adaptive gain is multiplied by $i^*_{o\alpha\beta,H}$ to generate the revised reference current $i^{**}_{o\alpha\beta,H}$:

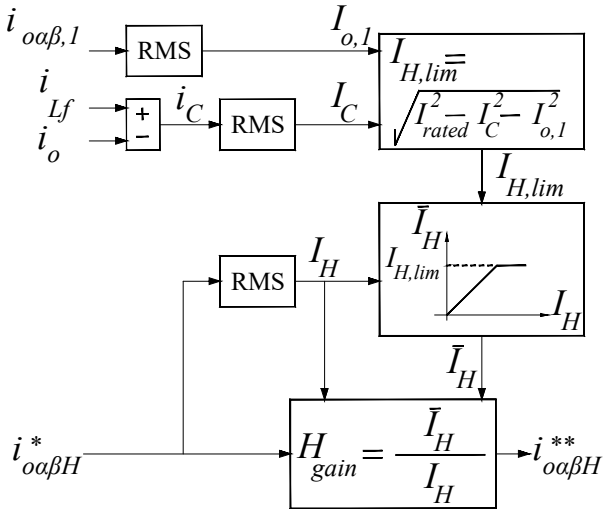

Figure 3.5: Structure of the current limiter.

$$i^{**}_{o\alpha\beta,H} = H_{gain} i^{*}_{o\alpha\beta,H} \tag{3.24}$$

It is worth noting that if the inverter rated current is not violated, $i^{**}_{o\alpha\beta,H}$ will be equal to $i^{*}_{o\alpha\beta,H}$.

To track the reference values of the fundamental voltage and harmonic currents in the $\alpha\beta$ reference frame, PR controllers are adopted [1]. The resonant frequency of PR controllers are adaptively tuned, as suggested in [106], to improve the controller performance during islanding, where the system frequency is drooped for active power sharing. To regulate the current reference given by (3.24), parallel resonant controllers are needed at different harmonic orders. Thus, the aggregated transfer function for the harmonic current controller is determined by

$$G_I(s) = \sum_h \frac{2K_{rh}s}{s^2 + 2\omega_{cut,h}s + (h\omega')^2} \tag{3.25}$$

Meanwhile, the transfer function of fundamental voltage controller is given by

$$G_V(s) = K_{pv} + \frac{2K_{r1}s}{s^2 + 2\omega_{cut,1}s + (\omega')^2} \tag{3.26}$$

where K_{pv} is the propositional gain. K_{r1} and K_{rh} are the resonant gains of the fundamental

and harmonic controllers, respectively. $\omega_{cut,1}$ and $\omega_{cut,h}$ are the cutoff bandwidths of the fundamental and harmonic controllers, respectively.

Equation (3.20) determines the DG harmonic current that realizes the target values of the harmonic conductance. Beside this duty for the DG current controller, the DG current should supply the harmonic content of its local nonlinear load, $i_{local,H}$. The harmonic currents of the local nonlinear load can be added to (3.20) to determine the total DG harmonic current reference. However, by considering the current summation as a control target, there is no guarantee that each individual current for the common and local loads will accurately follow their corresponding references. This limitation is associated with having two current references, i.e., $i^*_{o\alpha\beta,H}$ and $i^*_{local,H}$, to be tracked by only one control variable which is the DG modulated voltage, $v^*_{inv,\alpha\beta}$. To deal with this issue, it is proposed to control the DG feeder current, i.e., i_o shown in Figure 3.3, to follow (3.24). As a result, the controller will have just one current reference which is the harmonic current of the common load and the local nonlinear load will be directly fed by its corresponding DG.

The last signal that is added to the converter modulator input is the one used to damp the resonance of the LC filter. This signal is constituted by scaling the DG converter current [2]. Thus, the damping transfer function $G_D(s)$ can be given by

$$G_D(s) = -K_D \tag{3.27}$$

where K_D is the proportional gain of the resonance damping branch.

3.5.2 DG Thevenin Equivalent Model

To assure that the proposed control strategy can effectively track the target values of harmonic conductance, the DG Thevenin equivalent model is derived. The LC interfacing filter, shown in Figure 3.3, can be modelled by

$$\begin{cases} L_f \frac{di_{Lf}}{dt} = v_{inv} - v_o - R_f i_{Lf} \\ C_f \frac{dv_o}{dt} = i_{Lf} - i_o \end{cases} \tag{3.28}$$

where v_{inv} is the inverter voltage, i_{Lf} is the current through the filter inductor. By mapping (3.28) into the Laplace domain and combining the model equations to eliminate i_{Lf}, one can obtain

$$\left(L_f C_f s^2 + R_f C_f s + 1\right) V_o = V_{inv} - (L_f s + R_f) I_o \tag{3.29}$$

On the other hand, V_{inv} is equal to V^*_{inv} that is expressed by the voltage control law of Figure 3.3 as

$$V^*_{inv} = -K_D I_{Lf} + G_v \left(V^*_o - V_o\right) + G_I \left(I^*_{oH} - I_{oH}\right) \tag{3.30}$$

From (3.20), I^*_{oH} is given by

$$I^*_{oH} = -\sum_h G_h V_{oh} \tag{3.31}$$

The voltage harmonics in (3.20) are influenced by the signal decomposer dynamics. Thus, in order to embed the above equation into modelling, a transfer function of each voltage component has to be included. To facilitate this process, the values of G_h are assumed equal (i.e., $G_h = G_0 \ \forall h$). As long as the modelling target is to evaluate the controller performance, this simplification does not lose any generality. Hence, (3.31) can be rewritten as

$$I^*_{oH} = -G_0 \left(V_o - V_{o,1}\right) \tag{3.32}$$

The equivalent transfer function H of the signal decomposer is extracted in [103] as a function of D_h:

$$H \triangleq \frac{V_{o,1}}{V_o} \triangleq \frac{I_{o,1}}{I_o} = D_1 \prod_{h=2}^{n} \frac{1 - D_h}{1 - D_1 D_h} \tag{3.33}$$

By substituting from (3.33) in (3.32), the reference harmonic current can be described by

$$I^*_{oH} = -G_0 \left(1 - H\right) V_o \tag{3.34}$$

Analogously, the harmonic content of the DG output current can be calculated by

$$I_{oH} = I_o - I_{o,1} = I_o - H I_o = \left(1 - H\right) I_o \tag{3.35}$$

By substituting (3.34) and (3.35) into (3.30) and then using the resulted V_{inv} into (4-29), the Thevenin equivalent model of a DG can be given by

$$V_o = G V^*_o \ - Z_{th} I_o \tag{3.36}$$

where

$$\begin{aligned} G &= \frac{G_V}{L_f C_f s^2 + s\left(R_f + K_D\right) C_f + G_0 G_I (1-H) + G_V + 1} \\ Z_{th} &= \frac{G_I + K_D + R_f + s L_f}{L_f C_f s^2 + s\left(R_f + K_D\right) C_f + G_0 G_I (1-H) + G_V + 1} \end{aligned} \tag{3.37}$$

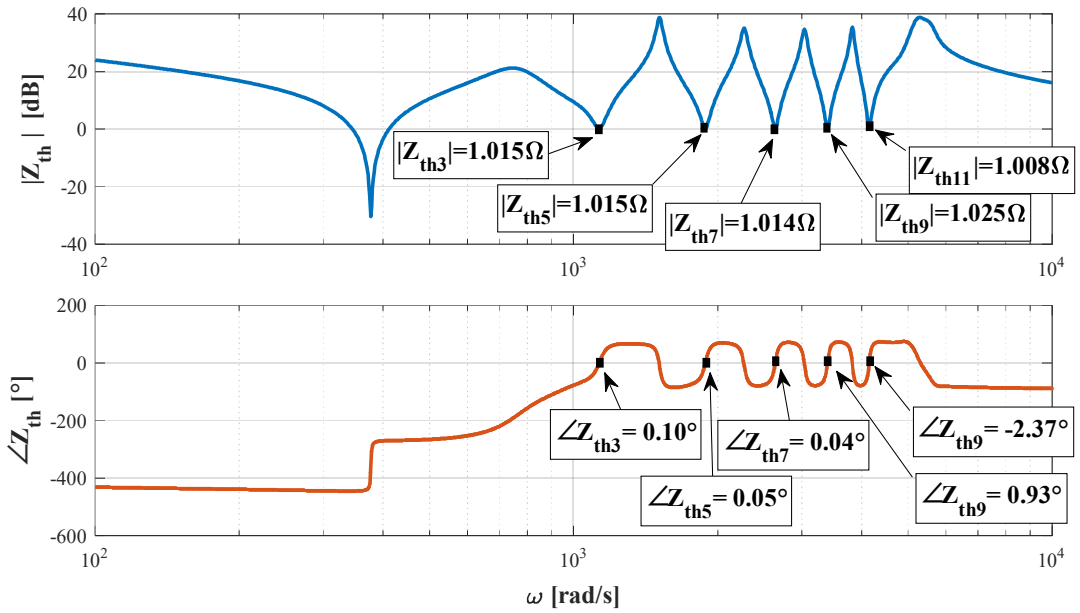

Figure 3.6: The DG output impedance.

Figure 3.6 shows the bode plot of the DG output impedance when the reference values of harmonic conductance are equal to 1 mho, i.e., corresponds to 1Ω at all harmonic orders. As can be seen, the controller is able to reach the reference values with high accuracy which validates the effectiveness of the proposed control strategy in shaping the DG harmonic conductance.

3.6 Performance Evaluation

This section evaluates the effectiveness of the proposed control algorithm. Simulated by MATLAB/Simulink, the performance of the microgrid, shown in 3.1, is examined. This microgrid includes two DGs with similar power ratings. The microgrid parameters are given in Appendix A.

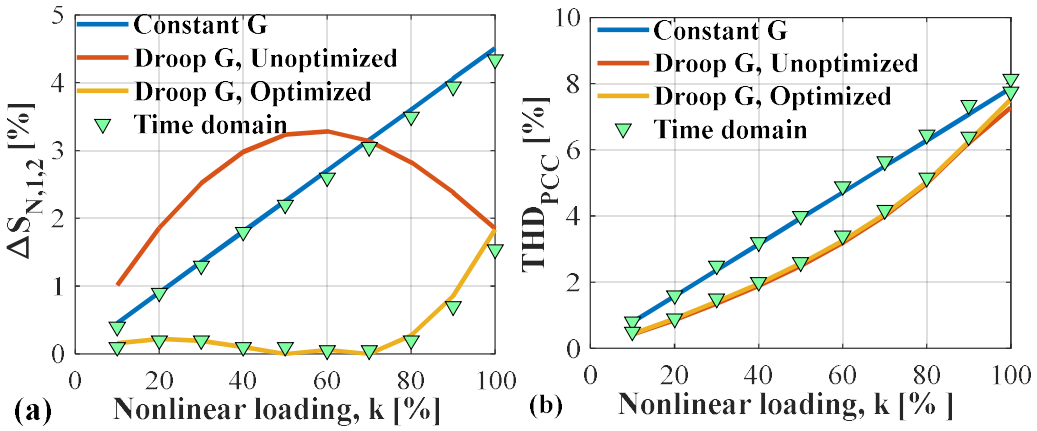

Figure 3.7: Performance evaluation the proposed droop-based and constant harmonic conductance methods: (a) sharing error, (b) voltage THD.

3.6.1 Nonlinear Load Sharing

Figure 3.7 demonstrates a comparison between the performance of the constant harmonic conductance and droop-based harmonic conductance approaches under different nonlinear loadings. Also, the importance of the proposed optimization method for tuning the droop-based harmonic conductance is illustrated. Those methods are contrasted with respect to the sharing error of non-fundamental power, as shown in Figure 3.7(a), and the voltage THD as displayed in Figure 3.7(b). The results obtained by the developed model in (3.1) – (3.7) and time-domain simulations are matching which proves the accuracy of the proposed harmonic current flow.

As demonstrated in Figure 3.7, the proposed droop-based technique with the aid of the suggested optimal tuning method offers superior performance at all nonlinear loading conditions. The proposed droop-based method that is optimally tuned offers a near-zero sharing error for nonlinear loading factors below 70%. Moreover, the reduction in the sharing error can be as high as 3% at nonlinear loading greater than 70%. Further, using the proposed optimized droop-based conductance, the voltage THD is improved by more than 1% for a significant range of the nonlinear loading factors. For instance, when k equals 50%, the THD is almost 1.5% lower than the value obtained by the constant conductance approach.

In order to show the significance of applying the proposed optimization method, the

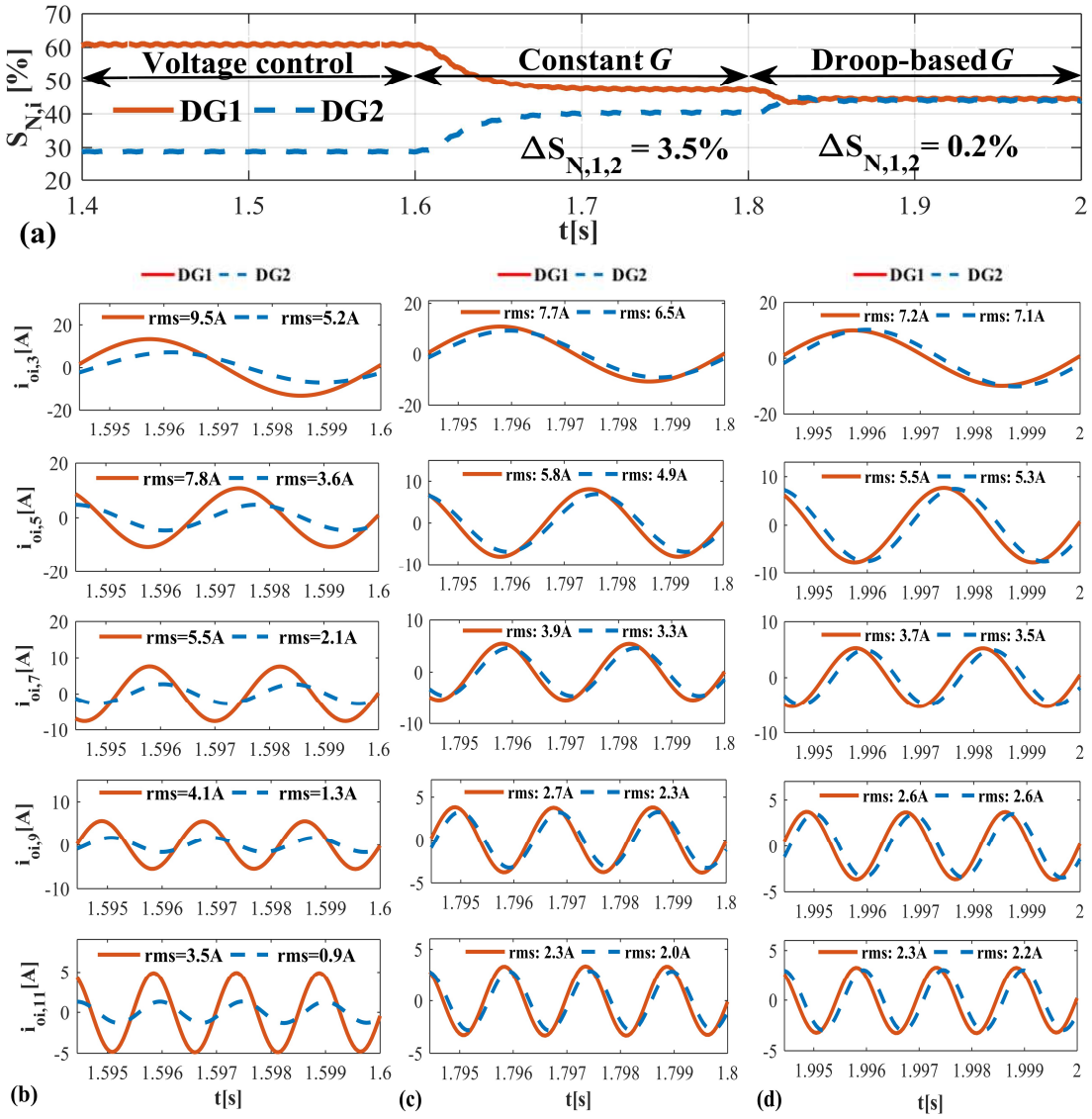

Figure 3.8: DGs non-fundamental powers and line current harmonic components for non-linear loading of 80%: (a) powers; harmonic currents for (b) conventional voltage control, (c) constant harmonic conductance, (d) droop-based harmonic conductance.

sharing error and the THD are also displayed in Figure 3.7 for the case where $G^{max}_{DG,i,h}$ is

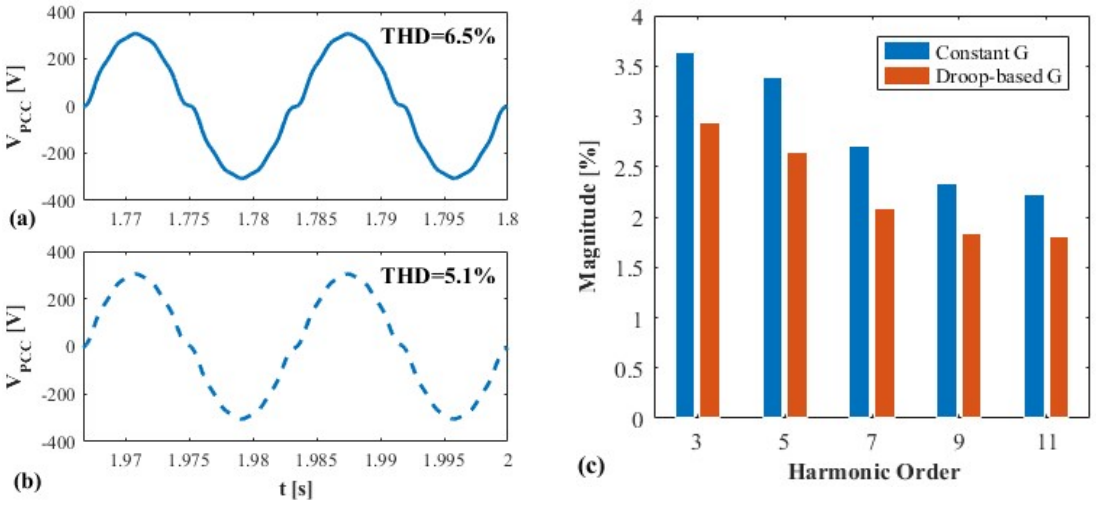

Figure 3.9: PCC voltage at 80% nonlinear loading. (a) constant harmonic conductance, (b) droop-based harmonic conductance, (c) voltage spectrum.

unoptimized (for instance, $G^{max}_{DG,i,h}$ equals to 3 times $G^{min}_{DG,i,h}$ at each harmonic order). By contrast with the optimized $G^{max}_{DG,i,h}$, the THD remained almost constant. However, the unoptimized selection of $G^{max}_{DG,i,h}$ resulted in a significantly higher sharing error compared with the optimized $G^{max}_{DG,i,h}$.

Figure 3.8(a) demonstrates the DG non-fundamental powers when k is 80%. The DGs are controlled with the conventional voltage control mode from 1.4(s) to 1.6(s) in which all elements of PR controller banks are used in the voltage control loop [16]. As can be seen, the system faces a significant sharing error of about 16%. After 1.6(s), the hybrid control of voltage and current is used to shape the DG harmonic conductance. With the help of the constant harmonic conductance, the sharing error decreases without exceeding the standard voltage distortion limit. However, the constant harmonic conductance can only decrease the sharing error to 3.5%. Whereas, the sharing error is reduced to a negligible value of 0.2% when activating the proposed droop based method from 1.8(s) to 2(s). Also, Figures 3.8(b), 3.8(c), and 3.8(d) reveal that among the three different control techniques described above, the proposed droop-based method leads to the best performance in terms of harmonic current sharing. The RMS values of DGs' harmonic currents are relatively equal using the proposed droop-based approach. Moreover, Figure 3.9 illustrates the PCC voltage waveform and harmonic spectrum for the constant harmonic conductance and

droop-based approaches. Using the proposed droop-based method, the voltage harmonics are reduced by about 20% which leads to 1.4% decrease in voltage THD.

3.6.2 Supplying Local Nonlinear Loads

To demonstrate the advantage of the proposed controller in dealing with local nonlinear loads, another case study is conducted. In this study, one of the DGs supplies a 2 kW local nonlinear load and accordingly has an extra capacity for this purpose. The rest of DG capacity should participate in supplying the common nonlinear load. All other system parameters are similar to the previous case study. Initially, the DGs are controlled in the voltage control mode. Due to the very low values of DG harmonic resistances, resulted by the bank of PR controllers in the voltage loop, the harmonic currents of the local load are short-circuited by the DG and will not affect the network. As a result, the non-fundamental power in Figure 3.8(a) and Figure 3.10(a) are almost the same from 1.4(s) to 1.6(s).

From 1.6(s) to 1.8(s), the DGs are governed by the harmonic resistance shaping method proposed in [23]. This time span should be compared with the next 0.2(s) in which the DGs are controlled by the proposed droop-based method with local load compensation. Figure 3.10(a) and (b) reveal that the controller proposed in [23] cannot completely compensate the local nonlinear loads, thus, their demanded power should flow within the microgrid. As a result, a significant sharing error of 8.7% occurs compared to 0.2%, i.e., resulted when applying the proposed droop-based approach with local load compensation.

Comparing Figure 3.8(d) and Figure 3.10(d) shows that despite the presence of local nonlinear loads, the harmonic current sharing of the common nonlinear load is almost unaffected. That justifies the effectiveness the proposed droop-based method in supplying the local nonlinear loads, and concurrently, sharing the common nonlinear load. Further, as shown in Figure 3.11, the devastating impact of the flow of local load harmonic currents in the microgrid leads to 2.1% increase in the THD in contrast to the proposed droop-based method that shows superior performance.

3.6.3 Real-Time Simulation

To demonstrate the effectiveness of the proposed control method in real-time, the case study in Section 3.6.1 is tested experimentally using OPAL real-time simulators (RTS). RTS can perform powerful computations with high accuracy and low cost real-time execution. In addition, it increases the system reliability by increasing the test coverage and integrating

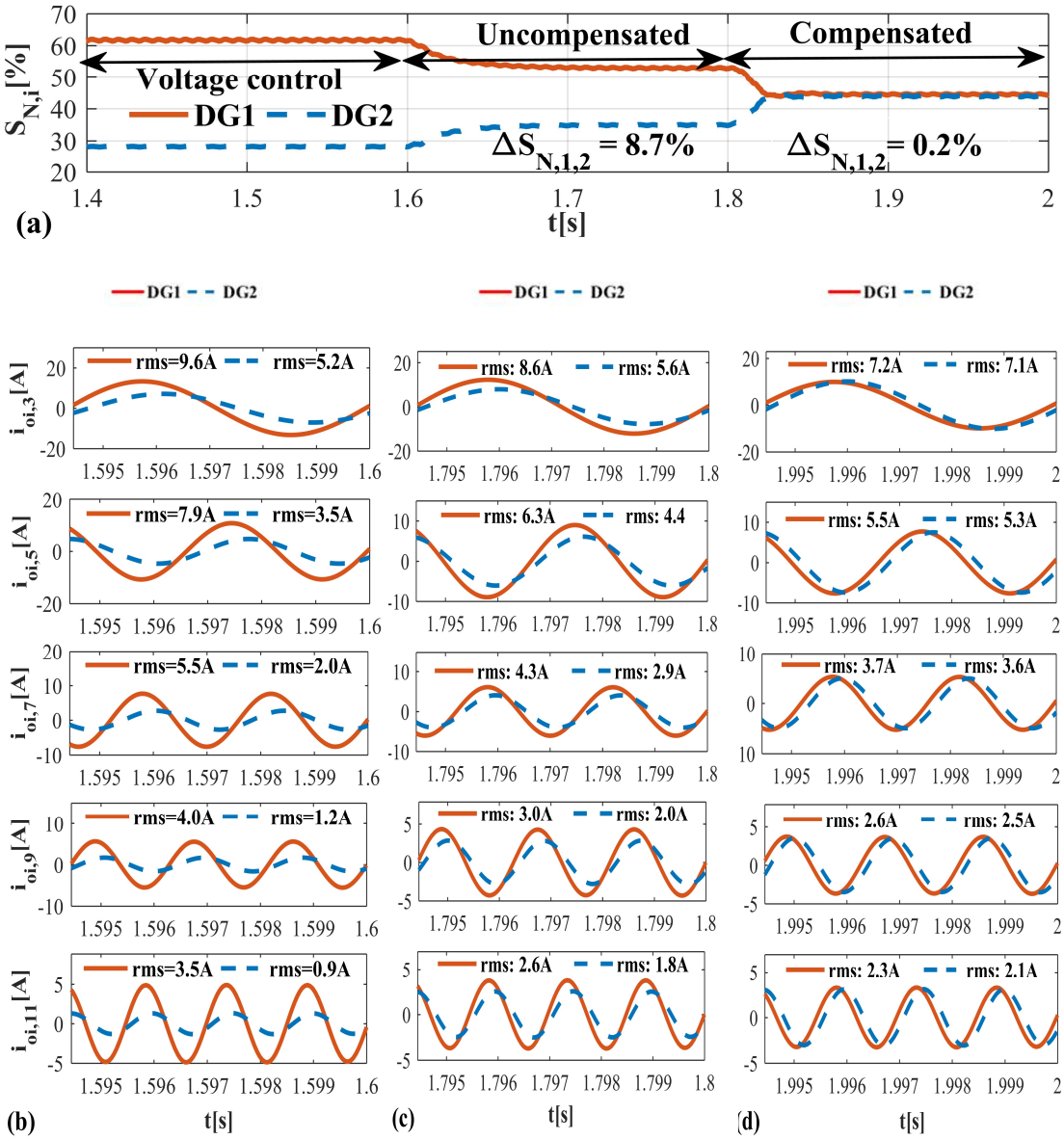

Figure 3.10: DGs non-fundamental powers and line current harmonic components for the 2kW nonlinear local load: (a) powers; harmonic currents for (b) conventional voltage control, (c) constant harmonic conductance, (d) droop-based harmonic conductance.

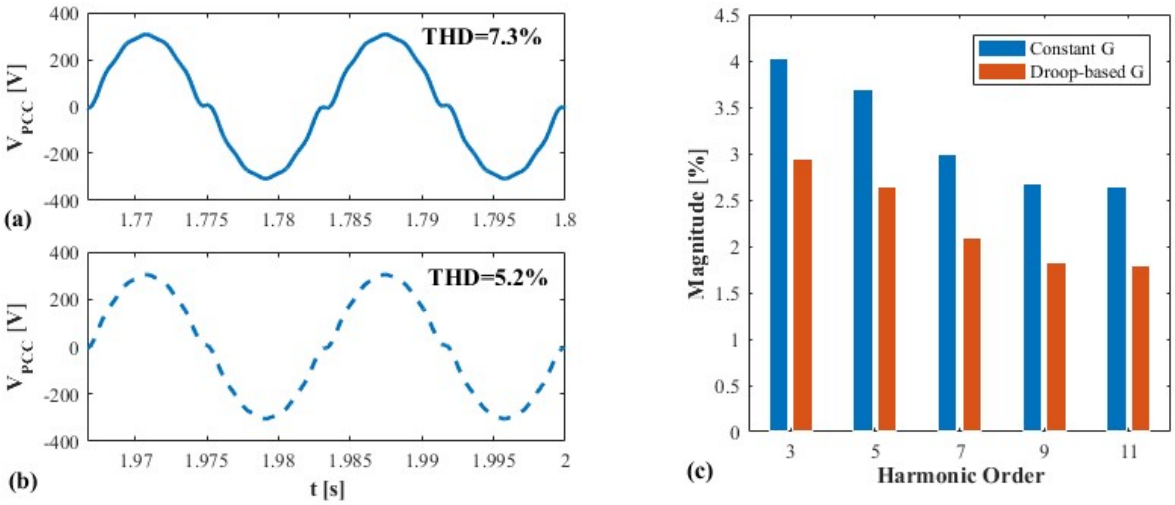

Figure 3.11: PCC voltage waveforms for compensated and uncompensated 2kW nonlinear local load: (a) constant harmonic conductance, (b) droop-based harmonic conductance, (c) voltage spectrum.

other control and protection systems. Typically, controllers are tested in real-time using OPAL RTS via two applications [107, 108]:

1. Rapid control prototyping (RCP) where a physical controller is implemented using the RTS and then connected to a physical system for testing. The main advantages of implementing the controller using the RTS are: flexibility, and ease of implementation and debugging.

2. Hardware-in-the-loop (HiL) where the physical controller is connected to a virtual system modelled using the RTS. This physical controller can be realized using another processor within the RTS, i.e., creating a RCP, or any DSP-based controller. The controller and virtual plant are connected in real-time through I/O channels.

Two cores (i.e, CPU1 and CPU2) within an OPAL RTS were employed for conducting the HiL application to test the proposed DG controller, as illustrated in Figure 3.12. The DG controller was emulated using CPU1, producing a rapid control prototyping (RCP) and exchanging real-time data with the virtual network modeled in CPU2. The test system and the controller were built using Simulink/SimPower Systems along with ARTEMiS plug-in

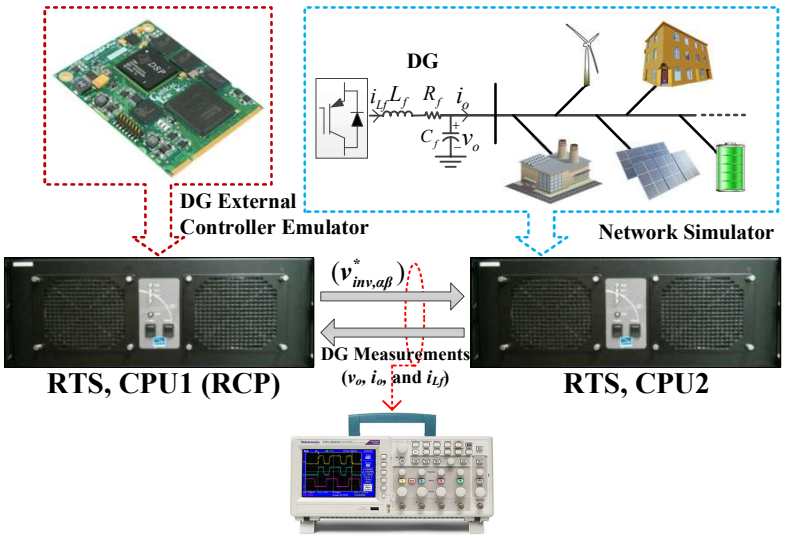

Figure 3.12: HiL setup.

from OPAL. In this chapter, the RTS models were run with a fixed-step sampling time of 10μs. More details about OPAL-RT and HiL applications are available in [109–111].

Figure 3.13(a) illustrates the non-fundamental powers at three control modes for the DGs, i.e., voltage control, constant conductance, and droop-based conductance. Initially, the DGs were operating at the voltage control mode, in which, the system suffered from high sharing error between the DG non-fundamental powers (i.e., 16.3%). By switching to the constant conductance control mode, the sharing error was reduced to 3.6%. By contrast, the proposed droop-based conductance method could offer superior results in distributing the nonlinear load among the DGs by reducing the sharing error to 0.2%. Figure 3.13(b) demonstrates the PCC voltage when the proposed droop-based conductance method was employed by the DGs. The THD of the PCC voltage is limited to 5.3% which complies with the standards. Lastly, Figure 3.13(c) displays the DG currents in the case of droop-based conductance. The accurate sharing of the current proves the effectiveness of the proposed method in sharing the harmonic currents.

3.7 Conclusion

In this chapter, a family of harmonic droop characteristics in terms of harmonic conductance versus harmonic current has been proposed to deal with the problem of nonlinear load

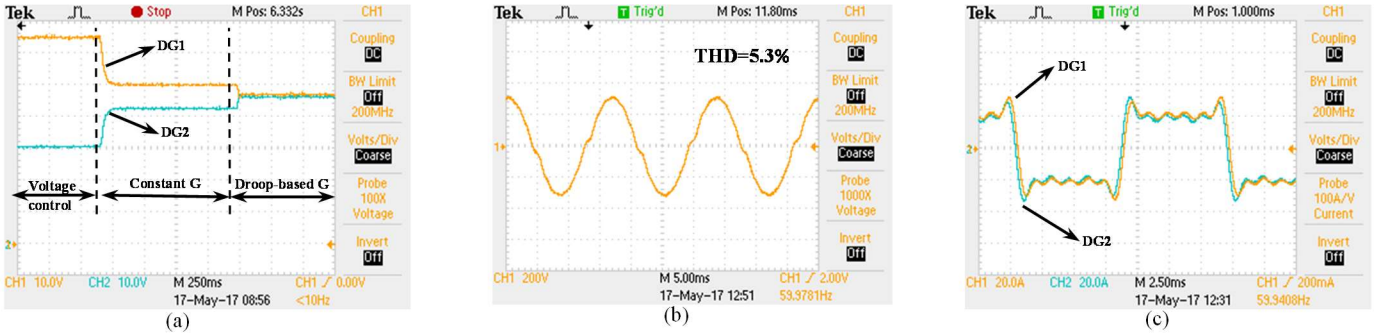

Figure 3.13: HiL results: (a) Non-fundamental powers of DGs, (b) PCC voltage for droop-based harmonic conductance, (c) DG currents for droop-based harmonic conductance.

sharing. The problem has been mathematically formulated and the worst case scenario has been generated. To cope with the unknown nature of microgrid nonlinear loads, a method based on the upper limits of load harmonic contents has been introduced. An optimal tuning method for the droop characteristics has been developed to minimize the sharing error. An adaptive hybrid voltage and current control method is adopted to realize the droop characteristics. The DG Thevenin model has been derived to validate the controller effectiveness in shaping the DG harmonic conductance. It has been proven by comparative evaluation that the proposed droop-based approach can offer an accurate nonlinear load sharing as well as enhanced voltage profile. In addition, the proposed control technique is able to compensate local nonlinear loads using their dedicated DGs without compromising the system performance.

Chapter 4

Optimal Planning of Distributed Generators and Shunt Capacitors in Isolated Microgrids with Nonlinear Loads

4.1 Introduction

This chapter[1] presents a comprehensive design procedure for isolated microgrids penetrated with nonlinear loads. The proposed microgrid planning approach simultaneously determines the sizes, locations and types of distributed generators (DGs) and shunt capacitor banks (CBs). The presence of nonlinear loads along with the capacitors of CBs or DGs' output filters may cause severe voltage distortions. To consider this issue, a harmonic power flow tool tailored for planning applications is developed that takes into account the specific features of isolated microgrids. Given the necessity of supply continuity for isolated microgrids after a contingency, the proposed planning approach takes into consideration the reliability to increase the probability of building successful islands. Unlike previous methods, the proposed approach does not rely merely on supply adequacy, and takes into account the fact that the voltage provision requirement can only be fulfilled through dispatchable DGs. The intermittent natures of loads and renewable DGs are

[1] A version of this chapter has been published: A. H. Yazdavar, M. Shaaban, E. F. El-Saadany, M. M. A. Salama, and H. H. Zeineldin, "Optimal Planning of Distributed Generators and Shunt Capacitors in Isolated Microgrids with Nonlinear Loads", *IEEE Trans. on Sustainable Energy, in press.*

modelled probabilistically. The effectiveness of the proposed planning approach has been validated using the PG&E 69-bus system.

4.2 Contributions

This chapter proposes a planning platform for isolated microgrids with nonlinear loads to simultaneously allocate DGs and CBs, considering the specific features of isolated microgrids. The main contributions of this chapter are as follows:

- Simultaneously allocating DGs and CBs while considering the power quality constraints.
- Considering the specific features of isolated microgrids in fundamental and harmonic power flow algorithms, including the lack of a slack bus, and the droop-based nature of some DGs. The impacts of droop-based operation on the power flow, and in particular, the inherent sharing error assigned to the voltage-reactive power droop characteristic are included in the planning. This is performed by embedding an appropriate power flow algorithm in the planning formulation.
- Modelling of wind turbines in the harmonic power flow to take into account the possibility of resonance that might happen in the presence of wind turbines, capacitor banks and nonlinear loads. This is done by including the Thevenin equivalent impedance of wind turbines in the harmonic analysis.
- Developing a reliability-based technique to build successful islands with dynamic borders, as a consequence of contingency. The proposed technique takes into consideration the voltage provision requirement for an island to be successful, and accordingly, distributes the dispatchable DGs throughout the microgrid.

4.3 Problem Formulation

In this section, the mathematical model of the proposed planning problem for allocation of DGs and CBs is described. The problem is formulated as a mixed-integer non-linear programming (MINLP). The following assumptions are made: 1) The problem is an expansion planning one in which the available microgrid network is initially supplied by

diesel-generator units connected to the generating bus. Due to ageing, the diesel generators are to be replaced by new units. 2) DGs' and CBs' capacities are discretized at definite steps. 3) All DGs belong to the same entity. 4) The renewable DGs are assumed to operate at unity power factor to harvest their maximum available power.

4.3.1 Objective Function

The planning objective is to minimize the total expected cost, once annualized over the planning horizon, considering the probability of each generation-load state. The derivation of generation-load model is explained in Section 4.6. Considering the decision variable $\mathcal{X}$ as the sizes, locations, and types of DGs and CBs, the objective function is described by

$$\min_{\mathcal{X}} \sum_{s \in \mathcal{S}^S} \Pr_s \left(C^C + O_s^C + M^C \right) \tag{4.1}$$

where C^C,O_s^C, M^C are the annualized capital, operational and maintenance costs, respectively.

Annualizing the costs is performed using two factors: capital recovery factor (CRF) and levelizing factor (LF) [112]. CRF is used to annualize the capital cost, and LF is applied to convert the escalating annual operational and maintenance costs into a series of equal amounts. These factors are given by

$$CRF = \frac{i(1+i)^n}{(1+i)^n - 1} \tag{4.2}$$

$$LF = \frac{(1+d')^n - 1}{d'(1+d')^n} \frac{d(1+d)^n}{(1+d)^n - 1} \tag{4.3}$$

where i and d are the interest and discount rates, respectively; and $d' = (d-e)\,/\,(1+e)$, where e is the escalation factor.

The cost terms in (4.1) can be written as

$$\begin{aligned} C^C = & CRF \left(\sum_{db \in \mathcal{S}^{DB}} \sum_{dr \in \mathcal{S}^{DR}} x_{db,dr} C_{dr}^C + \right. \\ & \left. \sum_{wb \in \mathcal{S}^{WB}} \sum_{wr \in \mathcal{S}^{WR}} x_{wb,wr} C_{wr}^C + \sum_{cb \in \mathcal{S}^{CB}} \sum_{cr \in \mathcal{S}^{CR}} x_{cb,cr} C_{cr}^C \right) \end{aligned} \tag{4.4}$$

$$O_s^C = LF\left(\sum_{day=1}^{365}\sum_{hr=1}^{24}\sum_{db\in\mathcal{S}^{DB}}\sum_{dr\in\mathcal{S}^{DR}} x_{db,dr}P_{d,t,s}H^R F^C\right) \tag{4.5}$$

$$M^C = LF\left(\sum_{db\in\mathcal{S}^{DB}}\sum_{dr\in\mathcal{S}^{DR}} x_{db,dr}M_{dr}^C + \sum_{wb\in\mathcal{S}^{WB}}\sum_{wr\in\mathcal{S}^{WR}} x_{wb,wr}M_{wr}^C\right) \tag{4.6}$$

where C_{dr}^C, C_{wr}^C, and C_{cr}^C are the capital costs of diesel generators, wind turbines, and capacitor banks, respectively; M_{dr}^C and M_{wr}^C are the maintenance costs of diesel generators and wind turbines, respectively; F^C is the fuel cost; H^R is the heat rate; $P_{dr,t,s}$ is the active power of diesel generator dr, at time t for state s; $x_{db,dr}$ is the binary variable for installing diesel generator dr at candidate bus db; $x_{wb,wr}$ is the binary variable for installing wind turbine wr at candidate bus wb; $x_{cb,cr}$ is the binary variable for installing capacitor bank cr at candidate bus cb; db, wb, and cb are the indices for candidate buses of diesel generators, wind turbines and capacitor banks, respectively; dr, wr, and cr are the indices for available ratings of diesel generators, wind turbines and capacitor banks; $\mathcal{S}^{DB}$, $\mathcal{S}^{WB}$, and $\mathcal{S}^{CB}$ are the sets of candidate buses for diesel generators, wind turbines, and capacitor banks, respectively; $\mathcal{S}^{DR}$, $\mathcal{S}^{WR}$, and $\mathcal{S}^{CR}$ are the sets of available ratings for diesel generators, wind turbines, and capacitor banks, respectively; y, day, and hr are the indices for year, day, and hour, respectively; t is the index for time $[y, day, hr]$; s is the index for combined states of wind-power generation and load.

4.3.2 Constraints

4.3.2.1 Power Flow Equations

Equations (4.7) and (4.8) describe the balancing constraints of active and reactive powers, respectively. In these equations, the terms describing the injected powers are defined by (4.9)–(4.14): the active and reactive powers of the lines (4.9, 4.10), the active power of wind turbines (4.11), the reactive power of capacitor banks (4.12), and the active and reactive powers of diesel generators (4.13, 4.14). Additionally, the power flow equations of isolated microgrids should account for the lack of a slack bus, and the droop-based operation of some DGs. The study conducted in [93] has shown that these characteristics impact: 1) the microgrid frequency, and consequently, bus voltages' angles and the flow of power and 2) the bus voltages' magnitudes. Further, obtaining accurate results entails the application

of a different power flow algorithm than the conventional one.

It is emphasized here that the above-mentioned characteristics must be embedded in the planning of isolated microgrids for the following reasons: 1) to investigate more accurately the planning constraints, and more importantly, 2) to account for the impact of voltage-reactive power droop characteristic. Although the droop characteristics, frequency-active power and voltage-reactive power, are employed to evenly distribute loads' active and reactive powers among generators, the error of reactive power sharing can be significant [113]. This error is a function of DGs' locations and their feeder impedances [114], and thus, must be considered in the planning. To account for the effect of droop characteristics, (4.15) and (4.16) are applied, whose droop slopes are given by (4.17) and (4.18), respectively, and are defined in terms of generator ratings and the permissible frequency and voltage drops. On the one hand, the optimization decision variable also includes the ratings of dispatchable DGs, and thus, they are known in each evaluation of the optimization objective function (4.1). On the other hand, the permissible frequency and voltage drops for the design of droop characteristics are inputs to the planning problem. Therefore, the slopes of droop characteristics are acquired with which the droop equations are determined using (4.15) and (4.16), and are merged into the power balance equations (4.7) and (4.8) through (4.13) and (4.14). One should note that (4.13) and (4.14) are used for the fact that DGs' ratings are selected among a set of discrete values. Another constraint on the reactive power of droop-based DGs will be added in Part 2 of this subsection.

$$P^I_{b,t,s} + P^W_{b,t,s} + P^D_{b,t,s} - P^L_{b,t,s} = 0, \forall b, t, s \tag{4.7}$$

$$Q^I_{b,t,s} + Q^C_{b,t,s} + Q^D_{b,t,s} - Q^L_{b,t,s} = 0, \forall b, t, s \tag{4.8}$$

$$P^I_{b,t,s} = \sum_{k=1}^{N^B} V_{b,t,s} V_{k,t,s} Y_{bk,s} \cos\left(\delta_{b,t,s} - \delta_{k,t,s} - \theta_{bk,t,s}\right) \tag{4.9}$$

$$Q^I_{b,t,s} = \sum_{k=1}^{N^B} V_{b,t,s} V_{k,t,s} Y_{bk,s} \sin\left(\delta_{b,t,s} - \delta_{k,t,s} - \theta_{bk,t,s}\right) \tag{4.10}$$

$$P^W_{b,t,s} = \sum_{wr \in \mathcal{S}^{WR}} x_{b,wr} P_{wr,t,s} \tag{4.11}$$

$$Q^C_{b,t,s} = \sum_{cr \in \mathcal{S}^{CR}} x_{b,cr} y_{b,cr,s} Q_{cr,t,s} \tag{4.12}$$

$$P^D_{b,t,s} = \sum_{dr \in \mathcal{S}^{DR}} x_{b,dr} P_{dr,t,s} \tag{4.13}$$

$$Q^D_{b,t,s} = \sum_{dr \in \mathcal{S}^{DR}} x_{b,dr} Q_{dr,t,s} \tag{4.14}$$

$$P_{dr,t,s} = \frac{1}{m^P_{dr}} \left(\omega^{nom} - \omega_{t,s}\right) \tag{4.15}$$

$$Q_{dr,t,s} = \frac{1}{m^Q_{dr}} \left(V^{nom} - V_{t,b,s}\right) \tag{4.16}$$

$$m^P_{dr} = \frac{\Delta\omega^{per}}{S_{dr}} \tag{4.17}$$

$$m^Q_{dr} = \frac{\Delta V^{per}}{S_{dr}} \tag{4.18}$$

where $P_{dr,t,s}$ and $Q_{dr,t,s}$ are the active and reactive powers of diesel generator dr, at time t for state s, respectively; $P_{wr,t,s}$ is the power injected by wind turbine wr, at time t for state s; $P^I_{b,t,s}$ and $Q^I_{b,t,s}$ are the active and reactive powers injected by the network into bus b, at time t for state s, respectively; $P^L_{b,t,s}$ and $Q^L_{b,t,s}$ are the active and reactive powers of bus b load, at time t for state s, respectively; V and δ are the bus voltage magnitude and phase angle, respectively; bk is the index for the feeder between buses b and k; Y_{bk} and θ_{bk} are the admittance magnitude and angle between buses b and k, respectively; ω^{nom} and V^{nom} are then nominal frequency and voltage; $\Delta\omega^{per}$ and ΔV^{per} are the permissible frequency drop and voltage drop, respectively; S_{dr} and S_{cb} are the ratings of diesel generator dr and capacitor bank cb, respectively; $y_{cb,cr,s}$ is the binary variable for switching capacitor bank cr at candidate bus cb for state s; m^P_{dr} is the droop gain of $\omega - P$ characteristic for diesel generator dr; m^Q_{dr} is the the droop gain of $V - Q$ characteristic for diesel generator dr; b is the index for bus; $b \in \mathcal{S}^B$ and $s \in \mathcal{S}^S$;

It should be noted in the microgrids' power flow equations, described above, instead of slack and PV buses, one must deal with droop buses, which are those connected to dispatchable generators. For droop buses, neither active powers nor voltage magnitudes are known parameters, and they are to be determined through the droop characteristics of frequency-active power and voltage-reactive power, respectively. Thus, each droop bus introduces four unknowns, i.e., its active and reactive powers as well as voltage's magnitude and angle. Equations (4.15) and (4.16) relate bus active and reactive powers to the microgrid's operational frequency and bus voltage's magnitude, respectively, and accordingly, two unknowns are remained per each bus along with the operational frequency. On the other hand, the angle of one droop-bus voltage is considered as the reference angle, and therefore, one unknown is diminished from those of droop buses. This practically makes two unknowns per each droop bus. Apart from droop buses, in microgrids' power flow

algorithm, the rest of buses are considered as PQ, with two unknowns in the power flow equations, i.e., voltage's magnitude and angle. Therefore, the microgrids' power flow equations include $2N^B$ unknowns, which are obtained through the optimization sub-problem as will be explained in Subsection 4.7.2.

4.3.2.2 Network's Elements

An additional set of constraints is related to the network's elements, including the capacity of DGs, CBs, and feeders along with the penetration level of renewable DGs and bus voltage limits, as given by (4.19)–(4.25). Specifically, (4.21) recommends considering zero as the minimum reactive power limit of diesel generators, i.e., only over-excited behaviour is allowed for isolated microgrids, for the following reason. According to the voltage-reactive power droop characteristic, as given by (4.16), if the voltage of a diesel unit goes above the nominal voltage, the reactive power of that generator becomes negative, and the generator is operated in an under-excited mode. In this case, the generator's reactive power demand is supplied by the rest of generators, and accordingly, the rating of the other generators must be increased. To avoid such scenarios, the under-excited behaviour of diesel generators is excluded.

$$\sqrt{{P_{dr,t,s}}^2 + {Q_{dr,t,s}}^2} \leq x_{b,dr} S_{dr},\ \forall b,\ dr,\ t,\ s \tag{4.19}$$

$$x_{b,dr} P_{dr}^{\min} \leq P_{dr,t,s} \leq x_{b,dr} P_{dr}^{\max},\ \forall b,\ dr,\ t,\ s \tag{4.20}$$

$$0 \leq Q_{dr,t,s} \leq x_{b,dr} Q_{dr}^{\max},\ \forall b,\ dr,\ t,\ s \tag{4.21}$$

$$Q_{cb,t,s} \leq x_{b,cr} S_{cr},\ \forall b,\ cr,\ t,\ s \tag{4.22}$$

$$I_{bk,t,s} \leq I_{bk}^{\max},\ \forall bk,\ t,\ s \tag{4.23}$$

$$V^{\min} \leq V_{t,b,s} \leq V^{\max},\ \forall b,\ t,\ s \tag{4.24}$$

$$\sum_b P_{b,s^M}^W \leq K^P \sum_b P_{b,s^M}^D \tag{4.25}$$

where P_{dr}^{max} and P_{dr}^{min} are the maximum and minimum active power limits of diesel generator dr, respectively; Q_{dr}^{max} is the maximum reactive power limit of diesel generator dr; V^{max} and V^{min} are the permissible bus maximum and minimum voltages, respectively; I_{bk} and I_{bk}^{max} are the current and the rated current of feeder bk, respectively; K^P is the allowed penetration for renewable DGs; $b \in \mathcal{S}^B$, $dr \in \mathcal{S}^{DR}$, $s \in \mathcal{S}^S$.

It is worth noting that the above-mentioned negative reactive power, which might be supplied by some of the generators, has the same reason as that of reactive-power-sharing-error, referred to in Part 1 of this subsection. They are due to the difference in generators'

feeder impedances. Because the generators' terminal voltage in (4.10) is not a global parameter and differs for different generators, the network-demanded reactive power is not shared accurately among generators, and in specific situations, some generators might supply negative reactive powers. Given that an isolated microgrid is operated based on droop characteristics, the operational consequences of their application must be considered in the planning, which as explained, requires a suitable model for power flow, and an additional constraint prohibiting under-excited behaviour of diesel generators.

4.3.2.3 Reliability

Algorithm 1 The LOLE Calculation

Start $\Pr_{fail} = 0$
for all $s_c \in \mathcal{S}^C$ **do**
    Read $island_1$ and $island_2$
    for all $s_g \in \mathcal{S}^G$ **do**
        for all $s_l \in \mathcal{S}^L$ **do**
            Calculate $\Pr_{c,g,l} = \Pr_c \Pr_g \Pr_l$
            for all $island \in \{island_1, island_2\}$ **do**
                if $island$ is not successful **then**
                    Calculate $\Pr_{fail} = \Pr_{fail} + \Pr_{c,g,l}$
                end if
            end for
        end for
    end for
end for
Calculate $LOLE = 8760 \Pr_{fail}$
/* s_g, s_l, and s_c are the indices for generation, load, and configuration states.
/* $\mathcal{S}^G$, $\mathcal{S}^L$, and $\mathcal{S}^C$ are the sets of system generation, load, and configuration states.
/* $\Pr_s$ is the probability of state s.

The North American Electric Reliability Corporation (NERC) standards mandate power systems to meet the $N-1$ security constraint, i.e., the system must continue its normal operation after any single element failure [115]. After a fault occurrence on any distribution line of an isolated microgrid and the fault removal, two separate islands are built. Depending on the fault location, the size of the islands can be significant, in which case under the NERC recommendations, neither can be ignored and both must operate normally. Compared to ADNs, building successful islands in the case of isolated microgrids

is more important, given that isolated microgrids are located in the off-grid regions with minimal access to other facilities.

On the other hand, the renewable DGs such as wind turbines and photovoltaic panels are categorized under the grid-feeding DGs, meaning that they cannot provide voltage and frequency support for the system [1]. These renewable DGs are connected to power systems through voltage-source-converters operated under the current-controlled mode to harvest their maximum available power, and accordingly, they are furnished with neither voltage control capability nor droop characteristics [2]. Therefore, although satisfying the supply adequacy constraint, an island comprising only renewable DGs such as wind turbines is doomed to failure. To avoid this failure, voltage controlled DGs should be distributed throughout an isolated microgrid to satisfy the reliability constraint developed in this subsection.

In this work, the reliability constraint is evaluated based on $LOLE$ derived for a composite generation-load-network model that takes into account the stochastic behaviour of the wind turbines and loads as well as the failure possibility of diesel generators, wind turbines, and distribution lines. First, all possible configurations caused by any distribution line fault removal are generated. Each configuration comprises two islands. An island is considered successful if, in addition to supply adequacy, i.e., meeting its active and reactive power demands, it has a voltage-controlled DG, which here is a diesel generator. Then, for all states of the generation and load as well as all configurations caused by the fault removals, $LOLE$ is calculated considering the states' corresponding probabilities as described by Algorithm 1. The obtained $LOLE$ should be less than its predefined upper limit, $LOLE^U$ as

$$LOLE \leq LOLE^U \tag{4.26}$$

where $LOLE^U$ is the upper limit for $LOLE$.

The above-mentioned supply adequacy is checked through the following conditions:

$$\sum_{b \in \mathcal{S}^{IB}} \sum_{dr \in \mathcal{S}^{DB}} x_{b,dr} S_{dr} \geq S^{LD,I}_{t,s^R} + S^{Loss,I}_{t,s^R} \quad \forall t, s^R \tag{4.27}$$

$$\sum_{b \in \mathcal{S}^{IB}} \sum_{dr \in \mathcal{S}^{DB}} x_{b,dr} Q^{\max}_{dr} \geq Q^{LD,I}_{t,s^R} + Q^{Loss,I}_{t,s^R} \quad \forall t, s^R \tag{4.28}$$

where $S^{Loss,I}_{t,s^R}$ and $Q^{Loss,I}_{t,s^R}$ are the apparent and reactive power losses in the island, and are considered 5% of the island apparent- and reactive-power demands, respectively [116]; $S^{LD,I}_{b,t,s^R}$, $P^{LD,I}_{b,t,s^R}$ and $Q^{LD,I}_{t,s^R}$ are the apparent-, active- and reactive-power demands of the

island, and are given by

$$S^{LD,I}_{t,s^R} = \sqrt{\left(P^{LD,I}_{t,s^R}\right)^2 + \left(Q^{LD,I}_{t,s^R}\right)^2} \tag{4.29}$$

$$P^{LD,I}_{t,s^R} = \sum_{b \in \mathcal{S}^{IB}} P^{L}_{b,t,s^R} - \sum_{b \in \mathcal{S}^{IB}} P^{W}_{b,t,s^R} \tag{4.30}$$

$$Q^{LD,I}_{t,s^R} = \sum_{b \in \mathcal{S}^{IB}} Q^{L}_{b,t,s^R} - \sum_{b \in \mathcal{S}^{IB}} Q^{C}_{b,t,s^R} \tag{4.31}$$

4.3.2.4 Voltage Distortion

The proliferation of nonlinear loads in distribution systems results in voltage-harmonic-distortion, one of the most significant power quality problems. Moreover, shunt capacitors are distributed throughout the distribution system as the source of reactive power or in the DGs' output filters. The presence of capacitors may lead to quasi-resonance [59], in which a harmonic frequency is near to the resonant frequency of the impedance network, and accordingly, aggregates the voltage distortion. Since the voltage distortion is affected by the size and location of DGs and CBs, harmonic analysis and voltage-distortion constraints should be embedded in the planning. As the harmonic analysis, in this chapter, a harmonic power flow algorithm suitable for the planning of isolated microgrids is developed, and is elaborated on in Section 4.4. As the voltage-distortion constraints, the upper limits of voltage total-harmonic-distortion (THD^V) and individual-harmonic-distortion (IH^V) are considered, as offered by the international standards in [98] and [117]. These constraints are checked at all microgrid buses and formulated as

$$THD^{V}_{b,t,s} \leq THD^{V,U}, \forall b, t, s \tag{4.32}$$

$$IH^{V}_{b,t,s} \leq IH^{V,U}, \forall b, t, s \tag{4.33}$$

where $THD^{V}_{b,t,s}$ and $IH^{V}_{b,t,s}$ are the THD^V and IH^V of bus b, at time t for state s; $THD^{V,U}$ are $IH^{V,U}$ the upper limits for voltage THD and IH, respectively; $b \in \mathcal{S}^B$ and $s \in \mathcal{S}^S$.

4.3.2.5 Binary Variables

The following constraints are considered for binary variables. Specifically, (4.35)-(4.37) are included to ensure only one member of each set can be installed at each candidate bus.

$$x_{db,dr},\ \ x_{wb,wr},\ \ x_{cb,cr},\ \ y_{cb,cr,s} \in \{0, 1\} \tag{4.34}$$

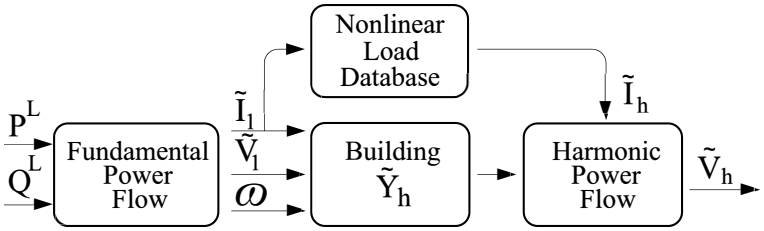

Figure 4.1: Harmonic power flow for isolated microgrids.

$$\sum_{dr \in \mathcal{S}^{DR}} x_{db,dr} \leq 1, \quad \forall\, db \in \mathcal{S}^{DB} \tag{4.35}$$

$$\sum_{wr \in \mathcal{S}^{WR}} x_{wb,wr} \leq 1, \quad \forall\, wb \in \mathcal{S}^{WB} \tag{4.36}$$

$$\sum_{cr \in \mathcal{S}^{CR}} x_{cb,cr} \leq 1, \quad \forall\, cb \in \mathcal{S}^{CB} \tag{4.37}$$

4.4 Harmonic Power Flow

In this section, a new harmonic power flow algorithm suitable for planning studies of isolated microgrids is developed. As shown in Figure 4.1, the fundamental power flow introduced in Subsection 4.3.2 provides the inputs for harmonic analysis, and accordingly, takes into account the fact that isolated microgrids are formed based on droop-based DGs and there is no slack bus. The fundamental power flow takes the vectors of load active and reactive powers, $\mathbf{P^L}$ and $\mathbf{Q^L}$, respectively, as the inputs, and generates the vectors of fundamental voltage and current phasors, i.e., $\tilde{\mathbf{V}}_\mathbf{1}$ and $\tilde{\mathbf{I}}_\mathbf{1}$, respectively, as well as the system frequency ω. The harmonic analysis includes the following:

1. The nonlinear loads' harmonic spectrum is updated based on their fundamental current magnitudes and phase angles. Representing the magnitude and phase angle of the h^{th} harmonic order obtained from the nonlinear loads' database by $I_{h,spec}$ and $\theta_{h,spec}$, respectively, one can write [61]:

$$\theta_h = \theta_{h,spec} + h\,(\theta_1 - \theta_{1,spec}) \tag{4.38}$$

$$I_h = I_1 \frac{I_{h,spec}}{I_{1,spec}} \tag{4.39}$$

where I_1 and θ_1 are the magnitude and phase angle of the fundamental current phasor, $\tilde{I}_1$. The vector of harmonic current phasor, $\tilde{\mathbf{I}}_\mathbf{h}$, is constructed using the updated spectrum of nonlinear loads.

2. The harmonic bus admittance matrix at different harmonic orders, $\tilde{\mathbf{Y}}_\mathbf{h}$ is generated using:

   - The dispatchable DGs' and distribution lines' admittances.
   - The CB's shunt admittances, as

   $$\tilde{Y}_{b,h} = jh\omega S_{cb,b} \tag{4.40}$$

   - An equivalent harmonic admittance of each linear loads, as given by (4.41) and (4.42).

   $$\tilde{Y}_{b,1} = \frac{P_b^L - jQ_b^L}{V_{b,1}^2} \tag{4.41}$$

   $$\tilde{Y}_{b,h} = \left(\mathrm{Re}(\tilde{Y}_{b,1}^{-1}) + jh\omega \times \mathrm{Im}(\tilde{Y}_{b,1}^{-1})\right)^{-1} \tag{4.42}$$

   where Re and Im operators return the real and imaginary parts, respectively; and $V_{b,1}$ is the voltage magnitude of bus b obtained from the fundamental power flow.
   - The Norton harmonic admittance of renewable DGs at each harmonic frequency, whose derivation is explained in Section 4.5.

   Of the above mentioned elements, except the distribution lines that are in series connection between two buses, the rest of the elements are shunt ones connecting one bus to the reference bus. The harmonic bus admittance matrix is constructed based on shunt and series admittances in its diagonal terms and only series admittances in its off-diagonal terms.

3. The microgrid bus harmonic voltages are acquired by

   $$\tilde{\mathbf{V}}_\mathbf{h} = \tilde{\mathbf{Y}}_\mathbf{h}^{-\mathbf{1}}\tilde{\mathbf{I}}_\mathbf{h} \tag{4.43}$$

4.5 Renewable DGs in Harmonic Power Flow

In this section, the derivation procedure for renewable DGs' output admittances at harmonic frequencies is explained, which is based on the works performed in [59], [118],

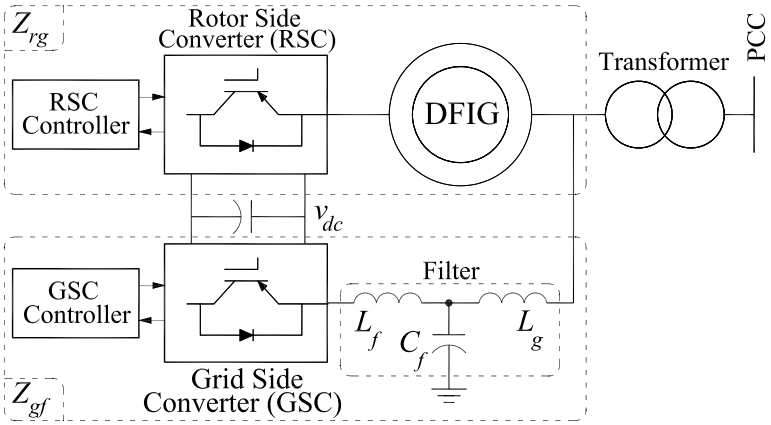

Figure 4.2: DFIG configuration diagram.

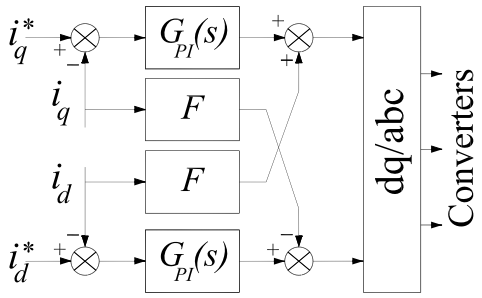

Figure 4.3: DFIG inner current loops.

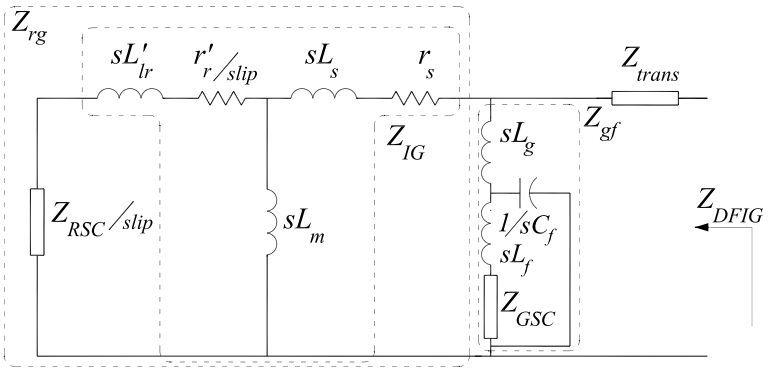

Figure 4.4: DFIG's impedance equivalent.

and [119]. Generally speaking, the switching frequencies of renewable DGs' voltage source converters (VSC) are high, so that these DGs do not generate low order harmonics [69]. This assumption is the basis of the harmonic analysis applied for planning in [56] and [57]; however, as shown in [59] and [118], the mutual interaction among the DGs' output filters, DGs' control systems and the distribution system might lead to resonance or quasi-resonance. Therefore, the harmonic model of such DGs must be embedded in the harmonic analysis. To do so, the Norton admittance of renewable DGs, considering their control systems and output filters, are obtained and added to the harmonic bus admittance matrix. In this chapter, the Norton admittance of type III wind turbines, i.e., doubly fed induction generators (DFIGs) are acquired. A similar procedure can be applied to include the harmonic models of other renewable DGs in the planning harmonic analysis.

The configuration diagram of a DFIG is shown in Figure 4.2. The DFIG's wound rotor is fed by the rotor-side converter (RSC) that is controlled to deliver the required active and reactive powers from the DFIG's stator. The grid-side converter is responsible to keep the dc-link voltage, v_{dc}, at its rated value. The LCL filter at the output of GSC is applied to suppress the switching frequency harmonics. The transformer is dedicated to providing the required voltage level and preventing the flow of inrush currents once the DFIG is connected to the grid. These elements are included in the DFIG's impedance, which according to Figure 4.2, consists of two parallel paths. The first path, Z_{rg}, comprises stator, rotor and the rotor-side converter. The second path, Z_{gf}, includes the filter and the grid-side converter.

The converters' impedances are affected by their controllers. Both DFIG's converters are controlled through the cascaded loops. The inner loops of both converters consist of current controllers, and their outer loops include power and voltage ones for RSC and

GSC, respectively. Because the bandwidths of the power and voltage loops are far below the harmonics of interest, these loops can be neglected in the impedance model of the converters [118]. The converters' inner-current loops are shown in Figure 4.3. As can be seen, they are implemented in the dq domain [120], using proportional-integral (PI) controllers along with feed-forward controllers. The following should be considered for RSC's and GSC's impedances:

- They are acquired using the Norton equivalent. The Norton equivalents of GSC and RSC current loops are initially obtained in the dq domain, and once shifted by $j\omega$, are transferred to the space-phasor domain [121].
- They are similar, and given by (4.44) in the space-phasor domain.

$$Z_{GSC} = Z_{RSC} = G_{PI}\left(s - j\omega\right) - jF \tag{4.44}$$

  where G_{PI} is the transfer function of the PI controller, and F is the feed-forward gain.

- The GSC's impedance is equal in the space phasor and Laplace domains; however, RSC's impedance in the Laplace domain is obtained by dividing the one in the space phasor domain by the rotor slip in the Laplace domain, which is defined by (4.45).

$$slip = \frac{s - j\omega_r}{s} \tag{4.45}$$

  where ω_r is the rotor speed.

Having the converters' impedances, and noting the already-described impedance paths, one can construct the DFIG's impedance equivalent as show in Figure 4.4, and use it to obtain the DFIG's impedance in the Laplace domain, $Z_{DFIG}\left(s\right)$. Given $Z_{DFIG}\left(s\right)$, one can substitute $jh\omega$ for s to acquire the DFIG's harmonic impedance at the h^{th} order harmonic. Then, the harmonic admittance of a bus with a DFIG can be written as

$$\tilde{Y}_{b,h} = \frac{1}{Z_{DFIG}\left(jh\omega\right)} \tag{4.46}$$

Obtaining the DFIG's impedance, it is instructive to look at a DFIG behavior at harmonic frequencies. Figure 4.5 shows the bode diagram of the output impedance of a 7.5 kW DFIG, which its parameters are given in [122]. As can be seen, at different harmonic orders, the DFIG shows different behaviours including inductive and capacitive ones. For

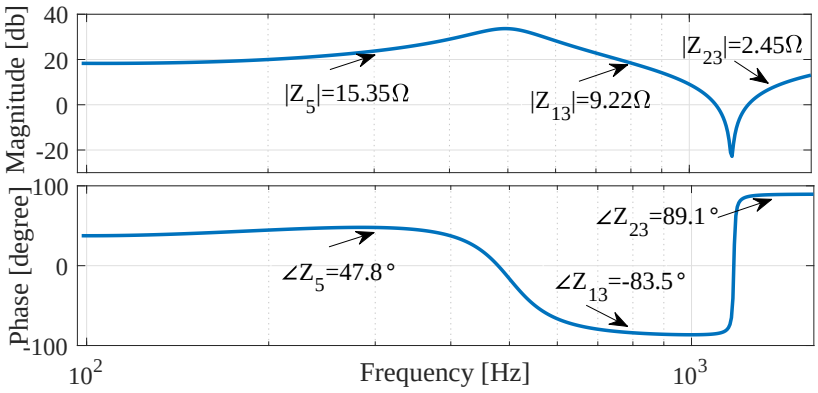

Figure 4.5: DFIG Output Impedance.

example, at the 23^{th} harmonic order, the phase angle is almost 90°, and accordingly, the DFIG shows an inductive behaviour. However, at the 13^{th} harmonic order, the phase angle is close to $-90°$, which represents a capacitor. It is worth noting that the magnitude of the DFIG's harmonic impedance are not large values, and thus, a DFIG can introduce a parallel inductive or capacitive branch to the network that must be considered in the harmonic analysis.

4.6 Uncertainty Modelling

This section describes the procedure for modelling the uncertainties associated with wind-power generation and load. The procedure is based on using historical data, and finding a suitable probability density function (PDF) for each source of uncertainty. Each PDF is then discretized by dividing its random variable (the uncertainty) into a number of segments, considering the trade-off between the accuracy and complexity of the planning problem. For each segment of a random variable, one state is assigned, whose value is given by the midpoint of that segment, and its probability is obtained using:

$$\Pr\left(x_a \leq x \leq x_b\right) = \int_{x_a}^{x_b} f_X\left(x\right) \tag{4.47}$$

where X is the random variable, x_a and x_b are the segment's bounds, and $f_X(x)$ is the PDF. Eventually, the combined wind-power generation and load model, which includes all possible operating conditions, is constructed by convolving different wind generation and

load states. Denoting wind-power generation and load states by s_w and s_l, respectively, a combined wind-power generation and load state can be considered as $s = (s_w, s_l)$, whose probability is equal to $\Pr_s = \Pr_{s_w} \times \Pr_{s_l}$.

In this study, five successive years of wind-speed data have been collected. Several PDFs including Weibull, Normal and Gamma were evaluated. Using a goodness-of-fit test [123], Weibull PDF has been selected to model the wind-speed uncertainty. The data were then categorized seasonally, and four PDFs, each representing a season, were obtained. On the other hand, the output power of a wind turbine is a function of the wind speed [45]. Combining the wind power function and the PDFs of wind speed, one can determine the states of wind-power generation.

Table 4.1: Load Stochastic Model

	Probability of Load States			
Load States	Winter	Spring	Summer	Fall
0.3388	0.2075	0.4887	0.2751	0.4754
0.6694	0.5574	0.4633	0.5469	0.4733
1.0000	0.2138	0.0219	0.1538	0.0255

Table 4.2: Wind Stochastic Model

	Probability of Wind States			
Wind States	Winter	Spring	Summer	Fall
0.0000	0.2503	0.1888	0.1561	0.2277
0.6500	0.3547	0.3878	0.5093	0.4073
1.0000	0.3950	0.4234	0.3346	0.3650

The historical data can also be used to accurately determine the load PDF. In this chapter, the load is assumed to follow the pattern of IEEE reliability test system (RTS) [124], which is a common practice in the literature [125]. The RTS provides hourly loads as the percentage of the daily peak-load for the four seasons where each season is represented by two days, a weekday and a weekend. The weekly peak-load is also described in terms of annual peak load, and accordingly, the yearly required data can be constructed. By following the same procedure as used for the wind-speed data, Normal PDF has been selected to model the load uncertainty.

Following the explained procedure, in this chapter, each of wind and load stochastic models are constructed in three states for each season, as illustrated in Tables 4.1 and 4.2, respectively. It is worth nothing that the proposed optimization problem has no limitation in terms of the number of wind and load states as well as the representative days that are considered in the development of the probabilistic model.

4.7 Solution procedure

In the next two sub-sections, the solution procedure for the proposed planning problem is elaborated as the main problem and a sub-problem.

4.7.1 Optimization Main Problem

The MINLP problem described in Section 4.3 is solved using genetic algorithm (GA). The effectiveness of GA in solving complicated optimization problems in the planning of power systems has already been proven in a verity of applications, e.g. in [126], [53], and [127]. The chromosome structure considered for GA is illustrated in Figure 4.6. As can be seen, the chromosome comprises four vectors. The first three vectors are assigned to the sizes and locations of diesel generators (DIGs), wind turbines (WTs) and capacitor banks (CBs), i.e., one vector for each type, where each vector's length is equal to the number of candidate buses. A zero value in each type's vector means not to install that type at the corresponding candidate bus. The fourth vector describes the switching status of capacitor banks and is made of several sub-vectors. Each sub-vector has the same length as the first three vectors and the number of sub-vectors is equal to the number of stochastic-model's load states. These sub-vectors eventually determine that a capacitor bank is fixed or switched as follows. A capacitor bank with values of one at all load states is a fixed capacitor bank, and otherwise, the capacitor bank is a switched one. The generated chromosomes are subsequently passed to the sum-problem.

For the sake of simplicity, in this chapter, only one capacitor unit has been considered for the switched-type CBs, as in [44] and [48], i.e., a capacitor bank is either in service, or is switched off. However, the chromosome structure proposed in Figure 4.6 can be simply revised to accommodate more capacitor units in the optimization. For this purpose, the fourth vector in the chromosome can be extended for the number of load states times the number of capacitor units. By doing so, for each CB, the optimization determines the units that should be in service at a load level.

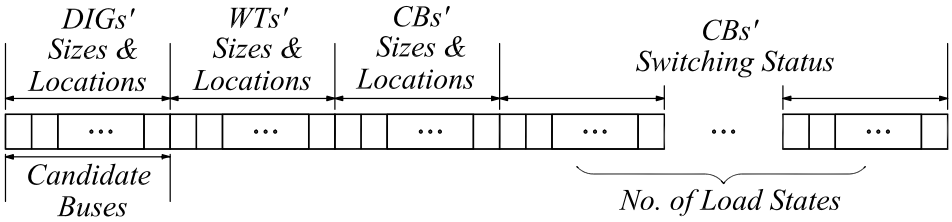

Figure 4.6: Chromosome structure.

4.7.2 Optimization Sub-Problem

The power flow constraints (4.7)–(4.18) are treated as an optimization sub-problem that minimizes the l^2-norm of power-flow-mismatch equations. To this aim, a nonlinear least-squares minimization is written as

$$\min_{\mathcal{X}^{PF}} \left\| \mathbf{F}(\mathcal{X}^{PF}) \right\|_2 \tag{4.48}$$

where $\mathbf{F}$ represents power mismatch equations for all buses that are extracted from (4.7) and (4.8); $\mathcal{X}^{\mathbf{PF}}$ is a vector comprising magnitudes and angles of bus-voltages as well as the network frequency. This optimization sub-problem is solved using a Newton-Trust region method [93]. The power flow solution is sent back to the main problem.

4.8 Case Studies and Discussion

Several studies are carried out in this section using the PG&E 69-bus system [Figure 4.7] to demonstrate the effectiveness of the proposed planning platform. The system line and load-demand data can be found in [128]. A planning horizon of 20 years is assumed. The annual interest, discount, and escalation rates are considered to be 7%, 5%, and 2%, respectively. The DGs' and CBs' different costs are those used in [48]. The lines' failure rate and repair time are taken as 0.12 f/km and 8 hr, respectively, and the reliability index limit, i.e., $LOLE^U$ is equal to 450 $hr/year$. For droop charateristics, the permissible frequency and voltage drops are equal to 1% and 5%, respectively. The harmonic spectrum of nonlinear loads [Figure 4.7] has been considered in accordance with the report of IEEE task force on harmonic modelling and simulations [129]. However, in order to be consistent with the harmonic upper limits as given by IEEE Std. 519 [98], the magnitudes of the harmonic spectrum are changed to adhere the standard, as illustrated in Table B.1 of Appendix B. The parameters of DFIG-based wind turbine applied for the harmonic analysis are also

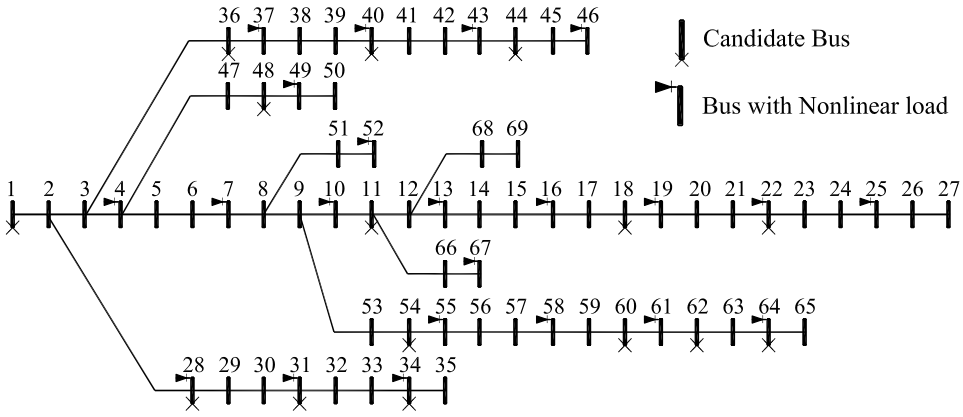

Figure 4.7: The test system (PG&E 69-bus).

given in Table B.2 of Appendix B. The harmonic analysis considers all odd harmonics up to the 37^{th} order. In what follows, three case studies are presented in which the first two studies only rely on the solution of the optimization sub-problem and the third one solves the whole problem.

4.8.1 Impact of Power Flow Algorithm and Introduced Constraint

The first case study reveals the significance of applying a power flow algorithm that takes into account the features of isolated microgrids, and the additional constraint introduced in Subsection 4.3.2. Two scenarios are studied, each based on three 5MVA diesel generators installed at a set of three buses.

Scenario 1 considers buses 1, 13, and 22. Figure 4.8 shows the voltage profile at the system peak load using the power flow algorithm suitable for isolated microgrids. The reactive powers delivered by the three generators are 3.202, 0.502, and -0.925 MVAr, respectively. The significant reactive power demanded by the generator of bus 22 is because the voltage of this bus has become more than 1 p.u. [Figure 4.8] while V^{nom} in (4.16) was 1 p.u. Several important points that can be seen are as follows. 1) The above-mentioned reactive power demand must be supplied by the two other generators, and accordingly, the system generation capacity is wasted. 2) The over-voltage is the direct consequence of applying the droop characteristics, and would not be observed if a conventional power flow were employed. The conventional power flow treats the DG buses as a PV one in which

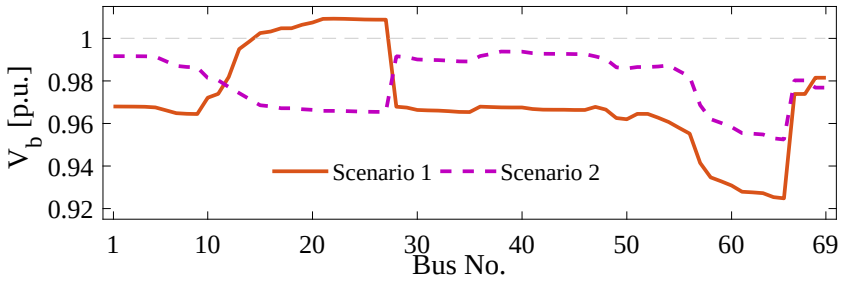

Figure 4.8: Impact of power flow algorithm and introduced constraint.

the bus voltage is assumed constant; however, in microgrids operated based on the droop characteristics, a dispatchable DG bus experiences a variable voltage that is determined by the load level and the slope of voltage-reactive power droop characteristic. 3) As long as the DGs are operated based on the droop characteristics, such consequences can exist, which must be considered in the planning stage. 4) One should note that the above issue happened without the presence of any capacitors, which their presence increases the chance of facing the over-voltage and reactive power demand by dispatchable DGs.

As for Scenario 2, the diesel generators are installed at buses 1, 38, and 54. The corresponding voltage profile at the system peak load has been shown in the same figure. The reactive powers delivered by the generators are 0.836, 0.619, and 1.270 MVAr, respectively. As can be seen, the above-mentioned issue of reactive power demand by dispatchable DGs has not been occurred. Moreover, it is clear that an appropriate distribution of the DGs can lead to a significant reduction in the reactive power demand, and consequently, in the system generation capacity.

4.8.2 Impact of DFIG Modelling in Harmonic Analysis

The second case study is conducted to show the importance of using the proposed model for renewable DGs in the harmonic analysis. For this study, the test network is supplied by a 5 MVA diesel generator installed at Bus 1 and a 0.5 MVA DFIG-based wind turbine at Bus 11. A 0.4 MVAr shunt capacitor bank is also connected to Bus 11. Figure 4.9 compares the network voltage THDs for the DFIG's simplified model of [56] and the one introduced in Section 4.5. As illustrated, a significant error as high of 2.8% can be expected. This voltage-THD discrepancy is attributed to the inductive/capacitive behaviour of the DFIG's harmonic impedances, and its mutual interaction with the shunt capacitor bank that leads to a quasi-resonance.

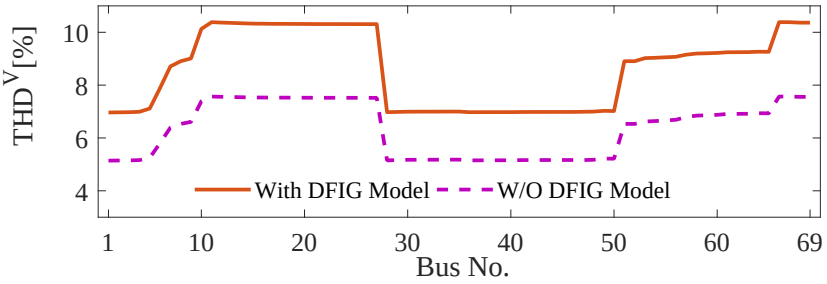

Figure 4.9: Impact of DFIG modelling in the harmonic analysis.

4.8.3 Impact of Voltage Distortion Constraint in Planning

The third case study evaluates the significance of including the voltage distortion constraint in the planning. To that aim, the optimization problem is solved in two scenarions, with and without the voltage distortion constraint. The candidate buses are shown in Figure 4.7.

First, the results for the scenario without the voltage distortion constraint are elaborated. The summary of the optimal solution is illustrated in the second column of Table 4.3. As can be seen, the optimization leads to four diesel generators that are distributed throughout the network to satisfy the reliability constraint along with two wind turbines and three capacitor banks. Two capacitor banks are of switched type, and according to the optimization results should be in service for the second and third load levels. The voltage profile and THD are shown in Figures 4.10(a) and 4.10(b), respectively. As observed, the voltage profile is within the limits; however, the voltage THD at many buses are far above the permissible level of 5% [98], e.g., the voltage THD at bus 35 is 7.9%.

In the second scenario, the inclusion of voltage distortion constraint solves the issue, and results in voltage THD of less than 4% at all buses. The third column of Table 4.3 illustrates the corresponding optimal solution. Compared to the case without the distortion constraint, the size of diesel generators and capacitor banks have been changed. Figures 4.11(a) and 4.11(b) show both voltage profile and voltage THD are now acceptable. Additionally, there is no much difference between the results of the voltage profile obtained here and those of the case without the voltage distortion constraint [Figure. 4.10(a)]. To quantify the cost of avoiding the voltage distortion, one can look at the annualized costs for both scenarios. While the annualized cost for the case without the voltage distortion constraint is \$2.609 million, this value for the case with voltage distortion constraint is \$2.622 million, which means by less than 0.5% increase in the cost, a severe distortion

Table 4.3: Optimal Solution with/without Voltage Distortion Constraint

	Without Voltage Distortion Constraint	With Voltage Distortion Constraint
Diesel Generator	1.3 MVA @ Bus 28, 0.6 MVA @ Bus 44, 1.2 MVA @ Bus 54, 1.1 MVA @ Bus 64	1.4 MVA @ Bus 28, 0.4 MVA @ Bus 44, 1.5 MVA @ Bus 54, 1 MVA @ Bus 64
Wind Turbine	0.3 MVA @ Bus 22, 0.5 MVA @ Bus 36	0.3 MVA @ Bus 22, 0.5 MVA @ Bus 36
Capacitor Bank	0.3 MVAr @ Bus 18: Fixed, 0.5 MVAr @ Bus 34: Switched, 0.5 MVAr @ Bus 48: Switched	0.3 MVAr @ Bus 18: Fixed, 0.4 MVAr @ Bus 34: Switched, 0.4 MVAr @ Bus 48: Switched
Maximum Voltage THD	7.9% @ Bus 35	3.8% @ Bus 35
Annualized Cost	\$2.609 million	\$2.622 million

problem can be avoided. It is worth noting that the above severe voltage distortion is appeared because of the presence of capacitors, and one might not see such a distortion if only allocating the DGs in a network without capacitors. This is especially the case when the nonlinear loads' harmonics are consistent with the international standards, as considered here.

4.9 Extending The Proposed Planning Method

4.9.1 Higher Numbers and Different Types of DGs

It is worth noting the proposed planning method does not have any limitation on the number and types of DGs. In fact, the number of DGs are decided within the optimization; however, the number of DGs is affected by the number of candidate buses. The proposed planning method can be used for any number of candidate buses, and the higher number of candidate buses only adds to the length of the chromosome described in Figure 4.6. On the other hand, although wind power generation has been focused here, the planning algorithm can be readily extended to comprise other types of renewable generators, including photovoltaics (PVs), once their stochastic models are generated, and added to generation-load state model by following the explanations of Section 4.6.

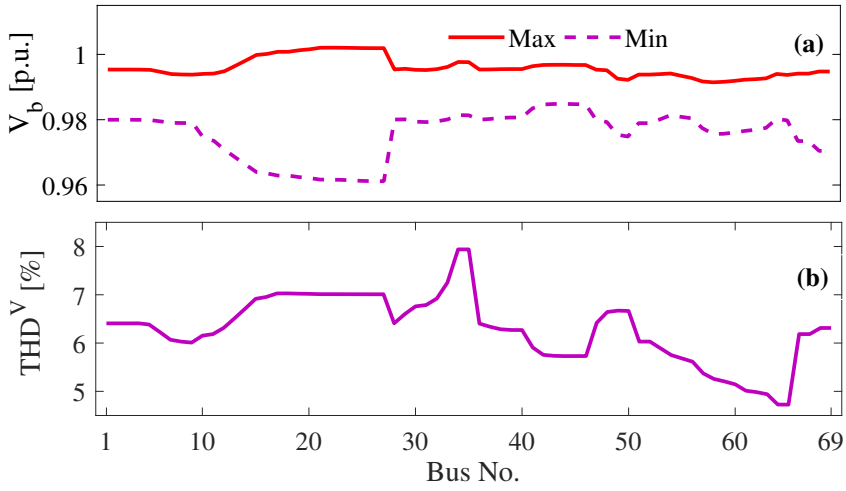

Figure 4.10: Planning without voltage distortion constraint.

4.9.2 Addition of Different Load Types

Different load types can be easily integrated into the planning method. They can be accommodated in the fundamental power flow algorithm by augmenting the model described by (4.7)-(4.18) with the following generic load equations [93]:

$$P_b^L = P_b^{L0} V_b{}^{\alpha} \left(1 + K_{pf} \left(\omega - \omega^{nom}\right)\right) \tag{4.49}$$

$$Q_b^L = Q_b^{L0} V_b{}^{\beta} \left(1 + K_{qf} \left(V_b - V^{nom}\right)\right) \tag{4.50}$$

where P_b^{L0} and Q_b^{L0} are the nominal values for the active and reactive powers of the load of bus b, respectively; α and β are the load active and reactive power exponents for dependence on voltage, respectively; K_{pf} and K_{qf} are the coefficients for active and reactive power dependence on frequency, respectively. With α and β equal to 0, 1, or 2, the model represents constant power, current, or constant impedance characteristics, respectively.

4.10 Conclusion

In this chapter a planning platform has been proposed to determine the optimal types (diesel generator or wind turbine), sizes, and locations of DGs and CBs in an isolated microgrids with nonlinear loads. In the proposed platform, the specific features of isolated

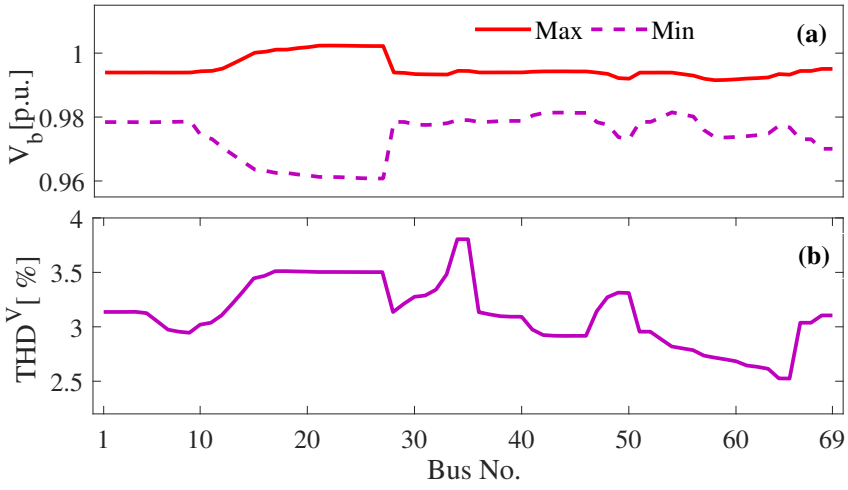

Figure 4.11: Planning with voltage distortion constraint.

microgrids, i.e., the lack of a slack bus and the droop-based behaviour of some DGs, have been taken into account for both fundamental power flow and harmonic power flow. To account for the possibility of resonance or quasi-resonance that can be caused by the wind turbines, a methodology has been proposed to incorporate them into the harmonic analysis. Eventually, given that a frequency and voltage provision cannot be provided by renewable DGs, a reliability-based technique has been proposed. This technique resulted in a better distribution of dispatchable DGs throughout the microgrid, and thus, allows building successful islands following a contingency.

Chapter 5

Harmonic Analysis of Three-Phase Diode Bridge Rectifiers Under Unbalanced and Distorted Supply

5.1 Introduction

Developing an effective harmonic power flow tool requires fast and accurate calculations of the harmonics generated by nonlinear elements. This chapter[1] presents a time-domain-based method for obtaining all steady-state characteristic and non-characteristic harmonics generated by three-phase diode bridge rectifiers, under unbalanced and distorted supply. The developed model is generic and able to address both continuous- and discontinuous-conduction modes with a single formulation. By introducing a virtual resistance on the rectifier's DC side, the model is extended to accommodate any DC-side filter. Further, a unique analytical Jacobian matrix is developed to guarantee a quadratic convergence for the iterative part of the proposed method. The effectiveness of the proposed method for harmonic analysis is confirmed through a comparative evaluation with time-domain simulations using PSCAD/EMTDC.

[1] A version of this chapter has been published: A. H. Yazdavar, M.A. Azzouz, E. F. El-Saadany, "Harmonic Analysis of Three-Phase Diode Bridge Rectifiers Under Unbalanced and Distorted Supply", *IEEE Trans. on Power Delivery.*

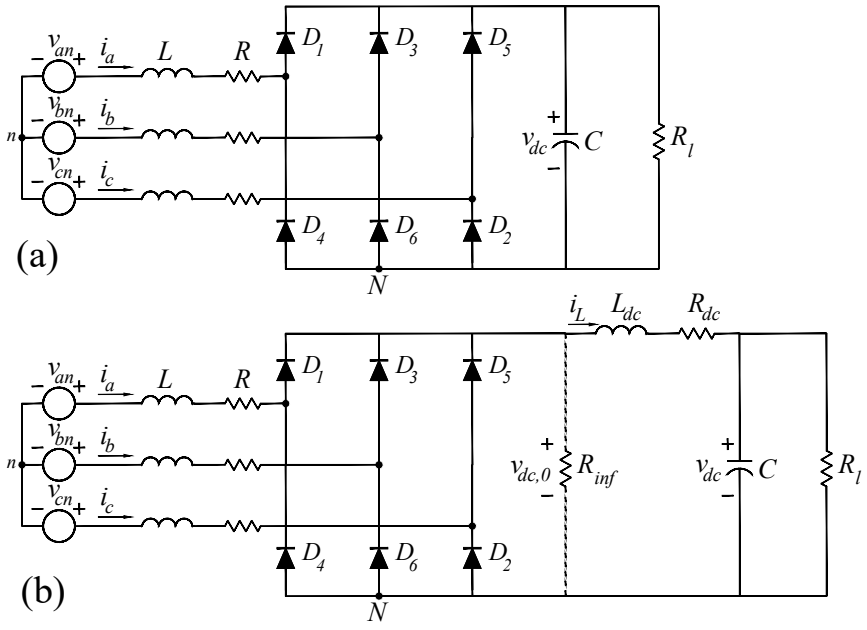

Figure 5.1: Rectifier circuit.

5.2 Contributions

The main contributions of this chapter are as follows:

- A state-space-based model is derived with which to obtain all steady-state characteristic and non-characteristic harmonics of three-phase diode bridge rectifiers, under distorted and unbalanced supply. The model is independent of the network's X/R ratio.
- An analytical Jacobian matrix is developed to accelerate convergence. In this development, the system model has been arranged so as to prohibit the appearance of any terms requiring the integration of a matrix exponential.
- The AC and DC sides of the rectifier are decoupled, through R_{inf}, allowing the model extension for any DC-side filter.

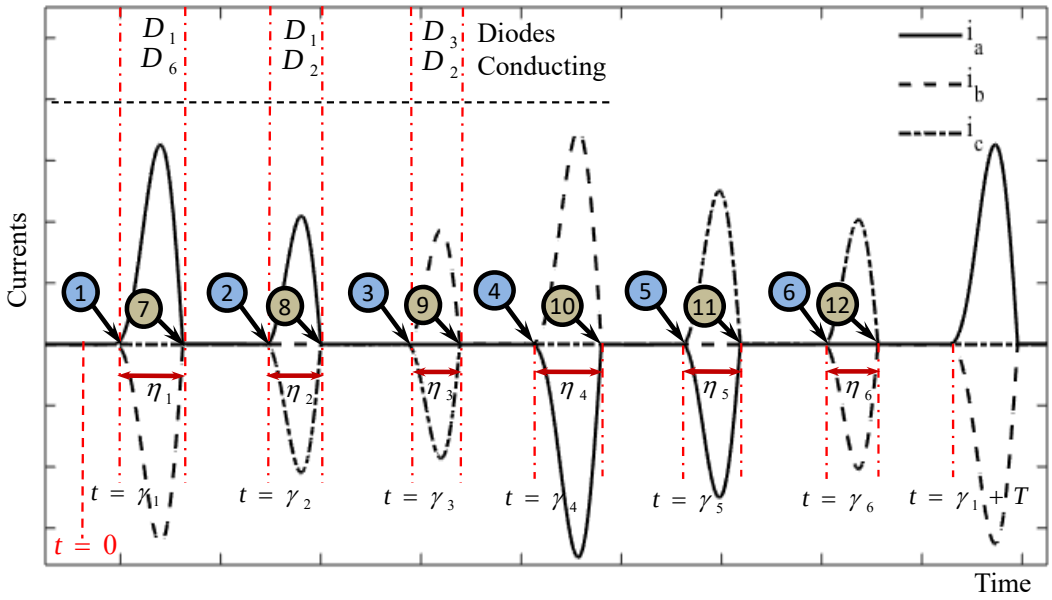

Figure 5.2: Discontinuous mode.

5.3 System Description

Figure 5.1 shows two three-phase diode bridge rectifier circuits with C and LC smoothing filters. The DC load is represented by a resistor, which might be an actual resistive load at the DC side, the inverter of a VSD, or a DC/DC converter. The target of harmonic analysis is to develop a model that gives the steady-state harmonics of the AC currents and DC voltage, once supplied by a distorted and unbalanced source. The developed model can be applied in harmonic power flow algorithms to improve the accuracy of existing methods, such as the ones proposed in [130] and [131], where the nonlinear loads are represented at each harmonic by a current source. At each iteration of a harmonic power flow algorithm, the information of the supply voltage harmonics in terms of magnitude and phase angles are known, and thus are regarded as the inputs in the developed model. The supply voltage can be considered as

$$\begin{cases} v_{an} = \sum\limits_{h} V_h \sin\left(|h|\,\omega t + \phi_h\right) \\ v_{bn} = \sum\limits_{h} V_h \sin\left(|h|\,\omega t + \phi_h - \frac{2\pi}{3} S_h\right) \\ v_{cn} = \sum\limits_{h} V_h \sin\left(|h|\,\omega t + \phi_h + \frac{2\pi}{3} S_h\right) \end{cases} \tag{5.1}$$

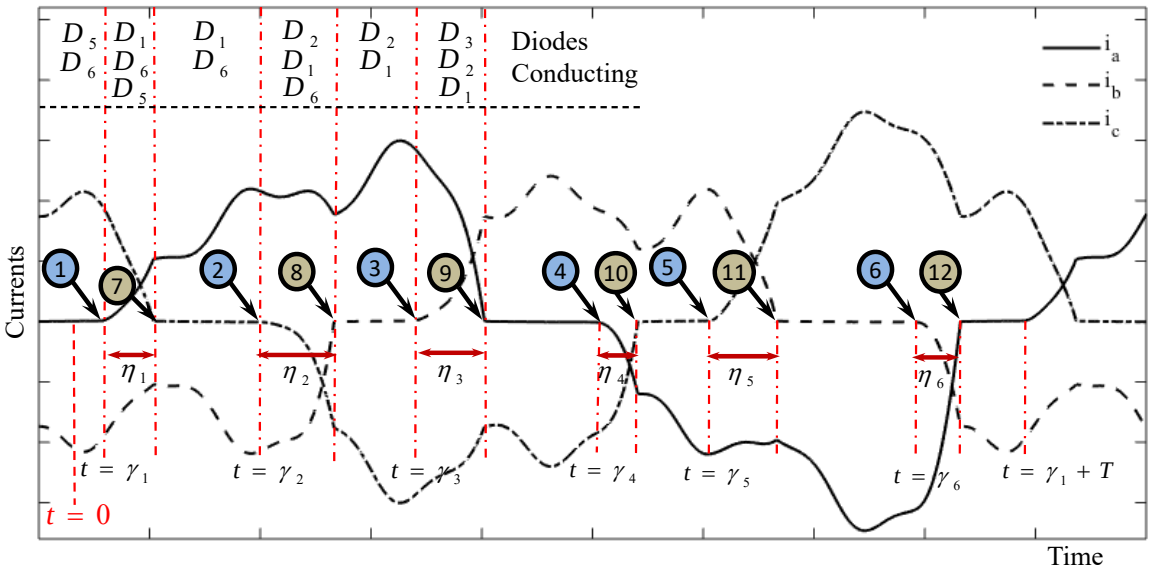

Figure 5.3: Continuous mode.

where h is the harmonic order; ω is the supply frequency; V_h and ϕ_h are the magnitude and phase angle of the h^{th} order harmonic, respectively; and S_h is given by

$$S_h = \begin{cases} +1 & h = 1, 4, 7, ... \\ -1 & h = -1, -2, -5, ... \end{cases} \tag{5.2}$$

The model formulation is initially derived for Figure 5.1(a) with the C filter, and then extended to accommodate the LC filter, i.e., displayed in Figure 5.1(b).

Figures 5.2 and 5.3 demonstrate the general trend of the three-phase currents (i_a, i_b, and i_c) in Figure 5.1, for the DCM and CCM, respectively. As can be seen, the supply voltage in (5.1) leads to different peaks and conduction angles for different phases. Also, the sixth-period symmetry, introduced by [77], no longer exists. Further, half-wave symmetry is not applicable, given that the model must consider the existence of even harmonics in the supply. Hence, the formulation is developed based on a complete period (T), which is considered here from $t = \gamma_1$ to $t = \gamma_1 + T$.

5.4 Calculating The Switching Instants

Obtaining the harmonic current source equivalent of a diode rectifier entails getting the switching instants, γ_i and $\gamma_i + \eta_i$, where $i \in \{1, 2, ..., 6\}$, as shown in Figures 5.2 and 5.3. The switching instants can be acquired using the boundary conditions of the phase voltages and currents; twelve switching instants need twelve boundary conditions. Such conditions are defined on the system model, which is developed in the state-space domain.

5.4.1 System in State-Space Domain

The switching instants divide each period into twelve time segments that are governed by six pairs of state-space equations, i.e.,

$$\dot{\mathbf{X}} = \mathbf{A_{on,i}}\mathbf{X} \qquad \gamma_i \leq t \leq \gamma_i + \eta_i \tag{5.3}$$

$$\dot{\mathbf{X}} = \mathbf{A_{off,i}}\mathbf{X} \qquad \gamma_i + \eta_i \leq t \leq \gamma_{i+1} \tag{5.4}$$

where $\mathbf{X}$ is the state-space vector; $\mathbf{A_{on,i}}$ and $\mathbf{A_{off,i}}$ are state transition matrices, which are detailed in Section 5.5; $i \in \{1, 2, ..., 6\}$; $\gamma_{6+1} = \gamma_1 + T$.

For the case of CCM, $\mathbf{A_{on,i}}$ matrices correspond to commutation intervals, in which three diodes conduct together. However, for DCM, these matrices give the system equation for conduction intervals in which two diodes close the current path between the supply and the DC side. On the other hand, $\mathbf{A_{off,i}}$ matrices are correlated to the conduction of two diodes for CCM, and no diode for DCM. Thus, for both CCM and DCM, the numbers of conducting diodes differ in the time segments described by (5.3) and (5.4).

Given that each diode allows current to pass through one phase of the supply and the corresponding AC-side inductor, different numbers of conducting diodes lead to different numbers of state variables, and accordingly different state-space vectors. Additionally, to build the system model, the state-space equations of different time segments must be combined. Doing so is simpler with the same state-space vectors. Otherwise, the basis for the state-space vectors must be changed at each switching instant [77]. To avoid the complexity of changing the bases, the diodes are modelled by a piecewise linear model through two different resistances, R_{on} and R_{off}, being on and off, respectively. While the former resistance is a very small value, the latter is taken to be significantly large. Large R_{off} causes a negligible current to pass through the non-conducting diode with no manipulation of the state-space vector containing the state variables.

The state-space vector includes circuit state variables and supply state variables, as $\mathbf{X} = \begin{bmatrix} \mathbf{X_{cir}}^{\mathbb{T}} & \mathbf{X_{sup}}^{\mathbb{T}} \end{bmatrix}^{\mathbb{T}}$. The circuit state variables are the currents at the AC side, and the voltage at the DC side, i.e., $\mathbf{X_{cir}} = \begin{bmatrix} i_a & i_b & i_c & v_{dc} \end{bmatrix}^{\mathbb{T}}$. The supply state variables are considered as follows. In the stationary $\alpha\beta$ domain, for each supply harmonic, one voltage component can be written in terms of the derivative of the other component. Thus, the harmonic voltage components are taken as state variables, i.e., $\mathbf{X_{sup}} = \begin{bmatrix} v_{\alpha,1} & v_{\beta,1} & \dots & v_{\alpha,h} & v_{\beta,h} & \dots \end{bmatrix}^{\mathbb{T}}$. The length of $\mathbf{X_{sup}}$ is $2n_h$, where n_h denotes the number of supply harmonics. In this chapter, ellipsis "..." in vectors and matrices stands for their extension for all harmonics.

5.4.2 Mismatch Equations

This subsection develops a single formulation for both CCM and DCM with which the mismatch equations governing the switching instants can be described. This formulation is based on obtaining the relation between the state variables at the first instant and the last instant of a period, i.e., $\mathbf{X}(\gamma_1)$ and $\mathbf{X}(\gamma_1+T)$, through two approaches.

In the first approach, the solutions of the state-space equations, (5.3) and (5.4), at different time segments within a period are combined. Each segment's differential equation gives the relation between the state variables at the last and first instants of a segment. Additionally, the state variables at the first instant of each segment equal the state variables at the last instant of the precedent segment. By combining the relations of different segments, the state variables at the end of the period, i.e., at $t = \gamma_1 + T$ are obtained as

$$\mathbf{X}(\gamma_1+T) = \mathbf{\Phi}\mathbf{X}(\gamma_1) \tag{5.5}$$

where $\mathbf{\Phi}$ is a square matrix of size $4 + 2n_h$, and is given by

$$\mathbf{\Phi} = \prod_{i=1}^{6} e^{\mathbf{A_{off,i}}(\gamma_{i+1}-\gamma_i-\eta_i)} e^{\mathbf{A_{on,i}}(\eta_i)} \tag{5.6}$$

The second approach uses the steady-state constraints based on the periodic nature of the state variables. Because the steady-state harmonics are aimed

$$\mathbf{X}(\gamma_1+T) = \mathbf{X}(\gamma_1) \tag{5.7}$$

From (5.5) and (5.7), one gets

$$(\mathbf{\Phi} - \mathbf{I})\,\mathbf{X}\,(\gamma_1) = \mathbf{0} \tag{5.8}$$

where $\mathbf{I}$ is the identity matrix of size $4 + 2n_h$.

Equation (5.8) is a homogeneous one. To obtain its non-trivial solution, $(\mathbf{\Phi} - \mathbf{I})$ and $\mathbf{X}\,(\gamma_1)$ are decomposed into their sub-matrices and sub-vectors, respectively, allowing (5.8) to be re-written as

$$\begin{bmatrix} \mathbf{D} & \mathbf{E} \\ \mathbf{F} & \mathbf{K} \end{bmatrix} \begin{bmatrix} \mathbf{X}_{\text{cir}}\,(\gamma_1) \\ \mathbf{X}_{\text{sup}}\,(\gamma_1) \end{bmatrix} = \begin{bmatrix} \mathbf{0} \\ \mathbf{0} \end{bmatrix} \tag{5.9}$$

where the size of the sub-matrices are as follows: for $\mathbf{D}$, 4×4; for $\mathbf{E}$, $4 \times 2n_h$; for $\mathbf{F}$, $2n_h \times 4$; and for $\mathbf{K}$, $2n_h \times 2n_h$.

From (5.9), $\mathbf{X_{cir}}\,(\gamma_1)$ is obtained as

$$\mathbf{X_{cir}}\,(\gamma_1) = -\mathbf{D}^{-1}\mathbf{E}\mathbf{X_{sup}}\,(\gamma_1) \tag{5.10}$$

According to (5.10), the circuit state variables can be acquired if the supply state variables at $t = \gamma_1$ are known. The in-quadrature nature of the supply voltage components in the stationary $\alpha\beta$ domain, described in the previous subsection, makes this possible. Therefore,

$$\dot{\mathbf{X}}_{\mathbf{sup}} = \mathbf{A}^{\mathbf{sup,sup}}\mathbf{X}_{\mathbf{sup}} \tag{5.11}$$

where $\mathbf{A}^{\mathbf{sup,sup}}$ is of size $2n_h \times 2n_h$, relates the supply state variables together, and is given by

$$\mathbf{A}^{\mathbf{sup,sup}} = diag\left(\begin{bmatrix} 0 & -\omega \\ \omega & 0 \end{bmatrix}, ..., \begin{bmatrix} 0 & -h\omega \\ h\omega & 0 \end{bmatrix}, ...\right) \tag{5.12}$$

Using (5.11), $\mathbf{X_{sup}}\,(\gamma_1)$ is written as

$$\mathbf{X_{sup}}\,(\gamma_1) = e^{\mathbf{A}^{\mathbf{sup,sup}}\gamma_1}\mathbf{X_{sup}}\,(0) \tag{5.13}$$

From (5.10) and (5.13), $\mathbf{X}\,(\gamma_1) = \begin{bmatrix} \mathbf{X_{cir}}\,(\gamma_1)^{\mathbb{T}} & \mathbf{X_{sup}}\,(\gamma_1)^{\mathbb{T}} \end{bmatrix}^{\mathbb{T}}$ is obtained. Having $\mathbf{X}\,(\gamma_1)$, the system state variables at the end of each segment, i.e., at $t = \gamma_i$ and $t = \gamma_i + \eta_i$, where $i \in \{1, 2, ..., 6\}$ are acquired using (6.12) and (5.15):

$$\mathbf{X}\,(\gamma_i + \eta_i) = e^{\mathbf{A}_{\mathbf{on,i}}(\eta_i)}\mathbf{X}\,(\gamma_i) \tag{5.14}$$

Table 5.1: Boundary Conditions on Voltages and Currents

Voltage Conditions				Current Conditions			
point		CCM	DCM	point		CCM	DCM
1	$t = \gamma_1$	$3v_{an} = v_{dc}$	$v_{ab} = v_{dc}$	7	$t = \gamma_1 + \eta_1$	$i_c = 0$	$i_a = 0$
2	$t = \gamma_2$	$-3v_{bn} = v_{dc}$	$v_{ac} = v_{dc}$	8	$t = \gamma_2 + \eta_2$	$i_b = 0$	$i_a = 0$
3	$t = \gamma_3$	$3v_{cn} = v_{dc}$	$v_{bc} = v_{dc}$	9	$t = \gamma_3 + \eta_3$	$i_a = 0$	$i_b = 0$
4	$t = \gamma_4$	$-3v_{an} = v_{dc}$	$v_{ba} = v_{dc}$	10	$t = \gamma_4 + \eta_4$	$i_c = 0$	$i_b = 0$
5	$t = \gamma_5$	$3v_{bn} = v_{dc}$	$v_{ca} = v_{dc}$	11	$t = \gamma_5 + \eta_5$	$i_b = 0$	$i_c = 0$
6	$t = \gamma_6$	$-3v_{cn} = v_{dc}$	$v_{cb} = v_{dc}$	12	$t = \gamma_6 + \eta_6$	$i_a = 0$	$i_c = 0$

$$\mathbf{X}(\gamma_{i+1}) = e^{\mathbf{A_{off,i}}(\gamma_{i+1}-\gamma_i-\eta_i)}\mathbf{X}(\gamma_i + \eta_i) \tag{5.15}$$

Given that the boundary conditions introduced in the next subsection can be described in terms of the state variables at the switching instants, the mismatch equations can be written as follows:

$$f_i = \mathbf{C_{f,i}}\mathbf{X}(\gamma_i) \tag{5.16}$$

$$g_i = \mathbf{C_{g,i}}\mathbf{X}(\gamma_i + \eta_i) \tag{5.17}$$

where $\mathbf{C_{f,i}}$ and $\mathbf{C_{g,i}}$ are row vectors and are given in Subsection 5.6.1.

Using the Newton method, the solution to a set of twelve equations described by (5.16) and (5.17) can be written as

$$\mathbf{\Delta^{(j+1)}} = \mathbf{\Delta^{(j)}} - \mathbf{J^{-1}}\mathbf{H_{fg}}\left(\mathbf{\Delta^{(j)}}\right) \tag{5.18}$$

where $\mathbf{\Delta}$ is a vector containing all η_i and γ_i angles, $\mathbf{J}$ is the Jacobian matrix given in Subsection 5.6.2, $\mathbf{H_{fg}}$ is a vector containing all mismatch equations, and j is the iteration number. The developed Jacobian matrix has the advantage of being similar for different rectifier operating modes and filter structures.

5.4.3 Boundary Conditions

The aforementioned twelve boundary conditions that are required for obtaining the switching instants, γ_i and $\gamma_i + \eta_i$ are basically the diodes' turn-on and turn-off conditions. The turn-on conditions are described in terms of the relation between the supply and DC-side

voltages, and the turn-off conditions are given by the AC side currents. Table 5.1 illustrates the boundary conditions for both CCM and DCM in accordance with Figures 5.2 and 5.3.

Points 1 to 6 in Table 5.1 correspond to voltage conditions that turn on the diodes. For the DCM, the diodes turn on once their corresponding supply line voltage becomes equal to the DC-side voltage, v_{dc}. For example, at $t = \gamma_1$, according to Figure 5.2, D_1 and D_6 start conduction, when $(v_{an} - v_{bn})$ is equal to v_{dc}. On the other hand, in order to have a diode start conduction in the CCM, the DC-side voltage should be three times that of the supply voltage associated with that diode. For example, at $t = \gamma_1$, according to Figure 5.3, D_1 is supposed to start conduction, and its associated voltage is v_{an}, it is necessary to have $v_{dc} = 3v_{an}$.

Eventually, for Points 7 to 12, the turn-off conditions for CCM and DCM are given based on zeroing of the AC-side currents in accordance with Figures 5.2 and 5.3.

5.5 State Space Model Details

The state transition matrices, $\mathbf{A_{on},}_i$ and $\mathbf{A_{off},}_i$ of (5.3) and (5.4), for both DCM and CCM can be formulated in the following generic forms

$$\mathbf{A_{on,i}} = \begin{bmatrix} \mathbf{A_{on,i}^{cir,cir}} & \mathbf{A_{on,i}^{cir,sup}} \\ \mathbf{0}_{2n_h \times 4} & \mathbf{A^{sup,sup}} \end{bmatrix} \tag{5.19}$$

$$\mathbf{A_{off,i}} = \begin{bmatrix} \mathbf{A_{off,i}^{cir,cir}} & \mathbf{A_{off,i}^{cir,sup}} \\ \mathbf{0}_{2n_h \times 4} & \mathbf{A^{sup,sup}} \end{bmatrix} \tag{5.20}$$

The sub-matrices of (5.19) and (5.20), for DCM and CCM are given in the Subsections 5.5.1 and 5.5.2, respectively.

5.5.1 Discontinuous Conduction Mode

According to Figure 5.2, for $\gamma_1 \leq t \leq \gamma_1 + \eta_1$, D_1 and D_6 are conducting. Figure 5.4 shows the current circulating path for this conduction interval. Applying KVL, modelling the conducting diodes by R_{on}, and noting $i_a = -i_b$ give the differential equations of phases a and b, as expressed by (5.21) and (5.22). To represent the negligible current of phase c, R_{off} is used instead of R_{on} in (5.23). The high value of R_{off} and the consequent negligible i_c allow us to select the rest of the terms in (5.23) to simplify building the state-space

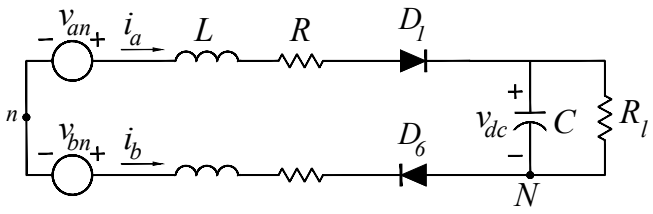

Figure 5.4: Rectifier circuit during a conduction interval.

equations. To do so, terms similar to those in phase-a equation are used. The equations for the circuit state variables are completed by adding the differential equation of the DC side, given by (5.24):

$$\frac{di_a}{dt} = -\frac{R+R_{on}}{L}i_a - \frac{1}{2L}v_{dc} + \frac{1}{2L}(v_{an} - v_{bn}) \tag{5.21}$$

$$\frac{di_b}{dt} = -\frac{R+R_{on}}{L}i_b + \frac{1}{2L}v_{dc} - \frac{1}{2L}(v_{an} - v_{bn}) \tag{5.22}$$

$$\frac{di_c}{dt} = -\frac{R+R_{off}}{L}i_c - \frac{1}{2L}v_{dc} + \frac{1}{2L}(v_{an} - v_{bn}) \tag{5.23}$$

$$\frac{dv_{dc}}{dt} = \frac{1}{C}i_a - \frac{1}{CR_l}v_{dc} \tag{5.24}$$

After $t = \gamma_1 + \eta_1$, the conducting diodes, i.e., D_1 and D_6, switch to the turn-off mode, which will be continued until $t = \gamma_2$. As the diodes turn off, the three-phase currents become zero, leaving just the DC side energized. In this case, the differential equations relevant to circuit state variables can be derived by replacing R_{on} with R_{off}, and are not re-written here to save space. Therefore, $\mathbf{A}^{\mathbf{cir,cir}}_{\mathbf{on,i}}$, $\mathbf{A}^{\mathbf{cir,cir}}_{\mathbf{off,i}}$, $\mathbf{A}^{\mathbf{cir,sup}}_{\mathbf{on,i}}$ and $\mathbf{A}^{\mathbf{cir,sup}}_{\mathbf{off,i}}$ for the first two segments of DCM, i.e., $i = 1$ become:

$$\mathbf{A}^{\mathbf{cir,cir}}_{\mathbf{on,1}} = \begin{bmatrix} -\frac{R+R_{on}}{L} & 0 & 0 & -\frac{1}{2L} \\ 0 & -\frac{R+R_{on}}{L} & 0 & \frac{1}{2L} \\ 0 & 0 & -\frac{R+R_{off}}{L} & -\frac{1}{2L} \\ \frac{1}{C} & 0 & 0 & -\frac{1}{CR_l} \end{bmatrix} \tag{5.25}$$

$$\mathbf{A}^{\mathbf{cir,cir}}_{\mathbf{off,1}} = \begin{bmatrix} -\frac{R+R_{off}}{L} & 0 & 0 & -\frac{1}{2L} \\ 0 & -\frac{R+R_{off}}{L} & 0 & \frac{1}{2L} \\ 0 & 0 & -\frac{R+R_{off}}{L} & -\frac{1}{2L} \\ \frac{1}{C} & 0 & 0 & -\frac{1}{CR_l} \end{bmatrix} \tag{5.26}$$

$$\mathbf{A}^{\mathbf{cir,sup}}_{\mathbf{on,1}} = \mathbf{A}^{\mathbf{cir,sup}}_{\mathbf{off,1}} = \frac{1}{2L}\mathbf{K}^{\mathbf{dc,1}}_{\mathbf{abc}}\mathbf{K}^{\mathbf{abc}}_{\alpha\beta}\mathbf{K}^{\alpha\beta}_{\mathbf{h}} \tag{5.27}$$

where $\mathbf{K}^{\mathbf{dc,1}}_{\mathbf{abc}}$ relates the last terms of (5.21)–(5.23) to the phase voltages, $\mathbf{K}^{\mathbf{abc}}_{\alpha\beta}$ is the inverse Clarke transformation matrix, and $\mathbf{K}^{\alpha\beta}_{\mathbf{h}}$ allows writing the voltages of $\alpha\beta$ domain in terms of their harmonic components. $\mathbf{K}^{\mathbf{dc,1}}_{\mathbf{abc}}$, $\mathbf{K}^{\mathbf{abc}}_{\alpha\beta}$, and $\mathbf{K}^{\alpha\beta}_{\mathbf{h}}$ are expressed by

$$\mathbf{K}^{\mathbf{dc,1}}_{\mathbf{abc}} = \begin{bmatrix} 1 & -1 & 1 & 0 \\ -1 & 1 & -1 & 0 \\ 0 & 0 & 0 & 0 \end{bmatrix}^{\mathbb{T}} \tag{5.28}$$

$$\mathbf{K}^{\mathbf{abc}}_{\alpha\beta} = \begin{bmatrix} 1 & -\frac{1}{2} & -\frac{1}{2} \\ 0 & \frac{\sqrt{3}}{2} & -\frac{\sqrt{3}}{2} \end{bmatrix}^{\mathbb{T}} \tag{5.29}$$

$$\mathbf{K}^{\alpha\beta}_{\mathbf{h}} = \begin{bmatrix} 1 & 0 & \dots & 1 & 0 & \dots \\ 0 & 1 & \dots & 0 & 1 & \dots \end{bmatrix}_{2\times 2n_h} \tag{5.30}$$

For the remaining time segments of DCM, $\mathbf{A}^{\mathbf{cir,cir}}_{\mathbf{on,i}}$, $\mathbf{A}^{\mathbf{cir,cir}}_{\mathbf{off,i}}$, $\mathbf{A}^{\mathbf{cir,sup}}_{\mathbf{on,i}}$, and $\mathbf{A}^{\mathbf{cir,sup}}_{\mathbf{off,i}}$ matrices can be developed based on the following observations on (5.21)–(5.24):

1. The state equations (5.21)–(5.23) have two R_{on}, corresponding to phases connected to the conducting diodes, and one R_{off}, for the non-conducting phase.
2. The conducting diodes determine the line voltage appearing in (5.21)–(5.23). Here, D_1 and D_6 conduction leads to $(v_{an} - v_{bn})$.
3. For the two conducting phases, the one connected to the upper diode (D_1) sends the current to the DC side, and the other one that is connected to the lower diode (D_6) receives the current from the DC side.
4. The sending-phase-state equation (phase a) has a negative sign for the v_{dc} multiplier, and a positive sign for the line voltage multiplier. Such multipliers have opposite signs for the receiving phase (phase b) state equation, and similar signs for the non-conducting phase (phase c) state equation.

Applying the above observations for the sequence of conducting diodes, shown in Figure 5.2 for a half-period, provides $\mathbf{A}^{\mathbf{cir,cir}}_{\mathbf{on,i}}$ matrices for the remaining conducting segments, which by replacing R_{on} by R_{off} gives the corresponding $\mathbf{A}^{\mathbf{cir,cir}}_{\mathbf{off,i}}$ matrices for the non-conducting segments. Lastly, to obtain the rest of $\mathbf{A}^{\mathbf{cir,sup}}_{\mathbf{on,i}}$ and $\mathbf{A}^{\mathbf{cir,sup}}_{\mathbf{off,i}}$ matrices, $\mathbf{K}^{\mathbf{dc}}_{\mathbf{abc,1}}$

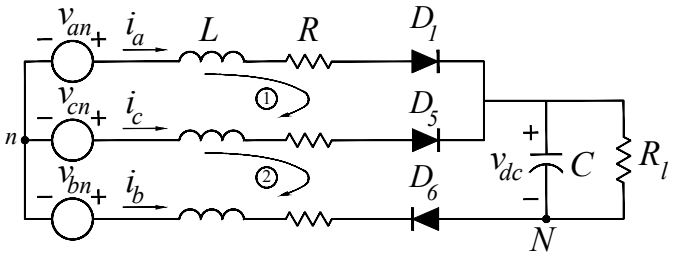

Figure 5.5: Rectifier circuit during a commutation interval.

in (5.27) should be replaced by $\mathbf{K}^{\mathbf{dc}}_{\mathbf{abc,i}}$, which is determined based on the second point of the above observations.

5.5.2 Continuous Conduction Mode

According to Figure 5-3, $\gamma_1 \leq t \leq \gamma_1 + \eta_1$ corresponds to a commutation interval, in which the three diodes D_1, D_5, and D_6 are conducting. By writing the KVL for loops 1 and 2 of Figure 5.5, and substituting for one phase current in terms of the other two phase currents (e.g., $i_c = -(i_a + i_b)$), (5.31)–(5.33) are given. Addition of the DC-side dynamic equation completes the circuit state-space equations for this commutation interval:

$$\frac{di_a}{dt} = -\frac{R+R_{on}}{L} i_a - \frac{1}{3L} v_{dc} + \frac{2v_{an} - (v_{bn} + v_{cn})}{3L} \tag{5.31}$$

$$\frac{di_b}{dt} = -\frac{R+R_{on}}{L} i_b + \frac{2}{3L} v_{dc} + \frac{2v_{bn} - (v_{an} + v_{cn})}{3L} \tag{5.32}$$

$$\frac{di_c}{dt} = -\frac{R+R_{on}}{L} i_c - \frac{1}{3L} v_{dc} + \frac{2v_{cn} - (v_{an} + v_{bn})}{3L} \tag{5.33}$$

$$\frac{dv_{dc}}{dt} = -\frac{1}{C} i_b - \frac{1}{CR_l} v_{dc} \tag{5.34}$$

From (5.31)–(5.34), $\mathbf{A}^{\mathbf{cir,cir}}_{\mathbf{on,1}}$ and $\mathbf{A}^{\mathbf{cir,sup}}_{\mathbf{on,1}}$ are obtained as

$$\mathbf{A}^{\mathbf{cir,cir}}_{\mathbf{on,1}} = \begin{bmatrix} -\frac{R+R_{on}}{L} & 0 & 0 & -\frac{1}{3L} \\ 0 & -\frac{R+R_{on}}{L} & 0 & \frac{2}{3L} \\ 0 & 0 & -\frac{R+R_{on}}{L} & -\frac{1}{3L} \\ 0 & -\frac{1}{C} & 0 & -\frac{1}{CR_l} \end{bmatrix} \tag{5.35}$$

$$\mathbf{A}_{\mathbf{on,1}}^{\mathbf{cir,sup}} = \frac{1}{3L}\mathbf{K}_{\mathbf{abc}}^{\mathbf{dc,1}}\mathbf{K}_{\alpha\beta}^{\mathbf{abc}}\mathbf{K}_{\mathbf{h}}^{\alpha\beta} \tag{5.36}$$

where $\mathbf{K}_{\alpha\beta}^{\mathbf{abc}}$ and $\mathbf{K}_{\mathbf{h}}^{\alpha\beta}$ are found from (5.29) and (5.30), respectively, and $\mathbf{K}_{\mathbf{abc}}^{\mathbf{dc,1}}$ is given by

$$\mathbf{K}_{\mathbf{abc}}^{\mathbf{dc,1}} = \begin{bmatrix} 2 & -1 & -1 & 0 \\ -1 & 2 & -1 & 0 \\ -1 & -1 & 2 & 0 \end{bmatrix}^{\mathbb{T}} \tag{5.37}$$

In the next time segment, i.e., $\gamma_1 + \eta_1 \leq t \leq \gamma_2$, D_5 is turned off, and only D_1 and D_6 conduct. The system behaviour becomes similar to that of a DCM conduction interval. Thus, $\mathbf{A}_{\mathbf{off,1}}^{\mathbf{cir,cir}}$, $\mathbf{A}_{\mathbf{off,1}}^{\mathbf{cir,sup}}$, and $\mathbf{K}_{\mathbf{abc,1}}^{\mathbf{dc}}$ of the CCM are equal to $\mathbf{A}_{\mathbf{on,1}}^{\mathbf{cir,cir}}$, $\mathbf{A}_{\mathbf{on,1}}^{\mathbf{cir,sup}}$, and $\mathbf{K}_{\mathbf{abc,1}}^{\mathbf{dc}}$ of the DCM, already given by (5.25), (5.27), and (5.28), respectively.

The CCM's sub-matrices for the other commutation intervals are extracted using the following observations on (5.31)–(5.34):

1. Two equations (i.e., for phases a and c) have similar v_{dc} multipliers, as in (5.31) and (5.33), and the summation of these multipliers is equal to negative the v_{dc} multiplier in (5.32) (i.e., for phase b).

2. Noting the conducting diodes in Figure 5.5, the v_{dc} multiplier is negative in the equation that represents the phase sending the current to the DC side, and is positive otherwise. Also, the v_{dc} multipliers are equal for the phases connected through their diodes.

3. The first and last terms of (5.31)–(5.33) directly correlate with the corresponding phase. Therefore, they remain intact at the other commutation intervals.

4. The DC-side equation given by (5.34) includes a phase current (i_b) whose differential equation has a dissimilar v_{dc} multiplier (as in (5.32)). Also, this multiplier has a sign opposite to that of the phase current in the DC-side equation (5.34).

Based on the above observations, for the rest of the commutation intervals: 1) $\mathbf{A}_{\mathbf{on,i}}^{\mathbf{cir,cir}}$ matrices can be derived, considering the sequence of diode conduction, which is shown in Figure 5.3 for a half-period, and 2) $\mathbf{A}_{\mathbf{on,i}}^{\mathbf{cir,sup}}$ and $\mathbf{K}_{\mathbf{abc}}^{\mathbf{dc,i}}$ matrices are similar to $\mathbf{A}_{\mathbf{on,1}}^{\mathbf{cir,sup}}$ and $\mathbf{K}_{\mathbf{abc}}^{\mathbf{dc,1}}$, given by (5.36) and (5.37), respectively.

Eventually, because the behaviour of CCM when two diodes are conducting is similar to that of DCM conduction intervals, $\mathbf{A}_{\mathbf{off,i}}^{\mathbf{cir,cir}}$ and $\mathbf{A}_{\mathbf{off,i}}^{\mathbf{cir,sup}}$ matrices for the other time segments are derived regarding the explanations of Subsection 5.5.1.

5.6 Mismatch Equation Details

5.6.1 $\mathbf{C_{f,i}}$ and $\mathbf{C_{g,i}}$ Vectors

First, these vectors are provided for the rectifiers with a C filter. Starting with DCM, considering the voltages' boundary conditions given by Table 5.1 at $t = \gamma_i$ for $i \in \{1, 2, ..., 6\}$, $\mathbf{C_{f,i}}$ vectors can be written in the following form:

$$\mathbf{C_{f,i}} = \begin{bmatrix} \mathbf{O_{f,i}} & \mathbf{Q_{f,i}} \end{bmatrix} \tag{5.38}$$

where $\mathbf{O_{f,i}} = \begin{bmatrix} 0 & 0 & 0 & -1 \end{bmatrix}$; $\mathbf{Q_{f,i}}$ are vectors of length $2n_h$, relating the phase voltages required in the boundary conditions to the supply state variables.

To build $\mathbf{Q_{f,i}}$ vectors, a matrix is defined that relates the three-phase voltages to the supply state variables as

$$\mathbf{K_h^{abc}} = \mathbf{K_{\alpha\beta}^{abc}} \mathbf{K_h^{\alpha\beta}} \tag{5.39}$$

where $\mathbf{K_{\alpha\beta}^{abc}}$ and $\mathbf{K_h^{\alpha\beta}}$ were given by (5.29) and (5.30), respectively.

$\mathbf{Q_{f,i}}$ vectors are written in terms of the three rows of $\mathbf{K_h^{abc}}$, represented by $\mathbf{K_h^a}$, $\mathbf{K_h^b}$, and $\mathbf{K_h^c}$, respectively. For example, to hold the voltage boundary condition at $t = \gamma_1$, $\mathbf{Q_{f,1}}$ is written as $\mathbf{Q_{f,1}} = \mathbf{K_h^a} - \mathbf{K_h^b}$ to return $(v_{an} - v_{bn})$ in terms of the supply state variables.

On the other hand, $\mathbf{C_{g,i}}$ vectors are built incorporating the currents' boundary conditions given by Table 5.1 at $t = \gamma_i + \eta_i$ for $i \in \{1, 2, ..., 6\}$, and have the following form:

$$\mathbf{C_{g,i}} = \begin{bmatrix} \mathbf{Q_{g,i}} & \mathbf{0}_{1\times 2n_h} \end{bmatrix} \tag{5.40}$$

where $\mathbf{Q_{g,i}}$ vectors have a length equal to the number of circuit state variables, and their elements are all zero except the one used to express the boundary condition; e.g., holding the condition at $t = \gamma_1 + \eta_1$ needs $\mathbf{Q_{g,1}} = \begin{bmatrix} 1 & 0 & 0 & 0 \end{bmatrix}$.

$\mathbf{C_{f,i}}$ and $\mathbf{C_{g,i}}$ vectors for CCM can also be expressed by (5.38) and (5.40), respectively, once $\mathbf{Q_{f,i}}$ and $\mathbf{Q_{g,i}}$ vectors are written in accordance with Table 5.1 voltages' and currents' boundary conditions, respectively; e.g., boundary conditions at $t = \gamma_1$ and $t = \gamma_1 + \eta_1$ require $\mathbf{Q_{f,1}} = 3\mathbf{K_h^a}$ and $\mathbf{Q_{g,1}} = \begin{bmatrix} 0 & 0 & 1 & 0 \end{bmatrix}$, respectively.

For the case with an LC filter, only $\mathbf{O_{f,i}}$ of (5.38) and $\mathbf{Q_{g,i}}$ of (5.40) must be revised, to: 1) replace v_{dc} with $v_{dc,0}$, and 2) update the supply state variables. For the above CCM example, given that $v_{dc,0} = R_{\text{inf}}\,(-i_b - i_L)$, it is necessary to consider $\mathbf{O_{f,1}} = \begin{bmatrix} 0 & R_{\text{inf}} & 0 & R_{\text{inf}} & 0 \end{bmatrix}$ and $\mathbf{Q_{g,1}} = \begin{bmatrix} 0 & 0 & 1 & 0 & 0 \end{bmatrix}$.

5.6.2 Analytical Jacobian

According to mismatch equations (5.16) and (5.17), the Jacobian matrix has the following form:

$$J = \begin{bmatrix} \frac{\partial f_i}{\partial \eta_k} & \frac{\partial f_i}{\partial \gamma_k} \\ \frac{\partial g_i}{\partial \eta_k} & \frac{\partial g_i}{\partial \gamma_k} \end{bmatrix} \tag{5.41}$$

where $i \in \{1, 2, ..., 6\}$ and $k \in \{1, 2, ..., 6\}$.

Because the vectors $\mathbf{C_{f,i}}$ and $\mathbf{C_{g,i}}$ in (5.16) and (5.17) are constant, the elements of the Jacobian matrix are derived by multiplication of these vectors and the derivative of $\mathbf{X}(\gamma_{i+1})$ and $\mathbf{X}(\gamma_i + \eta_i)$ with respect to η_k and γ_k. Using (6.12) and (5.15), these derivative terms can be written as follows:

$$\frac{\partial}{\partial \eta_k}\mathbf{X}(\gamma_i + \eta_i) = \begin{cases} e^{\mathbf{A_{on,i}}(\eta_i)} \frac{\partial}{\partial \eta_k}\mathbf{X}(\gamma_i), & k \neq i. \\ \mathbf{A_{on,i}} e^{\mathbf{A_{on,i}}(\eta_i)}\mathbf{X}(\gamma_i) + e^{\mathbf{A_{on,i}}(\eta_i)} \frac{\partial}{\partial \eta_k}\mathbf{X}(\gamma_i), & k = i. \end{cases} \tag{5.42a}$$

$$\frac{\partial}{\partial \gamma_k}\mathbf{X}(\gamma_i + \eta_i) = e^{\mathbf{A_{on,i}}(\eta_i)} \frac{\partial}{\partial \gamma_k}\mathbf{X}(\gamma_i) \tag{5.42b}$$

$$\frac{\partial}{\partial \eta_k}\mathbf{X}(\gamma_{i+1}) = \begin{cases} e^{\mathbf{A_{off,i}}(\gamma_{i+1} - \gamma_i - \eta_i)} \frac{\partial}{\partial \eta_k}\mathbf{X}(\gamma_i + \eta_i), & k \neq i. \\ -\mathbf{A_{off,i}} e^{\mathbf{A_{off,i}}(\gamma_{i+1} - \gamma_i - \eta_i)}\mathbf{X}(\gamma_i + \eta_i) + & \\ e^{\mathbf{A_{off,i}}(\gamma_{i+1} - \gamma_i - \eta_i)} \frac{\partial}{\partial \eta_k}\mathbf{X}(\gamma_i + \eta_i), & k = i. \end{cases} \tag{5.42c}$$

$$\frac{\partial}{\partial \gamma_k}\mathbf{X}(\gamma_{i+1}) = \begin{cases} -\mathbf{A_{off,i}} e^{\mathbf{A_{off,i}}(\gamma_{i+1} - \gamma_i - \eta_i)}\mathbf{X}(\gamma_i + \eta_i) + & \\ e^{\mathbf{A_{off,i}}(\gamma_{i+1} - \gamma_i - \eta_i)} \frac{\partial}{\partial \gamma_k}\mathbf{X}(\gamma_i + \eta_i), & k = i. \\ \mathbf{A_{off,i}} e^{\mathbf{A_{off,i}}(\gamma_{i+1} - \gamma_i - \eta_i)}\mathbf{X}(\gamma_i + \eta_i) + & \\ e^{\mathbf{A_{off,i}}(\gamma_{i+1} - \gamma_i - \eta_i)} \frac{\partial}{\partial \gamma_k}\mathbf{X}(\gamma_i + \eta_i), & k = i + 1. \\ e^{\mathbf{A_{off,i}}(\gamma_{i+1} - \gamma_i - \eta_i)} \frac{\partial}{\partial \gamma_k}\mathbf{X}(\gamma_i + \eta_i), & otherwise. \end{cases} \tag{5.42d}$$

Starting from $i = 1$, all the derivative terms of (5.42a)–(5.42d) can be acquired once the derivative terms of $\mathbf{X}(\gamma_1)$, written in terms of its sub-vectors, are given. Using (5.10) and (5.13), the derivatives of $\mathbf{X}(\gamma_1)$ sub-vectors can be expressed as

$$\frac{\partial}{\partial \eta_k}\mathbf{X_{cir}}(\gamma_1) = \mathbf{D^{-1}} \left(\frac{\partial \mathbf{D}}{\partial \eta_k}\mathbf{D^{-1}}\mathbf{E} - \frac{\partial \mathbf{E}}{\partial \eta_k} \right) \mathbf{X_{sup}}(\gamma_1) \tag{5.43a}$$

$$\frac{\partial}{\partial \gamma_k}\mathbf{X_{cir}}\left(\gamma_1\right)=\begin{cases}\mathbf{D^{-1}}\left(\frac{\partial \mathbf{D}}{\partial \gamma_k}\mathbf{D^{-1}E}-\frac{\partial \mathbf{E}}{\partial \gamma_k}\right)\mathbf{X_{sup}}\left(\gamma_1\right), & k\neq 1.\\ \mathbf{D^{-1}}\left(\frac{\partial \mathbf{D}}{\partial \gamma_1}\mathbf{D^{-1}E}-\frac{\partial \mathbf{E}}{\partial \gamma_1}-\mathbf{EA^{sup,sup}}\right)\mathbf{X_{sup}}\left(\gamma_1\right), & k=1.\end{cases} \tag{5.43b}$$

$$\frac{\partial}{\partial \eta_k}\mathbf{X_{sup}}\left(\gamma_1\right)=0 \tag{5.43c}$$

$$\frac{\partial}{\partial \gamma_k}\mathbf{X_{sup}}\left(\gamma_1\right)=\begin{cases}0, & k\neq 1.\\ \mathbf{A^{sup,sup}X_{sup}}\left(\gamma_1\right), & k=1.\end{cases} \tag{5.43d}$$

The derivative terms $\partial\mathbf{D}$ and $\partial\mathbf{E}$ with respect to η_k and γ_k in (5.43a) and (5.43b) can be related to the corresponding derivatives of $\mathbf{\Phi}$ given by (5.6). Using the sub-matrice representation of $\mathbf{\Phi}-\mathbf{I}$ in (5.9), one can write

$$\begin{bmatrix}\partial\mathbf{D} & \partial\mathbf{E}\\ \partial\mathbf{F} & \partial\mathbf{K}\end{bmatrix}=\partial\left(\mathbf{\Phi}-\mathbf{I}\right)=\partial\mathbf{\Phi} \tag{5.44}$$

Eventually, the derivatives of $\mathbf{\Phi}$ with respect to η_k and γ_k are given by:

$$\frac{\partial}{\partial \eta_k}\mathbf{\Phi}=\left(\prod_{j=k+1}^{6}\Psi_{\mathbf{j}}\Theta_{\mathbf{j}}\right)\Psi_{\mathbf{k}}\mathbf{A_{on,k}}\Theta_{\mathbf{k}}\left(\prod_{j=1}^{k-1}\Psi_{\mathbf{j}}\Theta_{\mathbf{j}}\right)-\left(\prod_{j=k+1}^{6}\Psi_{\mathbf{j}}\Theta_{\mathbf{j}}\right)\mathbf{A_{off,k}}\left(\prod_{j=1}^{k}\Psi_{\mathbf{j}}\Theta_{\mathbf{j}}\right) \tag{5.45a}$$

$$\frac{\partial}{\partial \gamma_k}\mathbf{\Phi}=-\left(\prod_{j=k+1}^{6}\Psi_{\mathbf{j}}\Theta_{\mathbf{j}}\right)\mathbf{A_{off,k}}\left(\prod_{j=1}^{k}\Psi_{\mathbf{j}}\Theta_{\mathbf{j}}\right)+\left(\prod_{j=k}^{6}\Psi_{\mathbf{j}}\Theta_{\mathbf{j}}\right)\mathbf{A_{off,k-1}}\left(\prod_{j=1}^{k-1}\Psi_{\mathbf{j}}\Theta_{\mathbf{j}}\right) \tag{5.45b}$$

where $\Theta_{\mathbf{j}}=e^{\mathbf{A_{on,j}}(\eta_j)}$ and $\Psi_{\mathbf{j}}=e^{\mathbf{A_{off,j}}(\gamma_{j+1}-\gamma_j-\eta_j)}$.

5.7 Fourier Analysis

Once the switching instants are acquired, one can obtain the steady-state harmonics of the circuit state variables. The harmonics are acquired here based on the Fourier series analysis. Taking $x(t)$ as a function representing a circuit state variable, the objective is to get the phasors of $x(t)$ harmonics through the Fourier series. The exponential form of the

Fourier series and its coefficients are given by

$$x(t) = \sum_{h=-\infty}^{\infty} C_h e^{jh\omega t} \tag{5.46a}$$

$$C_h = \frac{1}{T}\int_T x(\tau) e^{-jh\omega\tau} d\tau \tag{5.46b}$$

According to (5.46b), the Fourier series coefficients involve integration, hindering the development of a compact formulation that gives the harmonics. To deal with this issue, a fictitious first-order differential equation is developed, whose solution yields the Fourier series coefficient [77]. Then, each harmonic of interest can be obtained by augmenting the system state-space model with a differential equation.

The fictitious differential equation for the h^{th} order harmonic can be written as

$$\frac{dx_h}{dt} = p_h x_h + q_h x(t) \tag{5.47}$$

where p_h and q_h are the differential equation coefficients, and x_h returns the harmonic of $x(t)$. The solution of (5.47) on a period, which is required by the Fourier series integral, results in

$$x_h(\gamma_1 + T) = e^{p_h T} x_h(\gamma_1) + \int_{\gamma_1}^{\gamma_1+T} e^{-p_h(\tau-\gamma_1-T)} q_h x(\tau)\, d\tau \tag{5.48}$$

Assuming $x_h(\gamma_1) = 0$, a comparison between (5.46b) and (5.48) shows that holding $x_h(\gamma_1 + T) = C_h$ requires the differential equation coefficients to be equal to the following complex numbers:

$$p_h = jh\omega \tag{5.49a}$$

$$q_h = \frac{1}{T} e^{-jh\omega(\gamma_1+T)} \tag{5.49b}$$

Considering the augmented state-space vector as $\tilde{\mathbf{X}} = \left[\ \mathbf{X_{cir}}^{\mathbb{T}} \quad \mathbf{X_{sup}}^{\mathbb{T}} \quad \mathbf{X_{har}}^{\mathbb{T}}\ \right]^{\mathbb{T}}$, its state-space model can be built. $\mathbf{X_{har}}$ consists of the harmonic state variables and is given by $\mathbf{X_{har}} = \left[\ \mathbf{i_{a,h}} \quad \mathbf{i_{b,h}} \quad \mathbf{i_{c,h}} \quad \mathbf{v_{dc,h}}\ \right]^{\mathbb{T}}$, where $\mathbf{i_{a,h}}$, $\mathbf{i_{b,h}}$, $\mathbf{i_{c,h}}$, and $\mathbf{v_{dc,h}}$ are sub-vectors comprising the harmonics of the circuit state variables, and each sub-vector can be generally represented by $\mathbf{x_h} = \left[\ x_0 \quad \ldots \quad x_h \quad \ldots\ \right]$. The augmented system state-space model has

the same form already described by (5.3) and (5.4), but in this case, the state-transition matrices are expressed by

$$\tilde{\mathbf{A}}_{\mathbf{on,i}} = \begin{bmatrix} \mathbf{A}_{\mathbf{on,i}}^{\mathbf{cir,cir}} & \mathbf{A}_{\mathbf{on,i}}^{\mathbf{cir,sup}} & \mathbf{0}_{4\times 4n_h^o} \\ \mathbf{0}_{2n_h\times 4} & \mathbf{A}^{\mathbf{sup,sup}} & \mathbf{0}_{2n_h\times 4n_h^o} \\ \mathbf{A}^{\mathbf{har,cir}} & \mathbf{0}_{4n_h^o\times 2n_h} & \mathbf{A}^{\mathbf{har,har}} \end{bmatrix} \tag{5.50}$$

$$\tilde{\mathbf{A}}_{\mathbf{off,i}} = \begin{bmatrix} \mathbf{A}_{\mathbf{on,i}}^{\mathbf{cir,cir}} & \mathbf{A}_{\mathbf{on,i}}^{\mathbf{cir,sup}} & \mathbf{0}_{4\times 4n_h^o} \\ \mathbf{0}_{2n_h\times 4} & \mathbf{A}^{\mathbf{sup,sup}} & \mathbf{0}_{2n_h\times 4n_h^o} \\ \mathbf{A}^{\mathbf{har,cir}} & \mathbf{0}_{4n_h^o\times 2n_h} & \mathbf{A}^{\mathbf{har,har}} \end{bmatrix} \tag{5.51}$$

where $\mathbf{A}^{\mathbf{har,cir}}$ and $\mathbf{A}^{\mathbf{har,har}}$ are expressed by (5.52a)–(5.52d). Representing the number of interested harmonics as n_h^o, the size of these matrices will be $4n_h^o \times 4$ and $4n_h^o \times 4n_h^o$, respectively. Since the harmonics of interest are usually different at the AC and DC sides, the subscripts h, ac and h, dc are used as the harmonic orders at the AC and DC sides, respectively.

$$\mathbf{A}^{\mathbf{har,cir}} = diag(\mathbf{q_{h,ac}}, \mathbf{q_{h,ac}}, \mathbf{q_{h,ac}}, \mathbf{q_{h,dc}}) \tag{5.52a}$$

$$\mathbf{A}^{\mathbf{har,har}} = diag(\mathbf{p_{h,ac}}, \mathbf{p_{h,ac}}, \mathbf{p_{h,ac}}, \mathbf{p_{h,dc}}) \tag{5.52b}$$

$$\mathbf{q_{h,ac/dc}} = \begin{bmatrix} q_0 & \cdots & q_{h,ac/h,dc} & \cdots \end{bmatrix}^{\mathbb{T}} \tag{5.52c}$$

$$\mathbf{p_{h,ac/dc}} = diag(p_0, ..., p_{h,ac/h,dc}, ...)^{\mathbb{T}} \tag{5.52d}$$

The augmented state-space vector at $t = \gamma_1 + T$, $\tilde{\mathbf{X}}(\gamma_1 + T)$ gives the harmonics. Due to the similarity of the augmented and the system state-space models, $\tilde{\mathbf{X}}(\gamma_1 + T)$ can be written in terms of $\tilde{\mathbf{X}}(\gamma_1)$ as

$$\tilde{\mathbf{X}}(\gamma_1 + T) = \tilde{\mathbf{\Phi}}\tilde{\mathbf{X}}(\gamma_1) \tag{5.53}$$

where $\tilde{\mathbf{\Phi}}$ can be obtained from (5.6), once $\mathbf{A_{on,i}}$ and $\mathbf{A_{off,i}}$ are replaced by the augmented state transition matrices described by (5.50) and (5.51), respectively.

Given that $\mathbf{X_{cir}}(\gamma_1)$ and $\mathbf{X_{sup}}(\gamma_1)$ have been already obtained, and $\mathbf{X_{har}}(\gamma_1)$ is a zero vector, $\tilde{\mathbf{X}}(\gamma_1)$ is known. Thus, determines $\tilde{\mathbf{X}}(\gamma_1 + T)$ and the harmonics.

It is worth noting that the calculation of any harmonic is independent of the calculation of other harmonics considered in the formulation, which speeds up the calculation process and avoids propagating truncation errors. Unlike those developed in [83] and [84], the proposed method provides a single formulation for both DCM and CCM that is independent

of the network's X/R ratio.

5.8 Model Extension to LC Filter

Although diode rectifiers are abundantly furnished with C filters at the DC side, LC filters [Figure 5.1b] can also be found in many high power applications [132]. Replacing C filters with LC filters adds to the complexity of the model, especially for CCM, for the following reason. The turn-on boundary conditions that require the rectifier's output voltage cannot be directly developed. However, in the case of C filters, this voltage is a state variable, which is used in constructing the turn-on boundary conditions. In [83], a circuit consisting of a fictitious voltage and two fictitious resistances have been proposed to obtain the boundary conditions. But, these conditions have not been defined based on the state variables, and accordingly, cannot be used for the method proposed in this chapter.

On the other hand, the LC filter leads to an inductive cut-set between the inductors of the DC and AC filters. Due to this cut-set, the inductor current of the DC filter (i_L) cannot be considered as an independent state variable, and must be replaced by the AC currents. As a consequence, the state-space model of a time segment involves more-complicated terms than does the C filter case, and it is impossible to extend the state-space model of a time segment to the other time segments of a period using the observations detailed in Section 5.5.

To deal with the above-mentioned issues, it is proposed here to add a large virtual resistance, R_{inf}, at the output of the rectifier [Figure 5.1b]. This resistance eliminates the inductive cut-set between the inductors of the DC and AC filters. Further, it allows writing the rectifier's output voltage ($v_{dc,0}$) in terms of the system state variables, and accordingly, constructing the required turn-on boundary conditions.

Adding R_{inf}, the state-space model of the system with an LC filter can be easily developed by replacing v_{dc} of the previous model with $v_{dc,0}$ written in terms of the circuit state variables, which are updated to include i_L as $\mathbf{X_{cir}} = \begin{bmatrix} i_a & i_b & i_c & i_L & v_{dc} \end{bmatrix}^{\mathbb{T}}$. For brevity's sake, only the equations relevant to the first two time segments of CCM are presented here. The equations for the rest of the time segments, as well as the DCM, can be derived in the same manner. Deriving the model for the case with an LC filter includes updating the sub-matrices in (5.19) and (5.20) for $i = 1$. Given that the voltage drops across R_{inf} for these time segments are $v_{dc,0} = R_{\text{inf}}\,(-i_b - i_L)$ and $v_{dc,0} = R_{\text{inf}}\,(i_a - i_L)$, respectively, $\mathbf{A}^{\mathbf{cir,cir}}_{\mathbf{on,1}}$ and $\mathbf{A}^{\mathbf{cir,cir}}_{\mathbf{off,1}}$ can be written as

$$\mathbf{A}^{\mathbf{cir,cir}}_{\mathbf{on,1}} = \begin{bmatrix} -\frac{R+R_{on}}{L} & \frac{R_{\inf}}{3L} & 0 & \frac{R_{\inf}}{3L} & 0 \\ 0 & -\left(\frac{R+R_{on}}{L}+\frac{2R_{\inf}}{3L}\right) & 0 & -\frac{2R_{\inf}}{3L} & 0 \\ 0 & \frac{R_{\inf}}{3L} & -\frac{R+R_{on}}{L} & \frac{R_{\inf}}{3L} & 0 \\ 0 & -\frac{R_{\inf}}{L_{dc}} & 0 & -\frac{R_{\inf}+R_{dc}}{L_{dc}} & -\frac{1}{L_{dc}} \\ 0 & 0 & 0 & \frac{1}{C} & -\frac{1}{CR_l} \end{bmatrix} \tag{5.54}$$

$$\mathbf{A}^{\mathbf{cir,cir}}_{\mathbf{off,1}} = \begin{bmatrix} -\frac{2(R+R_{on})+R_{\inf}}{2L} & 0 & 0 & \frac{R_{\inf}}{2L} & 0 \\ \frac{R_{\inf}}{2L} & -\frac{R+R_{on}}{L} & 0 & -\frac{R_{\inf}}{2L} & 0 \\ -\frac{R_{\inf}}{2L} & 0 & -\frac{R+R_{off}}{L} & \frac{R_{\inf}}{2L} & 0 \\ \frac{R_{\inf}}{L_{dc}} & 0 & 0 & -\frac{R_{\inf}+R_{dc}}{L_{dc}} & -\frac{1}{L_{dc}} \\ 0 & 0 & 0 & \frac{1}{C} & -\frac{1}{CR_l} \end{bmatrix} \tag{5.55}$$

No change is required for $\mathbf{A}^{\mathbf{sup,sup}}$, and the other two sub-matrices $\mathbf{A}^{\mathbf{cir,sup}}_{\mathbf{on,1}}$ and $\mathbf{A}^{\mathbf{cir,sup}}_{\mathbf{off,1}}$ are obtained from (5.27) and (5.36) once $\mathbf{K}^{\mathbf{dc,1}}_{\mathbf{abc}}$ is updated to account for the change in the circuit state variables. This update can be simply done by adding a row of zeros as the last row of the matrices in (5.28) and (5.37).

Eventually, to obtain the harmonics for the case with an LC filter, the sub-matrices of the augmented state transition matrices must be revised. Thus, $\mathbf{A}^{\mathbf{har,cir}}$ and $\mathbf{A}^{\mathbf{har,har}}$, already given by (5.52a) and (5.52b), respectively, must be updated as

$$\mathbf{A}^{\mathbf{cir,har}} = diag(\mathbf{q_{h,ac}}, \mathbf{q_{h,ac}}, \mathbf{q_{h,ac}}, \mathbf{q_{h,dc}}, \mathbf{q_{h,dc}}) \tag{5.56a}$$

$$\mathbf{A}^{\mathbf{har,har}} = diag(\mathbf{p_{h,ac}}, \mathbf{p_{h,ac}}, \mathbf{p_{h,ac}}, \mathbf{p_{h,dc}}, \mathbf{p_{h,dc}}) \tag{5.56b}$$

The addition of R_{inf} actually decouples the dynamic equations of the AC and DC sides, allowing modelling of even more-sophisticated filters at the DC side, e.g., two-stage LC filters. Moreover, this idea can be employed in modelling rectifiers with higher pulse numbers, such as 12-pulse rectifiers.

The proposed method for the harmonic analysis of diode bridge rectifiers is summarized in Algorithm 2.

Algorithm 2 Harmonic Analysis for Diode Bridge Rectifier

1: Select the operation mode: DCM or CCM.
2: /* Calculating The Switching Instants
3: Initialize $\mathbf{\Delta} = [\eta_1, \gamma_1, ..., \eta_6, \gamma_6]^{\mathbb{T}}$.
4: Calculate $\mathbf{A_{on,i}}$ and $\mathbf{A_{off,i}}$, for all i, using (5.19) and (5.20).
5: **while** max $\left(\left|\mathbf{\Delta}^{(\mathbf{j+1})} - \mathbf{\Delta}^{(\mathbf{j})}\right|\right) < \varepsilon$ **do**
6: Build the mismatch equations, using (5.16) and (5.17).
7: Construct the Jacobian matrix, using (5.41).
8: Update $\mathbf{\Delta}^{(\mathbf{j+1})}$, using (5.18).
9: $\mathbf{j = j + 1}$
10: **end while**
11: /* Calculating The Harmonics
12: Calculate $\tilde{\mathbf{A}}_{\mathbf{on,i}}$ and $\tilde{\mathbf{A}}_{\mathbf{off,i}}$, for all i, using (5.50) and (5.51).
13: Obtain $\tilde{\mathbf{X}}(\gamma_1 + T)$, using (5.53).
14: Get $\mathbf{X_{har}}(\gamma_1 + T)$, using $\tilde{\mathbf{X}} = \left[\ \mathbf{X_{cir}}^{\mathbb{T}} \quad \mathbf{X_{sup}}^{\mathbb{T}} \quad \mathbf{X_{har}}^{\mathbb{T}}\ \right]^{\mathbb{T}}$.

5.9 Performance Evaluation

The effectiveness of the proposed method is evaluated through comparative studies with PSCAD/EMTDC time-domain simulations in several case studies.

5.9.1 Rectifiers with LC Filters

The case with LC filter as displayed by the circuit in Figure 5.1b is investigated here. Two sets of system parameters that result in DCM and CCM, respectively, are considered, and are given in Appendix C.

First, the switching instants γ_i and $\gamma_i + \eta_i$ are acquired using the Newton method with the proposed Jacobian matrix. The proposed method shows a very fast convergence for both DCM and CCM. For example, with a tolerance of 10^{-6}, the convergence for the CCM has been achieved within 7 iterations, taking 25 ms on a machine with a core i7 CPU and 16 GB RAM in MATLAB environment. To validate the switching instants, the current waveforms for one period are obtained by PSCAD/EMTDC and the proposed model. Figures 5.6 and 5.7 show the results for the DCM and CCM, respectively. In both figures, excellent matching exists between the two sets of currents so that they cross the zero axis at the same points, which indicates the capability of the proposed model in extracting the switching instants.

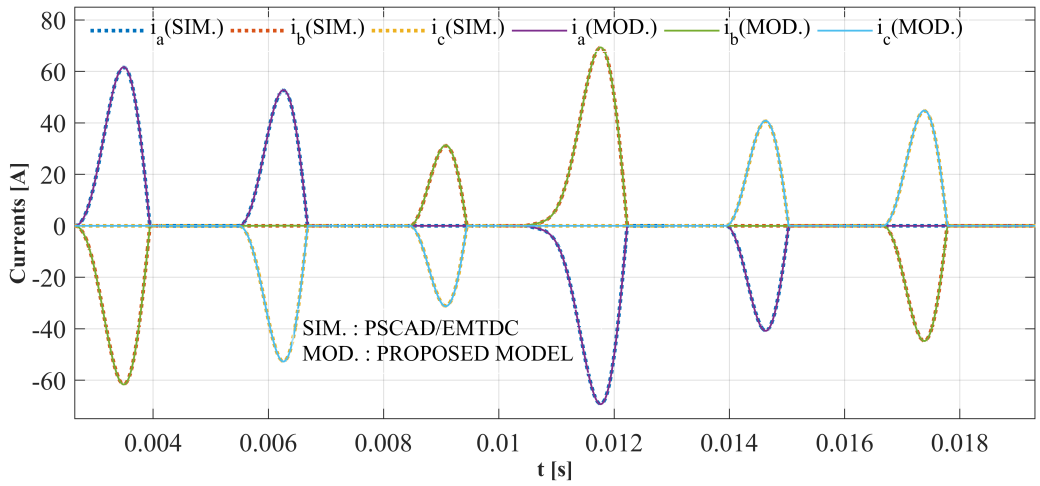

Figure 5.6: DCM current waveforms using the proposed model and PSCAD.

Second, the harmonic phasors obtained using the proposed method are compared with those given by PSCAD/EMTDC time-domain simulations with a sample time of 1 μs and simulation time of 1 s. Tables 5.2 and 5.3 illustrate such a comparison for the DCM and CCM, respectively, for all harmonics up to the 13^{th} order. The results show accurate compliance of the proposed model with the time-domain simulations. According to Table 5.2, in terms of the magnitudes of the current harmonics, the average absolute error is 0.001 A, and the highest absolute error, which has happened for the third harmonic of phase b, is 0.007 A. These errors are very small and correspond to 0.009% and 0.04%, respectively, when referred to the base value of the fundamental current (i.e., 15.65 A). In terms of the angles of the current harmonics, the average and highest absolute errors are only 0.1° and 0.4°, respectively. For the magnitudes of the DC voltage harmonics, Table 5.2 demonstrates the average and highest absolute errors of 0.001 V and 0.004 V, respectively, which in the base of the system DC voltage (292.15 V) are equivalent to 0.0003% and 0.001%, respectively. The average and highest absolute errors for the angles of the DC voltage harmonics are 0.1° and 0.2°, respectively. Analysis of the data for the CCM in Table 5.3 will draw similar conclusions.

Eventually, for the DCM and CCM, respectively, the model needs the total execution times of around 180 ms and 150 ms, in MATLAB environment, to provide all harmonics of i_a, i_b, i_c, and v_{dc} up to the 30^{th} order. In contrast, the PSCAD/EMTDC model (simulated using a sample time of 10 μs and simulation time of 1 s) requires around 18 s to complete the same task. The reason for the significant difference in the total execution times is that

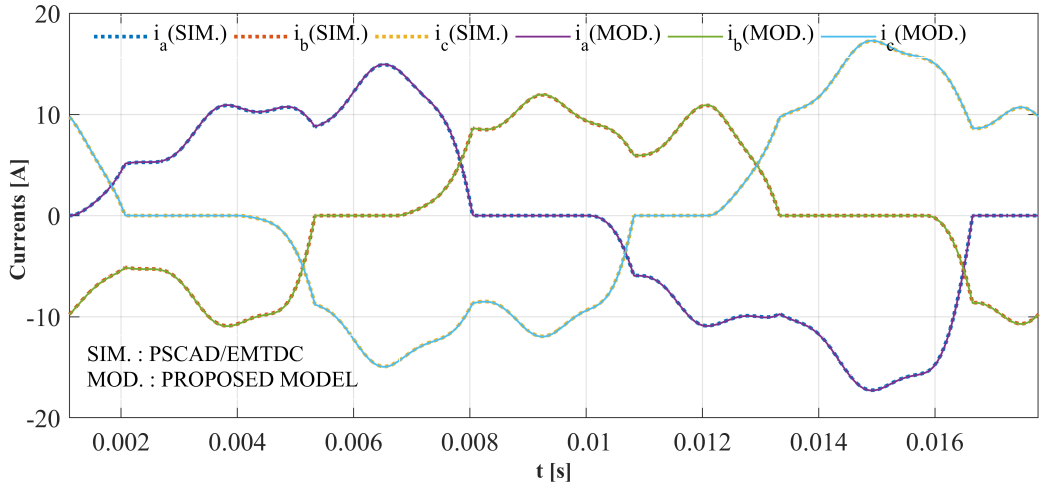

Figure 5.7: CCM current waveforms using the proposed model and PSCAD.

PSCAD/EMTDC integrates the system differential equations until the system reaches the steady-state point in which the harmonics should be calculated; however, the proposed method avoids the system transients and directly targets the steady-state point, and accordingly, is much faster. The two sample times considered above for the PSCAD/EMTDC model are based on the following rational. A sample time of 1 μs improves the accuracy of the PSCAD/EMTDC model that is regarded as the benchmark and allows evaluating the proposed method accuracy. On the other hand, a sample time of 10 μs has been considered for speed evaluation, given that this sample time in addition to decreasing the execution time can still provide acceptable results [84]. To further assess the execution time of the proposed method, its C-code has been generated. The execution times for the DCM and CCM are around 24 ms and 20 ms, respectively. This confirms that the speed of the proposed method is at the same order of those in [83] and [84].

5.9.2 Rectifiers with Two-Stage LC Filters

Two cascaded LC filters [Figure 5.8] can be applied to provide a qualified filtering through using filter inductive and capacitive elements with a lower rating, and accordingly, a two-stage filter is more effective than a single-stage one [133, 134]. As explained in Section 5.8, addition of R_{inf} makes the harmonic analysis of rectifiers with two-stage LC filters possible. By Updating the circuit state variables as $\mathbf{X_{cir}} = \begin{bmatrix} i_a & i_b & i_c & i_{L,1} & i_{L,2} & v_{dc,1} & v_{dc,2} \end{bmatrix}^{\mathbb{T}}$, and including the following two differential equations in the model given in Section 5.8,

Table 5.2: Harmonic Phasors of AC and DC side for DCM

	$\hat{I}_{a,h}(A)$		$\hat{I}_{b,h}(A)$		$\hat{I}_{c,h}(A)$		$\hat{V}_{dc,h}(V)$	
h	MODEL	PSCAD	MODEL	PSCAD	MODEL	PSCAD	MODEL	PSCAD
0	**0.019∠-90.0°**	**0.021∠-90.0°**	**0.014∠-90.0°**	**0.015∠-90.0°**	**0.033∠90.0°**	**0.037∠90.0°**	**292.149∠90.0°**	**292.150∠90.0°**
1	**15.649∠-5.6°**	**15.647∠-5.6°**	**14.612∠-145.1°**	**14.611∠-145.1°**	**10.517∠109.9°**	**10.515∠109.9°**	**0.695∠-138.3°**	**0.694∠-138.3°**
-2	**2.122∠164.7°**	**2.122∠164.8°**	**1.803∠-76.1°**	**1.802∠-76.0°**	**2.004∠36.5°**	**2.004∠36.5°**	**13.355∠-151.8°**	**13.355∠-151.8°**
3	**4.055∠-121.6°**	**4.055∠-121.6°**	**5.613∠55.7°**	**5.606∠55.8°**	**1.566∠-131.0°**	**1.566∠-130.9°**	**5.884∠-23.4°**	**5.883∠-23.5°**
4	**1.571∠-26.9°**	**1.569∠-26.9°**	**2.262∠-153.5°**	**2.261∠-153.4°**	**1.831∠70.0°**	**1.830∠70.1°**	**6.632∠93.8°**	**6.632∠93.7°**
-5	**14.514∠105.2°**	**14.511∠105.2°**	**12.470∠-116.6°**	**12.469∠-116.4°**	**9.768∠-17.0°**	**9.765∠-16.9°**	**0.884∠-85.5°**	**0.884∠-85.6°**
6	**0.810∠-60.6°**	**0.809∠-60.6°**	**0.964∠120.4°**	**0.964∠120.6°**	**0.156∠-53.2°**	**0.156∠-53.1°**	**17.645∠-81.2°**	**17.641∠-81.2°**
7	**11.989∠-89.0°**	**11.987∠-89.0°**	**12.075∠134.1°**	**12.072∠134.3°**	**8.876∠22.0°**	**8.874∠22.1°**	**0.720∠150.5°**	**0.719∠150.4°**
-8	**1.970∠112.7°**	**1.967∠112.8°**	**0.987∠-123.2°**	**0.987∠-123.0°**	**1.632∠-37.3°**	**1.631∠-37.3°**	**2.061∠133.5°**	**2.060∠133.4°**
9	**2.423∠172.8°**	**2.423∠172.9°**	**3.432∠-15.5°**	**3.428∠-15.2°**	**1.083∠146.4°**	**1.083∠146.5°**	**1.387∠-86.2°**	**1.386∠-86.4°**
10	**0.923∠-76.1°**	**0.922∠-76.1°**	**1.749∠145.9°**	**1.748∠146.1°**	**1.232∠-3.8°**	**1.231∠-3.7°**	**1.581∠22.5°**	**1.580∠22.3°**
-11	**9.430∠21.2°**	**9.429∠21.3°**	**7.719∠153.9°**	**7.719∠154.3°**	**7.014∠-105.3°**	**7.013∠-105.1°**	**0.409∠-152.2°**	**0.408∠-152.4°**
12	**0.699∠-122.6°**	**0.699∠-122.6°**	**0.871∠53.9°**	**0.871∠54.3°**	**0.177∠-138.3°**	**0.177∠-138.2°**	**5.533∠-170.6°**	**5.532∠-170.8°**
13	**6.739∠178.7°**	**6.738∠178.8°**	**7.028∠47.8°**	**7.027∠48.1°**	**5.753∠-69.3°**	**5.752∠-69.2°**	**0.302∠85.9°**	**0.302∠85.8°**

the harmonic analysis of rectifiers with two-stage LC filters can be accommodated.

$$\frac{di_{L,2}}{dt} = -\frac{R_{dc,2}}{L_{dc,2}} i_{L,2} + \frac{1}{L_{dc,2}} v_{dc,1} - \frac{1}{L_{dc,2}} v_{dc,2} \tag{5.57}$$

$$\frac{dv_{dc,1}}{dt} = \frac{1}{C_1} i_{L,1} - \frac{1}{C_1} i_{L,2} \tag{5.58}$$

The inclusion of (5.57) and (5.58) changes $\mathbf{A}^{\mathbf{cir,cir}}_{\mathbf{on,i}}$ and $\mathbf{A}^{\mathbf{cir,cir}}_{\mathbf{off,i}}$ sub-matrices. For instance, $\mathbf{A}^{\mathbf{cir,cir}}_{\mathbf{on,1}}$ and $\mathbf{A}^{\mathbf{cir,cir}}_{\mathbf{off,1}}$ are given by

$$\mathbf{A}^{\mathbf{cir,cir}}_{\mathbf{on,1}} = \begin{bmatrix} -\frac{R+R_{on}}{L} & \frac{R_{\inf}}{3L} & 0 & \frac{R_{\inf}}{3L} & 0 & 0 & 0 \\ 0 & -\left(\frac{R+R_{on}}{L} + \frac{2R_{\inf}}{3L}\right) & 0 & -\frac{2R_{\inf}}{3L} & 0 & 0 & 0 \\ 0 & \frac{R_{\inf}}{3L} & -\frac{R+R_{on}}{L} & \frac{R_{\inf}}{3L} & 0 & 0 & 0 \\ 0 & -\frac{R_{\inf}}{L_{dc,1}} & 0 & -\frac{R_{\inf}+R_{dc,1}}{L_{dc,1}} & 0 & -\frac{1}{L_{dc}} & 0 \\ 0 & 0 & 0 & 0 & -\frac{R_{dc,2}}{L_{dc,2}} & \frac{1}{L_{dc,2}} & -\frac{1}{L_{dc,2}} \\ 0 & 0 & 0 & \frac{1}{C_1} & -\frac{1}{C_1} & 0 & 0 \\ 0 & 0 & 0 & 0 & \frac{1}{C_2} & 0 & -\frac{1}{C_2 R_l} \end{bmatrix} \tag{5.59}$$

Table 5.3: Harmonic Phasors of AC and DC side for CCM

	$\hat{I}_{a,h}(A)$		$\hat{I}_{b,h}(A)$		$\hat{I}_{c,h}(A)$		$\hat{V}_{dc,h}(V)$	
h	MODEL	PSCAD	MODEL	PSCAD	MODEL	PSCAD	MODEL	PSCAD
0	**0.516∠-90.0°**	**0.513∠-90.0°**	**0.165∠90.0°**	**0.172∠90.0°**	**0.337∠90.0°**	**0.341∠90.0°**	**262.466∠90.0°**	**262.466∠90.0°**
1	**12.660∠-27.8°**	**12.664∠-27.8°**	**9.247∠-137.4°**	**9.238∠-137.4°**	**12.934∠109.9°**	**12.933∠109.9°**	**2.097∠74.6°**	**2.099∠74.6°**
-2	**1.257∠-34.4°**	**1.253∠-34.5°**	**1.228∠59.8°**	**1.225∠59.7°**	**1.690∠-168.0°**	**1.688∠-168.1°**	**4.318∠74.5°**	**4.319∠74.5°**
3	**2.042∠19.9°**	**2.044∠20.0°**	**0.497∠-93.1°**	**0.498∠-93.6°**	**1.902∠-173.9°**	**1.901∠-174.0°**	**0.923∠79.5°**	**0.926∠79.6°**
4	**0.837∠-23.8°**	**0.836∠-24.0°**	**0.688∠-141.5°**	**0.687∠-141.5°**	**0.802∠106.6°**	**0.800∠106.4°**	**0.331∠104.8°**	**0.333∠104.7°**
-5	**2.755∠64.1°**	**2.755∠64.1°**	**2.993∠-160.5°**	**2.993∠-160.2°**	**2.179∠-42.2°**	**2.179∠-42.3°**	**0.089∠41.9°**	**0.089∠42.0°**
6	**0.274∠-64.8°**	**0.274∠-64.8°**	**0.101∠52.1°**	**0.101∠52.9°**	**0.245∠136.7°**	**0.244∠136.6°**	**0.835∠-148.9°**	**0.834∠-149.0°**
7	**0.758∠101.2°**	**0.758∠101.3°**	**0.306∠21.7°**	**0.307∠22.4°**	**0.870∠-99.0°**	**0.870∠-99.0°**	**0.033∠37.6°**	**0.033∠37.4°**
-8	**0.508∠38.4°**	**0.507∠38.5°**	**0.770∠167.5°**	**0.769∠167.9°**	**0.594∠-53.3°**	**0.594∠-53.3°**	**0.068∠159.2°**	**0.068∠159.3°**
9	**0.472∠51.3°**	**0.472∠51.3°**	**0.259∠-142.5°**	**0.259∠-142.0°**	**0.227∠-113.4°**	**0.227∠-113.5°**	**0.078∠155.0°**	**0.079∠154.9°**
10	**0.499∠31.1°**	**0.498∠31.2°**	**0.234∠-77.0°**	**0.233∠-76.4°**	**0.483∠-176.2°**	**0.482∠-176.3°**	**0.042∠138.8°**	**0.042∠138.7°**
-11	**0.407∠38.6°**	**0.407∠38.7°**	**0.154∠-146.3°**	**0.154∠-145.5°**	**0.254∠-138.7°**	**0.254∠-138.8°**	**0.018∠100.9°**	**0.018∠100.9°**
12	**0.277∠-17.9°**	**0.277∠-17.8°**	**0.149∠152.7°**	**0.149∠153.5°**	**0.132∠172.3°**	**0.131∠172.1°**	**0.150∠156.5°**	**0.151∠156.4°**
13	**0.617∠115.4°**	**0.617∠115.5°**	**0.422∠-12.5°**	**0.421∠-11.7°**	**0.494∠-107.3°**	**0.494∠-107.2°**	**0.020∠64.9°**	**0.019∠64.9°**

$$\mathbf{A}_{\mathbf{off},\mathbf{1}}^{\mathbf{cir},\mathbf{cir}} = \begin{bmatrix} -\frac{2(R+R_{on})+R_{\inf}}{2L} & 0 & 0 & \frac{R_{\inf}}{2L} & 0 & 0 & 0 \\ \frac{R_{\inf}}{2L} & -\frac{R+R_{on}}{L} & 0 & -\frac{R_{\inf}}{2L} & 0 & 0 & 0 \\ -\frac{R_{\inf}}{2L} & 0 & -\frac{R+R_{on}}{L} & \frac{R_{\inf}}{2L} & 0 & 0 & 0 \\ \frac{R_{\inf}}{L_{dc,1}} & 0 & 0 & -\frac{R_{\inf}+R_{dc,1}}{L_{dc,1}} & 0 & -\frac{1}{L_{dc,1}} & 0 \\ 0 & 0 & 0 & 0 & -\frac{R_{dc,2}}{L_{dc,2}} & \frac{1}{L_{dc,2}} & -\frac{1}{L_{dc,2}} \\ 0 & 0 & 0 & \frac{1}{C_1} & -\frac{1}{C_1} & 0 & 0 \\ 0 & 0 & 0 & 0 & \frac{1}{C_2} & 0 & -\frac{1}{C_2 R_l} \end{bmatrix} \tag{5.60}$$

To show the capability of the proposed model in the harmonic analysis of rectifiers with two-stage LC filters, other studies are conducted using two sets of parameters [Appendix C] that result in DCM and CCM, respectively. Table 5.4 illustrates the harmonic phasors of the AC side current (i_a) and DC side voltage ($v_{dc,2}$) obtained from the proposed model and PSCAD/EMTDC time-domain simulations for both DCM and CCM. Again, the proposed algorithm provides very accurate results for both magnitudes and angles of different harmonic orders.

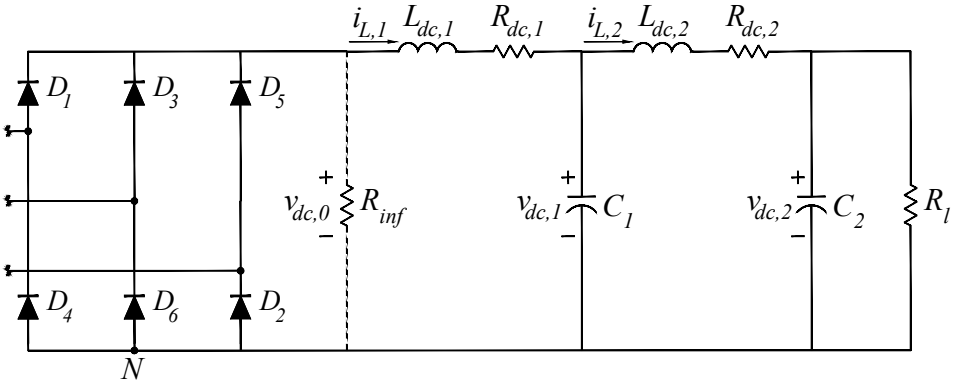

Figure 5.8: Rectifier with two-stage LC filter.

Table 5.4: Harmonic Phasors for Two-stage LC Filters

	DCM				CCM			
	$\hat{I}_{a,h}(A)$		$\hat{V}_{dc,2,h}(V)$		$\hat{I}_{a,h}(A)$		$\hat{V}_{dc,2,h}(V)$	
h	MODEL	PSCAD	MODEL	PSCAD	MODEL	PSCAD	MODEL	PSCAD
0	**0.058∠-90.0°**	**0.057∠-90.0°**	**285.000∠90.0°**	**285.008∠90.0°**	**0.574∠-90.0°**	**0.575∠-90.0°**	**262.116∠90.0°**	**262.114∠90.0°**
1	**14.533∠-13.9°**	**14.531∠-13.9°**	**0.223∠97.5°**	**0.222∠97.5°**	**12.982∠-30.1°**	**12.988∠-30.1°**	**2.455∠88.1°**	**2.458∠88.1°**
-2	**0.866∠-35.1°**	**0.866∠-35.1°**	**3.559∠221.3°**	**3.559∠221.3°**	**1.019∠-37.2°**	**1.019∠-37.2°**	**6.114∠72.4°**	**6.115∠72.5°**
3	**1.318∠-141.5°**	**1.319∠-141.5°**	**1.341∠194.2°**	**1.342∠194.2°**	**2.419∠23.8°**	**2.421∠23.8°**	**1.527∠69.3°**	**1.527∠69.4°**
4	**0.882∠98.4°**	**0.882∠98.3°**	**1.722∠178.4°**	**1.722∠178.4°**	**0.835∠-15.4°**	**0.835∠-15.4°**	**0.913∠90.8°**	**0.916∠90.8°**
-5	**13.172∠94.1°**	**13.169∠94.0°**	**0.123∠-29.4°**	**0.123∠-29.4°**	**3.345∠61.6°**	**3.346∠61.6°**	**0.544∠2.3°**	**0.545∠2.5°**
6	**0.175∠-151.0°**	**0.175∠-151.1°**	**10.095∠38.9°**	**10.093∠38.9°**	**0.282∠-69.1°**	**0.282∠-69.1°**	**3.742∠65.7°**	**3.741∠65.8°**
7	**12.017∠-114.7°**	**12.015∠-114.8°**	**0.047∠206.7°**	**0.047∠206.7°**	**0.728∠131.8°**	**0.727∠131.8°**	**0.061∠-137.0°**	**0.062∠-136.9°**
-8	**0.535∠-156.2°**	**0.535∠-156.3°**	**0.765∠249.5°**	**0.765∠249.4°**	**0.478∠31.2°**	**0.478∠31.2°**	**0.074∠-7.0°**	**0.074∠-6.8°**
9	**0.725∠110.6°**	**0.726∠110.5°**	**0.385∠210.6°**	**0.385∠210.5°**	**0.507∠56.6°**	**0.508∠56.6°**	**0.053∠-14.8°**	**0.052∠-14.6°**
10	**0.615∠-25.5°**	**0.615∠-25.6°**	**0.545∠210.5°**	**0.546∠210.5°**	**0.438∠35.3°**	**0.438∠35.3°**	**0.023∠-33.3°**	**0.023∠-33.2°**
-11	**8.775∠-6.7°**	**8.774∠-6.8°**	**0.113∠9.9°**	**0.113∠9.8°**	**0.499∠31.6°**	**0.499∠31.7°**	**0.007∠-63.7°**	**0.007∠-63.4°**
12	**0.220∠114.9°**	**0.219∠114.7°**	**5.876∠74.0°**	**5.875∠74.0°**	**0.271∠-17.7°**	**0.272∠-17.7°**	**0.044∠-20.1°**	**0.044∠-19.9°**
13	**7.221∠140.9°**	**7.220∠140.7°**	**0.072∠240.7°**	**0.072∠240.6°**	**0.681∠117.8°**	**0.681∠117.8°**	**0.005∠-112.6°**	**0.005∠-112.4°**

5.9.3 Harmonic Analysis Under Low X/R Ratio

The proposed model is independent of the X/R ratio of a rectifier's circuit. It is worth noting that facing rectifiers in circuits with low values of X/R ratio is possible. As an example, one can consider a rectifier at the front end of a low-power VSD that is connected to a distribution system without a filter [135]. Distribution systems are characterized by their feeders' low values of X/R ratio [136, 137]. Therefore, the described rectifier

Table 5.5: Harmonic Phasors for CCM with Low X/R ratio

	$\hat{I}_{a,h}(A)$		$\hat{I}_{b,h}(A)$		$\hat{I}_{c,h}(A)$		$\hat{V}_{dc,h}(V)$	
h	MODEL	PSCAD	MODEL	PSCAD	MODEL	PSCAD	MODEL	PSCAD
0	**0.1140∠-90.00°**	**0.1142∠-90.00°**	**0.0395∠90.00°**	**0.0394∠90.00°**	**0.1535∠90.00°**	**0.1536∠90.00°**	**262.798∠90.00°**	**262.795∠90.00°**
1	**3.0041∠-24.92°**	**3.0048∠-24.92°**	**1.6641∠-138.53°**	**1.6648∠-138.53°**	**2.7908∠121.96°**	**2.1916∠121.96°**	**0.2449∠30.80°**	**0.2449∠30.80°**
-2	**0.4286∠-31.40°**	**0.4287∠-31.41°**	**0.3722∠89.81°**	**0.3722∠89.79°**	**0.3961∠-157.94°**	**0.3962∠-157.93°**	**0.8166∠105.52°**	**0.8166∠105.52°**
3	**0.6628∠65.58°**	**0.6627∠65.56°**	**0.3235∠-3.80°**	**0.3235∠-3.82°**	**0.8336∠-135.74°**	**0.8336∠-135.73°**	**0.1739∠118.38°**	**0.1739∠118.38°**
4	**0.1470∠48.70°**	**0.1471∠48.66°**	**0.1228∠-77.93°**	**0.1228∠-77.98°**	**0.1231∠175.49°**	**0.1231∠175.47°**	**0.0736∠151.05°**	**0.0736∠151.05°**
-5	**1.0617∠92.98°**	**1.0617∠92.95°**	**0.9997∠-138.62°**	**0.9997∠-138.66°**	**0.8990∠-26.41°**	**0.8990∠-26.41°**	**0.0210∠89.77°**	**0.0209∠89.77°**
6	**0.1220∠16.05°**	**0.1219∠16.03°**	**0.0524∠47.83°**	**0.0523∠47.79°**	**0.1688∠-154.58°**	**0.1688∠-154.57°**	**0.2793∠-111.20°**	**0.2793∠-111.20°**
7	**0.5944∠-143.23°**	**0.5943∠-143.26°**	**0.5567∠102.23°**	**0.5567∠102.20°**	**0.6231∠-17.63°**	**0.6231∠-17.62°**	**0.0165∠112.41°**	**0.0165∠112.41°**
-8	**0.1840∠82.39°**	**0.1841∠82.35°**	**0.2141∠-128.08°**	**0.2141∠-128.13°**	**0.1086∠-7.41°**	**0.1086∠-7.41°**	**0.0138∠-115.97°**	**0.0138∠-115.96°**
9	**0.0883∠166.41°**	**0.0882∠166.34°**	**0.0170∠-132.39°**	**0.0169∠-132.42°**	**0.0976∠-4.85°**	**0.0976∠-4.88°**	**0.0203∠-114.84°**	**0.0203∠-114.84°**
10	**0.0739∠138.43°**	**0.0739∠138.36°**	**0.0313∠32.69°**	**0.0313∠32.57°**	**0.0720∠-66.33°**	**0.0721∠-66.35°**	**0.0048∠-114.18°**	**0.0048∠-114.17°**
-11	**0.3060∠-20.41°**	**0.3060∠-20.43°**	**0.3588∠95.62°**	**0.3587∠95.57°**	**0.3550∠-135.22°**	**0.3551∠-135.19°**	**0.0061∠-132.55°**	**0.0061∠-132.55°**
12	**0.0777∠123.78°**	**0.0777∠123.73°**	**0.0462∠-150.94°**	**0.0461∠-151.02°**	**0.0936∠-26.83°**	**0.0936∠-26.85°**	**0.0556∠150.35°**	**0.0556∠150.35°**
13	**0.2497∠142.08°**	**0.2498∠142.03°**	**0.2607∠16.05°**	**0.2608∠15.98°**	**0.2318∠-103.45°**	**0.2318∠-103.44°**	**0.0055∠-146.23°**	**0.0055∠-146.23°**

may experience a low X/R ratio. To show the capability of the proposed model in such situations, another study is conducted on a rectifier with a C filter that is connected to a distribution feeder with an impedance of 5% and X/R ratio of 0.5. The complete set of parameters are given in Appendix C, and the rectifier operates in the CCM. Table 5.5 illustrates the harmonic phasors of the AC-side currents and DC-side voltage obtained from the proposed model and PSCAD/EMTDC time-domain simulations. As can be seen, a very good compliance exists between the results acquired by the proposed model and those given by PSCAD/EMTDC time-domain simulations.

5.10 Discussion

5.10.1 Rectifier's Modes of Operation

In addition to the DCM and CCM demonstrated in Figures 5.2 and 5.3, three-phase diode-bridge rectifiers might work in two other modes [138]. Denoting DCM and CCM as Modes 1 and 2, respectively, the other two modes can be regarded as Modes 3 and 4. Mode 3 includes two intervals: in the first interval, the conduction of two diodes is followed by the conduction of three diodes; and in the second interval, the conduction of two diodes is followed by the conduction of no diode. Mode 4 is based on conduction through a

sequence of three-diode paths. Given that the operating range of Mode 3 is very small, and the operation in Mode 4 is rare, only Modes 1 and 2 are considered here as in [77], [84].

5.10.2 Verifying the Mode of Operation

The verification of each operational mode and the selection of its corresponding boundary conditions can be performed based on the diodes' conduction characteristics of DCM and CCM, which can be seen as follows. At the points of Table 5.1 in which the voltage conditions are defined, i.e., at $t = \gamma_i$, for $i \in \{1, 2, ..., 6\}$, the voltage drop across one diode becomes zero, and that diode starts conduction along with the other diode(s) that have already been exposed to zero voltage. For the DCM, only one diode's voltage has already increased to zero; however, for the CCM, two diodes have already been conducting, and hence, have zero voltage. Thus, the mode of operation can be verified through checking the diodes' voltages at the switching instants.

For example; for the DCM [Figure 5.2], at $t = \gamma_1$, v_{D_1} gets positive while v_{D_6} has already been positive; and for the CCM [Figure 5.3], at $t = \gamma_1$, v_{D_1} becomes positive, though v_{D_5} and v_{D_6} have already been positive; where v_{D_i} is the voltage across D_i. Therefore, v_{D_5} being negative at $t = \gamma_1$ gives the necessary condition for the operation in the DCM. To check whether this condition is met, v_{D_5} must be calculated. Starting with KVL in the loop of phase c [Figure 5.1a], v_{D_5} can be described in terms of the system state variables, their derivatives, and the voltage between the neutrals of the supply and rectifier, v_{Nn}. After some mathematical operations, the relation for v_{D_5} at $t = \gamma_1$ can be simplified to:

$$v_{D_5}(\gamma_1) = \frac{3}{2} v_{cn}(\gamma_1) - \frac{1}{2} v_{dc}(\gamma_1) - \frac{3}{2} L \frac{di_c}{dt}(\gamma_1) - \frac{3}{2} R i_c(\gamma_1) \tag{5.61}$$

At each iteration of the switching instants' calculations, the solution of the state-space model described in Section 5.4 provides the state-space variables and their derivatives at all switching instants, including $t = \gamma_1$, and therefore, all the terms in (5.61) are known, and $v_{D_5}(\gamma_1)$ is obtained.

In addition to $v_{D_5}(\gamma_1)$, the DCM operation needs negative values for $v_{D_6}(\gamma_2)$, $v_{D_1}(\gamma_3)$, $v_{D_2}(\gamma_4)$, $v_{D_3}(\gamma_5)$, and $v_{D_4}(\gamma_6)$. Hence, the necessary and sufficient condition for the operation in DCM can be defined by the constraint:

$$v_{D_{i-2}}(\gamma_i) < 0, \quad \forall i \in \{1, 2, ..., 6\} \tag{5.62}$$

where $v_{D_{1-2}} = v_{D_5}$, $v_{D_{2-2}} = v_{D_6}$, and the equations for $v_{D_{i-2}}(\gamma_i)$ are given in Table 5.6.

Table 5.6: Diodes' Voltages for Mode Verification

Switching Instant	$v_{D_{i-2}}(\gamma_i)$
$t=\gamma_1$	$v_{D_5}=\frac{3}{2}v_{cn}-\frac{1}{2}v_{dc}-\frac{3}{2}L\frac{di_c}{dt}-\frac{3}{2}Ri_c$
$t=\gamma_2$	$v_{D_6}=-\frac{3}{2}v_{bn}-\frac{1}{2}v_{dc}+\frac{3}{2}L\frac{di_b}{dt}+\frac{3}{2}Ri_b$
$t=\gamma_3$	$v_{D_1}=\frac{3}{2}v_{an}-\frac{1}{2}v_{dc}-\frac{3}{2}L\frac{di_a}{dt}-\frac{3}{2}Ri_a$
$t=\gamma_4$	$v_{D_2}=-\frac{3}{2}v_{cn}-\frac{1}{2}v_{dc}+\frac{3}{2}L\frac{di_c}{dt}+\frac{3}{2}Ri_c$
$t=\gamma_5$	$v_{D_3}=\frac{3}{2}v_{bn}-\frac{1}{2}v_{dc}-\frac{3}{2}L\frac{di_b}{dt}-\frac{3}{2}Ri_b$
$t=\gamma_6$	$v_{D_4}=-\frac{3}{2}v_{an}-\frac{1}{2}v_{dc}+\frac{3}{2}L\frac{di_a}{dt}+\frac{3}{2}Ri_a$

Given that the rectifier is operated either in DCM or CCM, not satisfying (5.62) implies the CCM operation.

5.10.3 Accuracy and Numerical Robustness

As explained, the proposed model includes two large resistances; R_{off}, introduced in Section III for a diode in the off mode; and R_{inf}, shown in Figure 5.1b and applied in Section 5.8 for the model extension to the case with LC filter. R_{inf}, as a parallel element, should be selected so that its current be negligible compared to that of its parallel impedance, which is achieved once the following condition is satisfied for all harmonics of interest:

$$R_{\text{inf}} \gg \left| R_{dc} + jh\omega L_{dc} + \frac{R_l}{1+jh\omega C R_l} \right| \tag{5.63}$$

In addition, R_{off}, as a series resistance, should be chosen to be significantly larger than its series impedance for all harmonics of interest, i.e.,

$$R_{off} \gg |R + R_{dc} + j\omega h\,(L + L_{dc})| \tag{5.64}$$

In this chapter, the values of R_{inf} and R_{off} have been taken equal to 10^5 and 10^8 Ω, respectively. As illustrated by Tables 5.2, 5.3, 5.4 and 5.5, these values lead to a three decimal place accuracy.

Furthermore, it is necessary to ensure the selected values for R_{inf} and R_{off} do not cause numerical problems such as singularity or ill-conditioning for the proposed model.

To that aim, the condition numbers, defined in [139], are employed to investigate the matrices whose inverses are used in the proposed model. The condition number of a well-conditioned matrix is 1; however, the condition number is a very large number for ill-conditioned systems, and is infinity for a singular one [139]. If the condition number is 10^a, one may lose up to a digits of accuracy [140]. Moreover, if the condition number exceeds 10^b, where b equals decimal precision of the computational platform used, one can not obtain the solution [141]. In terms of MATLAB computation, the decimal precision is 16 digits [142], and thus, the solution can not be obtained once the condition number is greater than 10^{16}.

The matrices that should be checked are $\mathbf{D}$ in (5.9), and the Jacobian matrix $\mathbf{J}$ given by (5.41). For the rectifier with LC filter operating in the CCM, the condition numbers for $\mathbf{D}$ and $\mathbf{J}$ matrices equal 1.1 and 519.9, respectively. Whereas, for the DCM, the condition numbers for the $\mathbf{D}$ and $\mathbf{J}$ matrices are 1.3 and 12.1, respectively. This confirms that the selected values for R_{inf} and R_{off} do not cause numerical problems.

5.11 Conclusion

This chapter has introduced a time-domain-based method for deriving all the characteristic and non-characteristic harmonics of three-phase diode bridge rectifiers under unbalanced and distorted supply. The proposed modelling has the following advantages: 1) it has a single formulation for both DCM and CCM; 2) the system AC and DC sides get decoupled through introducing R_{inf}, so that the model for a rectifier with a C filter can be readily extended to accommodate any filter structure at the DC side; 3) the harmonics are derived through multiplications of matrices, without any limiting constraint such as the network's X/R ratio. To guarantee a quadratic convergence, an analytical Jacobian matrix has been developed, which has the advantage of a unique formulation irrespective of the rectifier's mode of operation and the filter structure.

Chapter 6

Harmonic Analysis of Droop-based Islanded Microgrids

6.1 Introduction

A microgrid harmonic analysis should be carried out to quantify the distortions in voltage and current waveforms at various system buses. Islanded microgrids have specific features that should be considered in their harmonic analysis. First, microgrids' distributed generators (DGs) are typically droop-based, and accordingly, the steady state frequency is different from the rated one. Second, there is no slack bus, which affects the distribution of fundamental frequency currents, and thus, harmonic currents. Third, DGs usually have voltage source converters (VSC) as an interface for energy transfer to microgrids. The control structures and output filters of the VSCs affect the voltage and current distortions, and hence, they should be considered in the harmonic analysis. This chapter[1] proposes a harmonic power flow algorithm that takes into account these features. The effectiveness of the proposed method for harmonic analysis is confirmed through a comparative evaluation with time-domain simulations.

6.2 Contributions

The main contributions of this chapter are as follows:

[1] A version of this chapter will be submitted to *an IEEE* journal

- A sequential harmonic power flow algorithm is proposed for islanded microgrids.
- The proposed algorithm considers the specific features of isladed microgrids, i.e., the lack of a slack bus and the droop-based operation of DGs.
- The proposed algorithm includes DGs' controllers and filters in the harmonic analysis.
- The algorithm allows the incorporation of accurate models of nonlinear loads, i.e., iterative ones considering the mutual interactions of different harmonics.

6.3 Proposed Algorithm

Figure 6.1 shows the flowchart of the proposed harmonic power flow algorithm. As can be seen, the algorithm is a sequential one that repeats fundamental power flow (F.P.F) and harmonic power flow (H.P.F) algorithms, as two inner loops, in sequence until convergence is achieved. As this is a sequential algorithm, the convergence criteria should be selected from among the calculations that are common in the inner loops. Here, the convergence criteria is the equality of nonlinear loads' fundamental currents, $\tilde{\mathbf{I}}_{\mathbf{1}}^{\mathbf{N.L}}$, given by the fundamental power flow and harmonic power flow algorithms. The fundamental power flow takes into account the specific features of islanded microgrids, i.e., they are formed based on voltage-controlled DGs; there is no slack bus; and the DGs are operated based on droop characteristics. The fundamental power flow model is explained in Section 6.3.1. On the other hand, the harmonic power flow, explained in 6.3.2, is based on Nodal analysis in which the microgrid's nonlinear loads constitute its current source vector, and the rest of elements are modelled within the harmonic admittance matrix, which is calculated at the system operating frequency determined by the fundamental power flow algorithm. The DGs' voltage source converters (VSCs) are modelled through their transfer functions, with which are added to the harmonic bus admittance matrix of microgrids. The employed model for DGs' VSCs is given in Section 6.3.3. The model considered here for the harmonic current source equivalent of a nonlinear load is updated at each iteration, and takes into account the mutual interactions of different harmonics. This model is elaborated in Section 6.3.4.

6.3.1 Fundamental Power Flow

As can be seen in Figure 6.1, the inputs to the fundamental power flow algorithm are the vectors of fundamental active and reactive powers, i.e., $\mathbf{P_1}$ and $\mathbf{Q_1}$, respectively. These

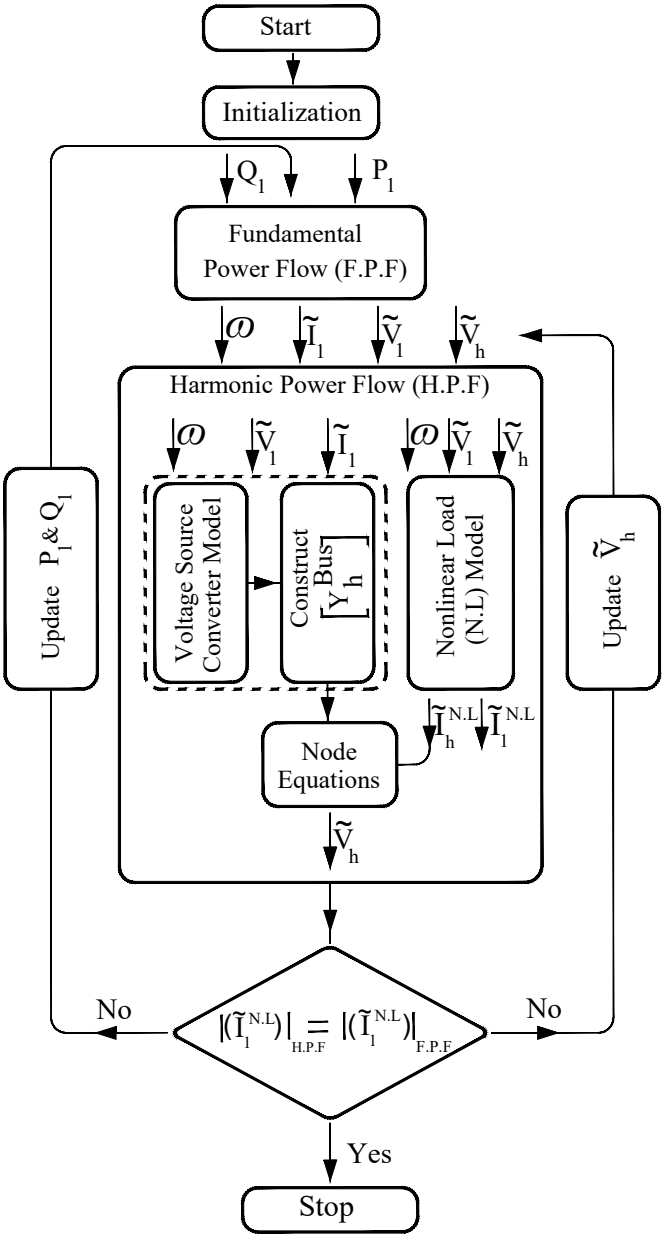

Figure 6.1: Flow chart of the proposed harmonic power flow for islanded microgrids.

data are available for linear loads; however, for nonlinear loads, the fundamental active and reactive power are determined as the output of nonlinear load models, which will be

explained later. The outputs of the fundamental power flow algorithm are the microgrid operating frequency, ω, and vectors including the fundamental voltages and currents of all buses, i.e., $\tilde{\mathbf{V}}_{\mathbf{1}}$ and $\tilde{\mathbf{I}}_{\mathbf{1}}$, respectively.

The model of the fundamental power flow algorithm comprises a set of mismatch equations derived from the balance of powers, i.e., at any bus, the summation of the powers injected by the network, DGs and loads is zero, as

$$P_{b,1}^{I} + P_{b,1}^{DG} - P_{b,1}^{L} = 0, \forall b \in \mathcal{S}^{B} \tag{6.1}$$

$$Q_{b,1}^{I} + Q_{b,1}^{DG} - Q_{b,1}^{L} = 0, \forall b \in \mathcal{S}^{B} \tag{6.2}$$

where $P_{b,1}^{I}$, $P_{b,1}^{DG}$, and $P_{b,1}^{L}$ are the fundamental active power contributions of the network, DG, and load at bus b, respectively; and $Q_{b,1}^{I}$, $Q_{b,1}^{DG}$, $Q_{b,1}^{L}$ are the fundamental reactive power contributions of the network, DG, and load at bus b, respectively, and $\mathcal{S}^{B}$ is a set that includes all microgrid buses. These power terms can be described by

$$P_{b,1}^{I} = \sum_{k=1}^{N^{B}} V_{b,1} V_{k,1} Y_{bk,1} \cos\left(\delta_{b,1} - \delta_{k,1} - \theta_{bk,1}\right), \forall b \in \mathcal{S}^{B} \tag{6.3}$$

$$Q_{b,1}^{I} = \sum_{k=1}^{N^{B}} V_{b,1} V_{k,1} Y_{bk,1} \sin\left(\delta_{b,1} - \delta_{k,1} - \theta_{bk,1}\right), \forall b \in \mathcal{S}^{B} \tag{6.4}$$

$$P_{b,1}^{DG} = \frac{1}{m_{b}^{P}} \left(\omega^{nom} - \omega\right), \forall b \in \mathcal{S}^{B} \tag{6.5}$$

$$Q_{b,1}^{DG} = \frac{1}{m_{b}^{Q}} \left(V^{nom} - V_{b,1}\right), \forall b \in \mathcal{S}^{B} \tag{6.6}$$

$$P_{b,1}^{L} = P_{b}^{L0} {V_{b,1}}^{\alpha} \left(1 + K_{pf}\left(\omega - \omega^{nom}\right)\right), \forall b \in \mathcal{S}^{LB} \tag{6.7}$$

$$Q_{b,1}^{L} = Q_{b}^{L0} {V_{b,1}}^{\beta} \left(1 + K_{qf}\left(V_{b,1} - V^{nom}\right)\right), \forall b \in \mathcal{S}^{LB} \tag{6.8}$$

where ω is the system operating frequency; $V_{b,1}$ and $\delta_{b,1}$ are the magnitude and phase angle of bus b fundamental voltage, respectively; $Y_{bk,1}$ and $\theta_{bk,1}$ are the magnitude and phase angle of the fundamental admittance between bus b and bus k, respectively; ω^{nom} and V^{nom} are the nominal system frequency and voltage, respectively; m_{b}^{P} and m_{b}^{Q} are the slopes of frequency-active power and voltage-reactive power droop characteristics, respectively; P_{b}^{L0} and Q_{b}^{L0} are the nominal values for the active and reactive powers of the load at bus b, respectively; α and β are the load active and reactive power exponents for dependence on voltage, respectively; K_{pf} and K_{qf} are the coefficients for active and reactive power

dependence on frequency, respectively; and $\mathcal{S}^{LB}$ is a set including linear loads' buses.

The solution of the fundamental power flow algorithm is obtained by minimizing the l^2-norm of power flow mismatch equations. For this purpose, a nonlinear least-squares minimization is written as

$$\min_{\mathcal{X}^{PF}} \left\| \mathbf{F}(\mathcal{X}^{PF}) \right\|_2 \tag{6.9}$$

where $\mathbf{F}$ represents power mismatch equations for all buses that are extracted from (6.1) and (6.2); $\mathcal{X}^{\mathbf{PF}}$ is a vector comprising the magnitudes and angles of bus-voltages as well as the network frequency. This optimization problem is solved using a Newton-Trust region method [93]. The power flow solution is sent back to the harmonic power flow algorithm.

6.3.2 Harmonic Power Flow

Given the fundamental power flow outputs, the harmonic bus admittance matrix, including system linear loads, distribution lines and DGs can be constructed at different harmonic orders. Microgrids' linear loads can be regarded as either constant power, constant current or constant impedance. The addition of constant impedance loads to the harmonic admittance matrix is straightforward. For the case of constant power and constant current loads, one can do the following. At each iteration, the fundamental power flow provides the fundamental active and reactive powers of the loads, and accordingly, their admittances can be obtained using (6.10) and (6.11).

$$\tilde{Y}_{b,1} = \frac{P^L_{b,1} - jQ^L_{b,1}}{V^2_{b,1}} \tag{6.10}$$

$$\tilde{Y}_{b,h} = \left(\mathrm{Re}(\tilde{Y}^{-1}_{b,1}) + jh\omega \times \mathrm{Im}(\tilde{Y}^{-1}_{b,1}) \right)^{-1} \tag{6.11}$$

where Re and Im operators return the real and imaginary parts, respectively; $V_{b,1}$ is the voltage magnitude of bus b obtained from the fundamental power flow; and h is the harmonic order.

Merging the distribution lines into the harmonic admittance matrix is also similar to that of the constant impedance load; however, depending on the cross section of the lines, the inclusion of skin effect might be necessary. Eventually, by deriving the transfer functions of DGs, their Thevenin impedances, and thus, their admittances are acquired and added to the harmonic bus admittance matrix. Having the harmonic bus admittance matrix, $\tilde{\mathbf{Y}}^{\mathbf{Bus}}_{\mathbf{h}}$, and the harmonic current source equivalent of nonlinear loads, $\tilde{\mathbf{I}}_{\mathbf{h}}$, one can

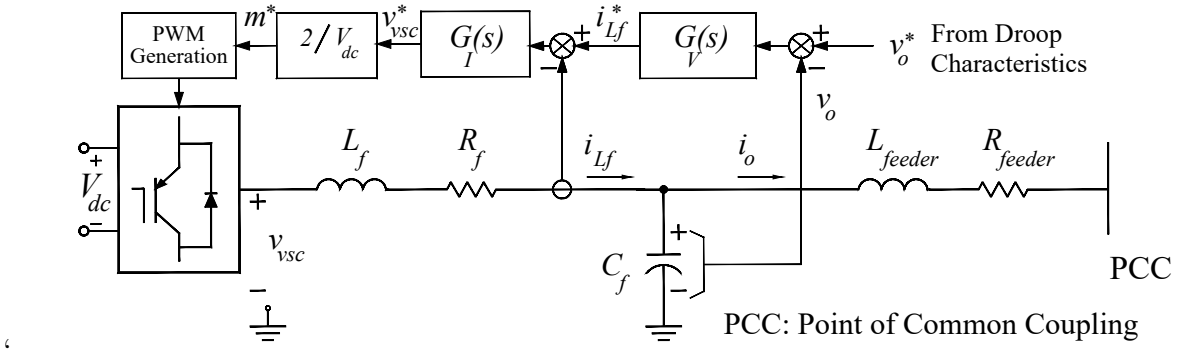

Figure 6.2: DGs' control structure.

use nodal analysis and obtain microgrid bus harmonic voltages as

$$\tilde{\mathbf{V}}_{\mathbf{h}} = \left(\tilde{\mathbf{Y}}_{\mathbf{h}}^{\mathbf{Bus}}\right)^{-\mathbf{1}} \tilde{\mathbf{I}}_{\mathbf{h}} \tag{6.12}$$

6.3.3 Harmonic Modeling of DGs' VSCs

According to the explanations given in Section 2.3.3, which are mainly based on the typical switching frequencies of microgrids, this chapter uses the transfer function approach for the harmonic modelling of DGs' VSCs. Using this approach, the Thevenin impedances of DGs' VSCs are derived and added to the harmonic bus admittance matrix at different harmonic orders. Given that islanded microgrids are formed based on voltage-controlled DGs, the derivation is performed here for voltage control DGs; however, a similar procedure can be applied in the case of current-controlled DGs to obtain their Norton equivalents.

Figure 6.2 illustrates the control structure of a voltage-controlled DG. As can be seen, the voltage is controlled in the outer-most loop, and the control structure is a cascade one with an inner current loop. It is worth noting that voltage-controlled DGs can also be seen without the inner current loop [12]. The voltage reference is given by frequency-active power and voltage reactive power droop characteristics, which are not shown here. The derivation of the model can be started by the LC interfacing filter that is governed by

$$L_f \frac{di_{Lf}}{dt} + R_f i_{Lf} = v_{vsc} - v_o \tag{6.13}$$

$$C_f \frac{dv_o}{dt} = i_{Lf} - i_o \tag{6.14}$$

where v_o and v_{vsc} are the voltages of the LC filter and VSC, respectively; i_{Lf} is the current of the filter inductor; and i_o is the DG line current. By mapping (6.13) and (6.14) into the Laplace domain and combining the model equations to eliminate i_{Lf}, one can obtain

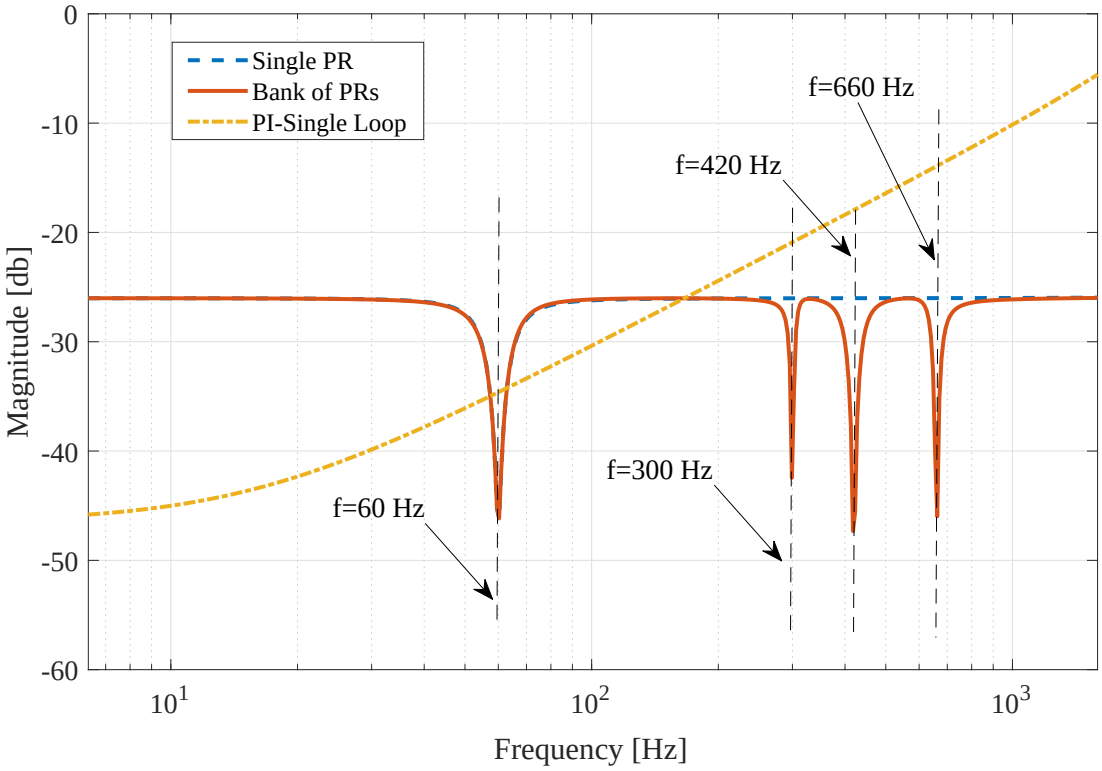

Figure 6.3: DGs' Thevenin impedance.

$$\left(L_f C_f s^2 + R_f C_f s + 1\right) V_o = V_{vsc} - (L_f s + R_f) I_o \tag{6.15}$$

On the other hand, V_{vsc} is equal to V^*_{vsc}, which can be acquired from the control loops' relations, (6.16) and (6.17), by substituting I^*_{Lf} in (6.16) from (6.17).

$$V^*_{vsc} = \left(I^*_{Lf} - I_{Lf}\right) G_I \tag{6.16}$$

$$I^*_{Lf} = \left(V^*_o - V_o\right) G_V \tag{6.17}$$

where V^*_o and I^*_{lf} are the references for the voltage and current loops, respectively; and

G_V and G_I are the controllers' transfer functions for the voltage and current loops, respectively. After some manipulations, the Thevenin model of the voltage-controlled DG can be furnished as

$$V_o = GV^* - Z_{th} I_o \tag{6.18}$$

where

$$Z_{th} = \frac{R_f + sL_f + G_I}{L_f C_f s^2 + C_f \left(R_f + G_I\right) s + 1 + G_V G_I} \tag{6.19}$$

The controller of the inner current loop can be a proportional controller since the accuracy is not a major concern for this loop. The voltage controller is usually selected among the following: a proportional-resonant (PR) controller at the fundamental frequency [12], a bank of PR controllers at the fundamental and harmonic frequencies [16], or a proportional-integral (PI) controller [86], to accurately follow the voltage command. Adaptive PR controllers have also been proposed in the literature in order to deal with frequency variations from the nominal value, as this happens in islanded microgrids [106].

Figure 6.3 shows a DG Thevenin impedance for three different controllers in the voltage loop, i.e., a PR controller, bank of PR controllers, and PI controller without the inner current loop. As can be seen, different controllers represent different impedances at harmonic frequencies, which might not be negligible. Although the Thevenin impedance for the case with a bank of PR controller is almost negligible, one can expect a different situation when applying the other two controllers shown in Figure 6.3. As a concluding remark, the DGs' equivalent impedances at harmonic frequencies depend on their control structures and filter parameters. These impedances can be obtained using the described transfer function approach and are embedded into the propose harmonic power flow algorithm.

6.3.4 Harmonic Modelling of Nonlinear Loads

VSC-interfaced DGs, as the microgrids' nonlinear generators, are not regarded as the main source of harmonic distortion due to their high switching frequencies and output filters, and accordingly, the main harmonic distortion is assigned to microgrids' nonlinear loads. Among nonlinear loads, three-phase power electronic devices, because of their ratings, have a major role in the harmonic generation. The other nonlinear loads such as PCs, TVs, compact fluorescent lamps, and battery chargers are single-phase loads, and their harmonic modeling is usually performed through statistical and probabilistic methods [143, 144]. These methods are beyond the scope of this thesis, and accordingly, this thesis considers three-phase power electronic devices. Two types of commonly used converters applied at the front end of three-phase electronic devices are thyristor-based (controlled) and diode-

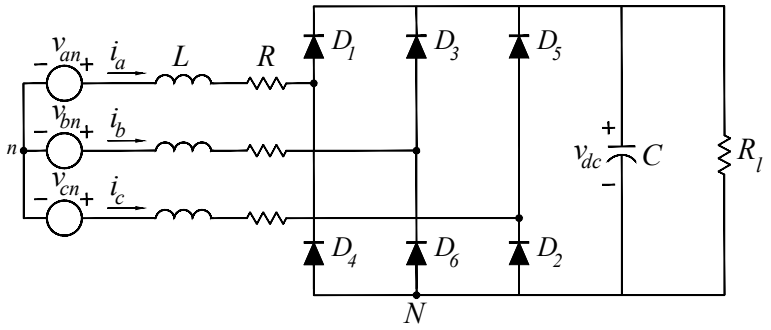

Figure 6.4: Three-phase diode bridge rectifier circuit.

based (uncontrolled) rectifiers. The former is usually used in DC and current-source AC drives, while the latter is normally seen in PWM-based AC drives and DC/DC converters.

This thesis concentrates on diode bridge rectifiers as the microgrids' dominant nonlinear loads for the following reasons. The advances in power electronics have made the application of AC drives more common than that of the DC drives. Further, the main applications for current-source AC drives are at the ratings of around several hundred horsepower [69, 145], and thus, these drives can be hardly seen in microgrids. Moreover, the current source equivalent of thyristor bridge rectifiers can be incorporated in a similar way to the proposed harmonic power flow algorithm.

The harmonic analysis of three-phase diode bridge rectifiers is conducted in accordance with the model already presented in Chapter 5. On the other hand, this chapter considers balanced three-phase microgrids, and accordingly, the symmetry in current waveforms can be exploited to simplify the model proposed in Chapter 5. In this section, the changes that are required to the model of Chapter 5 are explained. Figure 6.4 shows the circuit of a three-phase diode bridge rectifier considered as the nonlinear load in the proposed harmonic power flow algorithm. As can be seen, the circuit includes an L type filter at the AC side, a C filter at the DC side, and a resistor that represents the inverter of a variable speed drive or a DC/DC converter. The supply voltage magnitude and phase angle are known at each iteration of the harmonic power flow algorithm, and thus, they are inputs to the model.

Three phase diode bridge rectifiers are mainly operated in discontinuous [Figure 5.2] and continuous [Figure 5.3] conduction modes. For both modes, there are twelve switching instants within a period, and therefore, the current waveforms are divided into twelve time segments. The first step in the harmonic analysis is to acquire these switching instants. The current waveforms of balanced three-phase systems include a sixth period symmetry

[77], and thus, the switching instants can be obtained once one pair of (γ_i, η_i), where $i \in \{1, 2, ..., 6\}$ are calculated. The state-space model for rectifiers in balanced systems can be written as

$$\dot{\mathbf{X}} = \mathbf{A_{on,i}} \mathbf{X} \qquad \gamma_i \leq t \leq \gamma_i + \eta_i \tag{6.20}$$

$$\dot{\mathbf{X}} = \mathbf{A_{off,i}} \mathbf{X} \qquad \gamma_i + \eta_i \leq t \leq \gamma_{i+1} \tag{6.21}$$

where $\mathbf{A_{on,i}}$ and $\mathbf{A_{off,i}}$ are state transition matrices, and their details can be found in Section 5.5; $i \in \{1, 2, ..., 6\}$; $\gamma_{i+1} = \gamma_i + \frac{T}{6}$ and $\eta_{i+1} = \eta_i$; $\mathbf{X}$ is the state-space vector; the state-space vector includes circuit state variables and supply state variables, as $\mathbf{X} = \begin{bmatrix} \mathbf{X_{cir}}^{\mathbb{T}} & \mathbf{X_{sup}}^{\mathbb{T}} \end{bmatrix}^{\mathbb{T}}$. The circuit state variables are the currents at the AC side, and the voltage at the DC side, i.e., $\mathbf{X_{cir}} = \begin{bmatrix} i_a & i_b & i_c & v_{dc} \end{bmatrix}^{\mathbb{T}}$. The supply state variables comprise the α and β components of the supply voltage harmonics, i.e., $\mathbf{X_{sup}} = \begin{bmatrix} v_{\alpha,1} & v_{\beta,1} & ... & v_{\alpha,h} & v_{\beta,h} & ... \end{bmatrix}^{\mathbb{T}}$. The length of $\mathbf{X_{sup}}$ is $2n_h$, where n_h denotes the number of supply harmonics. The ellipsis "..." in vectors and matrices stands for their extension for all harmonics.

The switching instants are acquired by applying the system boundary conditions [Table 5.1] defined on the system model. Here, only points 1 and 7 of Table 5.1, i.e., the voltage condition at $t = \gamma_1$ and current condition at $t = \gamma_1 + \eta_1$, respectively, are needed, given that there are only two independent switching instants. The system model is developed by obtaining the relation between the state variables at two switching instants, i.e., $t = \gamma_1$ and $t = \gamma_1 + \frac{T}{6}$, through two approaches. The first approach relies on the continuity property of the state variables. Using this property, and combining the solutions of the state-space equations, (6.20) and (6.21), at the two time segments located in the interval $\gamma_1 \leq t \leq \gamma_1 + \frac{T}{6}$, one can write:

$$\mathbf{X}\left(\gamma_1 + \frac{T}{6}\right) = \mathbf{\Phi_1} \mathbf{X}\left(\gamma_1\right) \tag{6.22}$$

where $\mathbf{\Phi_1}$ is a square matrix of size $4 + 2n_h$, and is given by

$$\mathbf{\Phi_1} = e^{\mathbf{A_{off,1}}\left(\frac{T}{6} - \eta_1\right)} e^{\mathbf{A_{on,1}}(\eta_1)} \tag{6.23}$$

The second approach uses the sixth period symmetry as

$$\mathbf{X}\left(\gamma_1 + \frac{T}{6}\right) = \mathbf{\Phi_2} \mathbf{X}\left(\gamma_1\right) \tag{6.24}$$

where

$$\mathbf{\Phi_2} = diag\left(\mathbf{I_4}, \mathbf{\Phi_s}\right) \tag{6.25}$$

$$\mathbf{\Phi_s} = diag\left(\mathbf{\Theta_6}, ..., \mathbf{\Theta_6}, ...\right) \tag{6.26}$$

$$\mathbf{\Theta_6} = \begin{bmatrix} \cos\left(\frac{\pi}{3}\right) & -\sin\left(\frac{\pi}{3}\right) \\ \sin\left(\frac{\pi}{3}\right) & \cos\left(\frac{\pi}{3}\right) \end{bmatrix} \tag{6.27}$$

and $\mathbf{I_4}$ is the identity matrix of size 4. From (6.22) and (6.24), one gets

$$\left(\mathbf{\Phi_1} - \mathbf{\Phi_2}\right)\mathbf{X}\left(\gamma_1\right) = \mathbf{0} \tag{6.28}$$

The non-trivial solution of the homogeneous equation (6.28) is obtained in the same way as already performed in (5.9)–(5.13), with which $\mathbf{X_{cir}}(\gamma_1)$ and $\mathbf{X_{sup}}\left(\gamma_1\right)$ are acquired. Having $\mathbf{X}\left(\gamma_1\right)$, the system state variables at $t = \gamma_1 + \eta_1$ are obtained using (6.29):

$$\mathbf{X}\left(\gamma_1+\eta_1\right) = e^{\mathbf{A_{on,i}}(\eta_1)}\mathbf{X}\left(\gamma_1\right) \tag{6.29}$$

By obtaining $\mathbf{X}(\gamma_1)$ and $\mathbf{X}(\gamma_1+\eta_1)$, the system model is obtained, and one needs to apply the boundary conditions to furnish the mismatch equations giving the switching instants. Two row vectors, $\mathbf{C_{f,1}}$ and $\mathbf{C_{g,1}}$, as explained in Section 5.6.1, can be used to describe the boundary conditions, and thus, the mismatch equations can be written as

$$f_1 = \mathbf{C_{f,1}}\mathbf{X}\left(\gamma_1\right) \tag{6.30}$$

$$g_1 = \mathbf{C_{g,1}}\mathbf{X}\left(\gamma_1 + \eta_1\right) \tag{6.31}$$

The solution of (6.30) and (6.31), using the Newton method, returns the switching instants γ_1 and $\gamma_1 + \eta_1$.

Once the switching instants are obtained, the steady-state harmonics of the circuit state variables can be acquired by augmenting the system state-space model with a differential equation, for each harmonic of interest. As explained in Section 5.7, the solution of the augmented state space model gives the harmonic phasors. The solution of the augmented state-space model has been derived in Section 5.7 based on the analogy with the system state-space model. In the case of balanced systems, it should be underlined that the sixth period symmetry already exploited for the calculation of switching instants cannot be used for the calculation of harmonic phasors. However, the half-wave symmetry is applicable for balanced systems, and accordingly, the calculations of harmonics can be performed based on the solution of the augmented state-space vector over half a period. Considering the augmented state-space vector as $\tilde{\mathbf{X}} = \left[\ \mathbf{X_{cir}}^{\mathbb{T}}\ \ \mathbf{X_{sup}}^{\mathbb{T}}\ \ \mathbf{X_{har}}^{\mathbb{T}}\ \right]^{\mathbb{T}}$, where $\mathbf{X_{har}}$ consists of the harmonics of circuit state variables, the augmented state-space model can be built.

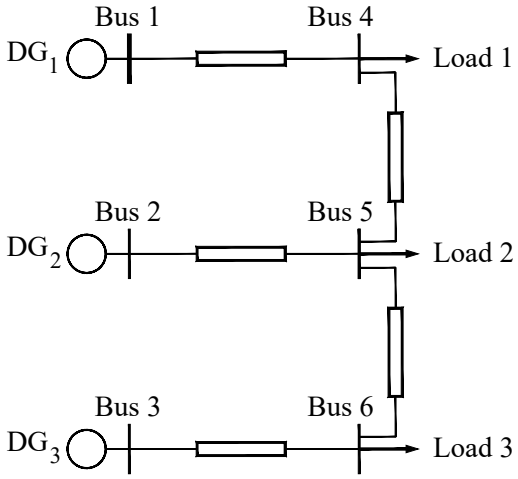

Figure 6.5: Test microgrid.

The solution of the augmented state space model can be written as

$$\tilde{\mathbf{X}}\left(\gamma_1 + \frac{T}{2}\right) = \tilde{\mathbf{\Phi}}\tilde{\mathbf{X}}\left(\gamma_1\right) \tag{6.32}$$

where $\tilde{\mathbf{\Phi}}$ is obtained using (6.33):

$$\tilde{\mathbf{\Phi}} = \prod_{i=1}^{3} e^{\tilde{\mathbf{A}}_{\mathbf{off},\mathbf{i}}(\gamma_{i+1}-\gamma_i-\eta_i)} e^{\tilde{\mathbf{A}}_{\mathbf{on},\mathbf{i}}(\eta_i)} \tag{6.33}$$

where $\tilde{\mathbf{A}}_{\mathbf{on,i}}$ and $\tilde{\mathbf{A}}_{\mathbf{off,i}}$ are state transition matrices already described in Section 5.7. $\tilde{\mathbf{X}}_{\mathbf{har}}\left(\gamma_1 + \frac{T}{2}\right)$ returns all harmonics of interest for circuit state variables.

6.4 Simulation Results

An study is conducted in this section to validate the effectiveness of the proposed harmonic power flow algorithm. The test microgrid is illustrated in Figure 6.5, which includes three identical 20 kVA voltage-controlled DGs, with cascade power, voltage and current controllers, similar to the one shown in Figure 6.2. The switching frequencies of the DGs' VSCs are set to 10 kHz. An adaptive proportional-resonant controller has been considered for the voltage loop, and a proportional controller is used for the inner current loop. In the

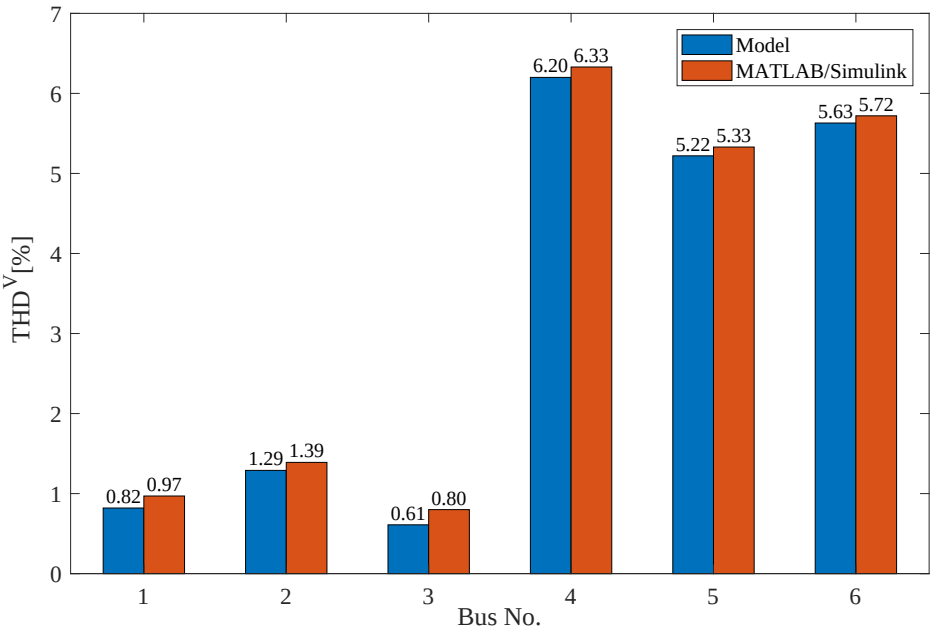

Figure 6.6: Voltage THDs.

harmonic power flow, for voltages and currents, harmonics up to the 29th order are taken into consideration. A mix of linear and nonlinear loads are assumed, with nonlinear loads constituting 43% of the microgrid's demand. System parameters are given in Appendix D.

In this study, two nonlinear loads are assumed, one at Buses 4 and the other at Bus 6, and a linear load is considered at Bus 2. The linear load is of constant impedance type, and the nonlinear loads are three-phase diode bridge rectifiers [Figure 6.4] working in the continuous conduction mode. Thus, the microgrid includes five nonlinear elements. Figure 6.6 shows the total harmonic distortion (THD) of bus voltages obtained from the proposed harmonic power flow algorithm and time-domain simulations in MATLAB/Simulink. As can be seen, there is a good compliance between the voltage THDs acquired using the proposed harmonic power flow algorithm and those given by MATLAB/Simulink. The maximum discrepancy in the voltage THDs is 0.19% and is observed at Bus 3, which is a generating bus. The error can be assigned to the following: 1) ignoring the switching harmonics and 2) the number of harmonics considered in the harmonic analysis of nonlinear loads. Form the results shown in Figure 6.6, one might conclude the discrepancy in voltage THDs caused by ignoring the switching harmonics is more severe at the buses close to DGs.

The results for fundamental active and reactive powers are illustrated in Table 6.1. The maximum percentage errors for active and reactive powers are 1.39% and 2.61%, respectively, which are quite acceptable. In terms of the microgrid' s frequency, the proposed harmonic power flow gives 0.9937 p.u., which is very close to the 0.9938 p.u. obtained from MATLAB/Simulink. In order to evaluate the capability of the proposed harmonic power flow algorithm in the calculation of each individual harmonics, loads' harmonic currents are also investigated. Table 6.2 illustrates loads' harmonic currents acquired by the proposed algorithm and MATLAB/Simulink. As can be seen, the algorithm shows a good performance. For example, the percentage errors for the dominant harmonics of load 1, i.e., the 5th and 7th harmonics, are 0.69% and 1.53%, respectively.

Table 6.1: Fundamental Active and Reactive Powers (60 kVA as the base).

	P1 [p.u.]			**Q1 [p.u.]**		
	H.P.F	**Simulink**	**Error, %**	**H.P.F**	**Simulink**	**Error, %**
Bus 1	0.355	0.353	0.63	0.115	0.115	0.22
Bus 2	0.355	0.353	0.61	0.148	0.147	0.39
Bus 3	0.355	0.353	0.64	0.090	0.089	0.45
Bus 4	0.224	0.221	1.25	0.067	0.069	2.61
Bus 5	0.587	0.585	0.28	0.090	0.089	1.02
Bus 6	0.226	0.222	1.39	0.066	0.068	2.41

Table 6.2: Loads' Harmonic Currents.

	$I_{Load\ 1}$(A,peak)		$I_{Load\ 2}$(A,peak)		$I_{Load\ 3}$(A,peak)	
Load Type	**Nonlinear**		**Linear**		**Nonlinear**	
Harmonic Order	**H.P.F**	**Simulink**	**H.P.F**	**Simulink**	**H.P.F**	**Simulink**
1	56.86	56.72	145.86	145.50	57.09	56.99
5	13.11	13.02	5.30	5.18	13.61	13.54
7	3.85	3.91	1.69	1.64	3.71	3.79
11	1.85	1.79	0.94	0.96	1.97	1.91
13	1.51	1.45	0.76	0.81	1.55	1.50
17	0.71	0.67	0.36	0.33	0.69	0.65
19	0.53	0.54	0.28	0.25	0.55	0.55
23	0.45	0.43	0.22	0.19	0.46	0.44
25	0.38	0.36	0.19	0.19	0.37	0.36
29	0.22	0.20	0.11	0.13	0.22	0.21

6.5 Conclusion

This chapter has proposed a sequential harmonic power flow algorithm for droop-based islanded microgrids. The algorithm repeats fundamental power flow and harmonic power flow algorithms in sequence until the convergence is achieved. The convergence criterion has been defined based on the equality of the common calculations of the two algorithms, i.e., the fundamental components of nonlinear loads' currents. The proposed harmonic power flow algorithm considers the specific features of islanded microgrids, i.e., the droop-based operation of DGs, the lack of a slack bus, and the presence of voltage-controlled DGs. The algorithm also allows the combination of nonlinear loads' accurate models and DGs' complicated controllers. Comparative studies with time-domain simulations in MATLAB/Simulink validated the effectiveness of the proposed harmonic power flow algorithm.

Chapter 7

Summary, Contributions and Directions for Future Works

7.1 Summary

The main goal of this thesis was to improve power quality for microgrids penetrated with nonlinear loads at two levels; at the device level, in the control of distributed generators (DGs); and at the system level, in the planning of microgrids. Additionally, because modelling is the core of power quality studies, this dissertation also considered modelling at two levels; at the device level, in the modelling of nonlinear loads and generators that are common to microgrids; and at the system level, in developing a harmonic power flow algorithm for islanded microgrids. Accordingly, this thesis identified and studied four research points on the planning, control and modelling of microgrids for power quality assurance. A detailed summary of the main studies conducted in this thesis is given in what follows.

There is always a trade-off between accuracy and voltage quality in sharing of nonlinear loads among different DGs. To achieve a better trade-off, Chapter 3 proposed a family of droop characteristics in terms of harmonic conductance versus harmonic current, i.e., one droop characteristic for each harmonic. As a consequence of assigning a variable conductance for each harmonic current, the DGs' controllability is improved, and therefore, the error of nonlinear load sharing is reduced. This chapter also formulated the problem of nonlinear load sharing, and generated the worst case scenario. To deal with the unknown nature of microgrid nonlinear loads, this chapter introduced a method based on the upper limits of load harmonic content.

In addition, this chapter proposed a tuning methodology to optimally adjust the droop characteristics while complying with international standards for the whole operational range. Further, to accurately track the DGs' harmonic conductances designated by the proposed droop characteristics, a hybrid controller of voltage and current is propounded. The proposed algorithm is capable of accurately distributing common nonlinear loads among DGs, and also compensate the local nonlinear loads by their dedicated DGs. The effectiveness of the proposed control strategy has been assured through a comprehensive performance evaluation. To validate the controller effectiveness in shaping DGs' harmonic conductances, the DGs' Thevenin model was derived. Moreover, comparative evaluations proved that the proposed droop-based approach can offer an accurate nonlinear load sharing as well as enhanced voltage profile.

Chapter 4 proposed a comprehensive planning procedure for isolated microgrids penetrated with nonlinear loads. The proposed microgrid planning approach simultaneously determined the sizes, locations and types of DGs and shunt capacitor banks (CBs), while taking into consideration the specific feature of isolated microgrids in the formulation of the planning problem as well as in power flow and reliability constraints.

For the planning formulation, DGs' ratings, and not their active and reactive powers, were directly selected as the optimization variables, and hereupon the DGs' droop slopes merged into the formulation. Merging the droop characteristics into the formulation allowed considering the following in the planning: 1) the impacts of droop-based operation on the flow of active and reactive powers as well as the voltage profile; 2) the error in reactive power sharing, which is a function of DGs' location and their feeder impedances, and 3) the impact of frequency drop caused by the droop-based operation and fundamental power flow on the flow of harmonics. Considering isolated microgrids' features in reliability constraints is as follows. Isolated microgrids require voltage and frequency support during the normal operation, and in particular, following a contingency to build successful islands. Accordingly, the proposed planning approach took into account reliability. Unlike previous approaches, the proposed method does not rely only on supply adequacy, and propounds the fact that the voltage provision requirement can only be accomplished through dispatchable DGs. This method resulted in an effective distribution of dispatchable DGs throughout the microgrid, and thus, allowed building successful islands following a contingency.

The proposed planning algorithm also considered the possibility of resonance or quasi-resonance that might be caused by wind turbines in the presence of nonlinear loads and capacitors. To that aim, a methodology was presented to incorporate wind turbines into the harmonic analysis. A probabilistic approach was used to model the intermittency in loads and renewable DGs. The effectiveness of the proposed planning platform was validated

using the PG&E 69-bus system, and the following were observed: 1) the significance of applying suitable fundamental-power-flow and harmonic-power-flow algorithms for isolated microgrids, and 2) the possibility of avoiding a severe voltage distortion by utilizing an appropriate planning method and only small increase in the cost.

Chapter 5 introduced a time domain-based model for obtaining all the characteristic and non-characteristic harmonics of three-phase diode bridge rectifiers. The model is initially derived in the state-space domain. The most comprehensive situation were considered for the supply, i.e., an unbalanced and distorted supply that includes even harmonics, and accordingly, there is no symmetry in the waveforms of a rectifiers' line currents to be exploited. Thus, the state-space equations were derived for a complete period. There are twelve switching instants within a period, and accordingly, twelve sets of state space equations were obtained and combined together in order to build a rectifier model. The model was then used to acquire the switching instants, using the Newton method. To achieve a quadratic convergence, an analytical Jacobian matrix was developed and used in the iterative process.

The Jacobian matrix has the advantage of being unique for the continuous and discontinuous conduction modes of three-phase diode bridge rectifiers. The harmonics were acquired by augmenting the state-space model with a fictitious differential equation for each harmonic of interest. The solution of the augmented state-space equations gives the harmonics, which includes just multiplications of matrices and no integration. The advantages of this harmonic analysis method are as follows. First, the calculation of each harmonic is independent of the calculation of any other harmonics considered in the formulation. Second, the harmonics of both continuous and discontinuous conduction modes are acquired through a single formulation. Third, the harmonic analysis does not rely on any limiting constraints such as the network's X/R ratio. Lastly, by introducing a virtual large resistance on the rectifier's DC side, the system AC and DC sides became decoupled, and the model initially derived for C filters was extended to accommodate other DC-side filters, including LC filters and two stage LC filters. In order to confirm the effectiveness of the proposed model for harmonic analysis, a comparative evaluation with time-domain simulations was used.

Eventually, Chapter 6 proposed a sequential harmonic power flow algorithm for islanded microgrids. The algorithm took into consideration the droop-based operation of islanded microgrids, the lack of a slack bus, and the presence of voltage-controlled DGs. Further, the algorithm allowed the integration of accurate models for nonlinear loads, such as the one proposed in Chapter 5. The DGs' controllers were modelled through their transfer functions, given the typical range of microgrids' switching frequencies. Thanks to the flexibility of the transfer function method, sophisticated control structures with several

cascade controllers could be readily embedded into the harmonic power flow algorithm. The effectiveness of the proposed method was validated through comparative studies with time domain-based simulations in MATLAB/Simulink.

7.2 Contributions

The main contributions of the research presented in this thesis can be summarized as follows:

1. This thesis proposed a decentralized control scheme to improve nonlinear load sharing and power quality. A family of droop characteristics in terms of harmonic conductance versus harmonic current ($G_h - I_h$) is presented, i.e., a droop characteristic for each harmonic, to shape the DGs' harmonic impedances. There is always a trade-off between sharing accuracy and voltage quality; however, the flexible structure of the proposed method offers a better trade-off compared to other techniques in the literature. A mathematical formulation has been proposed for the problem of nonlinear load sharing, which determines the maximum nonlinear load sharing error and the minimum DG spare power. This thesis also presented a tuning methodology that optimally adjusts the droop characteristics. The proposed method also estimates the maximum harmonic current limits, and accordingly, ensures the system voltage quality complies with international standards.

2. This thesis presented a planning algorithm for isolated microgrids penetrated with nonlinear loads to simultaneously determine the locations, sizes and types of DGs and CBs. The main contributions of the proposed planning algorithm are as follows. For the first time, the specific features of isolated microgrids in fundamental and harmonic power flow algorithms have been considered in the planning. Further, by modelling the wind turbine in the harmonic power flow algorithm, the possibility of resonance that might happen because of the presence of nonlinear loads, capacitors, and wind turbines is taken into consideration. Moreover, given that isolated microgrids require the provision of voltage and frequency support, a reliability based method has been proposed to effectively distribute dispatchable DGs throughout the microgrids and to build successful islands following a contingency.

3. This thesis presented a model for the harmonic analysis of three-phase diode bridge rectifiers. The main contributions of this work are as follows. A state-space-based

model is developed that allows obtaining all steady-state characteristic and non-characteristic harmonics of three-phase diode bridge rectifiers, under distorted and unbalanced supply. The model is independent of the network's X/R ratio. An analytical Jacobian matrix is derived to accelerate convergence. In this derivation, the system model has been arranged so as to avoid the appearance of any terms requiring the integration of a matrix exponential. Through introducing a high resistance at the DC side, the AC and DC sides of the rectifier are decoupled, allowing the model extension for any DC-side filter.

4. This thesis proposed an accurate sequential harmonic power flow algorithm for islanded microgrids that has the following unique features. First, the algorithm takes into account the fact that there is no slack bus and the droop-based operation of DGs. Second, the algorithm considers DGs' controllers and filters in the harmonic analysis of islanded microgrids. Third, the algorithm allows incorporating the accurate models of nonlinear loads, i.e., iterative ones considering the mutual interactions of different harmonics, in the harmonic analysis.

7.3 Directions for Future Works

Based on the results presented in this thesis, the following subjects are suggested for future works:

1. Developing a supervisory centralized controller with minimal communication requirements for accurate sharing of non-fundamental power and power quality improvement based on harmonic power flow. Cascade controllers of voltage and current can be used at each DG to implement the virtual harmonic resistances, whose values are determined through an optimization model similar to the one proposed in Chapter 3.

2. Developing a planning platform for isolated microgrids to simultaneously site and size distributed generators, energy storages, and shunt capacitors in isolated microgrids with nonlinear loads considering power quality and reliability constraints. This requires to include the following in the planning algorithm proposed in Chapter 4: 1) a probabilistic wind-generation and load model derived on an hourly basis, 2) a suitable droop characteristic for energy storages along with their power and energy equality and inequality constraints, and 3) a model for harmonic analysis of energy storages.

3. Developing a model for harmonic analysis of twelve-pulse diode bridge rectifiers under unbalanced and distorted supply and deriving its analytical Jacobian matrix to ensure a quadratic convergence. A state-space model similar to the one proposed in Chapter 5 can be developed to first derive the switching instants using the Newton method and developed Jacobian matrix, and then, to obtain steady state harmonics by augmenting the set of equations with a fictitious differential equation for each harmonic of interest

4. Investigating the capability of the proposed sequential harmonic power flow algorithm in Chapter 6 for line commutated converters and twelve-pulse diode bridge rectifiers in unbalanced islanded microgrids. This investigation relies on already obtained models for current source equivalents of line commutated converters and twelve-pulse diode bridge rectifiers that are updated at each iteration of the harmonic power flow algorithm.

References

[1] J. Rocabert, A. Luna, F. Blaabjerg, and P. Rodriguez, "Control of power converters in ac microgrids," *IEEE Transactions on Power Electronics*, vol. 27, no. 11, pp. 4734–4749, 2012.

[2] J. He and Y. W. Li, "Hybrid voltage and current control approach for dg-grid interfacing converters with lcl filters," *IEEE Transactions on Industrial Electronics*, vol. 60, no. 5, pp. 1797–1809, 2013.

[3] T. Vandoorn, J. De Kooning, B. Meersman, and L. Vandevelde, "Review of primary control strategies for islanded microgrids with power-electronic interfaces," *Renewable and Sustainable Energy Reviews*, vol. 19, pp. 613–628, 2013.

[4] K. Siri, C. Lee, and T.-E. Wu, "Current distribution control for parallel connected converters. i," *IEEE Transactions on Aerospace and Electronic Systems*, vol. 28, no. 3, pp. 829–840, 1992.

[5] T. Caldognetto and P. Tenti, "Microgrids operation based on master–slave cooperative control," *IEEE Journal of Emerging and Selected Topics in Power Electronics*, vol. 2, no. 4, pp. 1081–1088, 2014.

[6] M. Mahmud, M. Hossain, H. Pota, and A. Oo, "Robust nonlinear distributed controller design for active and reactive power sharing in islanded microgrids," *IEEE Transactions on Energy Conversion*, vol. 29, no. 4, pp. 893–903, 2014.

[7] H. Han, X. Hou, J. Yang, J. Wu, M. Su, and J. M. Guerrero, "Review of power sharing control strategies for islanding operation of ac microgrids," *IEEE Transactions on Smart Grid*, vol. 7, no. 1, pp. 200–215, 2016.

[8] Y. A.-R. I. Mohamed and E. F. El-Saadany, "Adaptive decentralized droop controller to preserve power sharing stability of paralleled inverters in distributed generation

microgrids," *IEEE Transactions on Power Electronics*, vol. 23, no. 6, pp. 2806–2816, 2008.

[9] Q.-C. Zhong, "Harmonic droop controller to reduce the voltage harmonics of inverters," *IEEE Transactions on Industrial Electronics*, vol. 60, no. 3, pp. 936–945, 2013.

[10] M. M. Hashempour, M. Savaghebi, J. C. Vasquez, and J. M. Guerrero, "A control architecture to coordinate distributed generators and active power filters coexisting in a microgrid," *IEEE Transactions on Smart Grid*, vol. 7, no. 5, pp. 2325–2336, 2016.

[11] M. S. Munir, Y. W. Li, and H. Tian, "Improved residential distribution system harmonic compensation scheme using power electronics interfaced dgs," *IEEE Transactions on Smart Grid*, vol. 7, no. 3, pp. 1191–1203, 2016.

[12] Y. W. Li, "Control and resonance damping of voltage-source and current-source converters with *lc* filters," *IEEE Transactions on Industrial Electronics*, vol. 56, no. 5, pp. 1511–1521, 2009.

[13] J. He, Y. W. Li, and F. Blaabjerg, "Flexible microgrid power quality enhancement using adaptive hybrid voltage and current controller," *IEEE Transactions on Industrial Electronics*, vol. 61, no. 6, pp. 2784–2794, 2014.

[14] M. Savaghebi, A. Jalilian, J. C. Vasquez, and J. M. Guerrero, "Secondary control for voltage quality enhancement in microgrids," *IEEE Transactions on Smart Grid*, vol. 3, no. 4, pp. 1893–1902, 2012.

[15] T.-L. Lee and P.-T. Cheng, "Design of a new cooperative harmonic filtering strategy for distributed generation interface converters in an islanding network," *IEEE Transactions on Power Electronics*, vol. 22, no. 5, pp. 1919–1927, 2007.

[16] D. De and V. Ramanarayanan, "Decentralized parallel operation of inverters sharing unbalanced and nonlinear loads," *IEEE Transactions on Power Electronics*, vol. 25, no. 12, pp. 3015–3025, 2010.

[17] M. Hamzeh, H. Karimi, and H. Mokhtari, "Harmonic and negative-sequence current control in an islanded multi-bus mv microgrid," *IEEE Transactions on Smart Grid*, vol. 5, no. 1, pp. 167–176, 2014.

[18] M. S. Golsorkhi, M. Savaghebi, D. D.-C. Lu, J. M. Guerrero, and J. C. Vasquez, "A gps-based control framework for accurate current sharing and power quality improvement in microgrids," *IEEE Transactions on Power Electronics*, vol. 32, no. 7, pp. 5675–5687, 2017.

[19] J. He, Y. W. Li, and F. Blaabjerg, "An enhanced islanding microgrid reactive power, imbalance power, and harmonic power sharing scheme," *IEEE Transactions on Power Electronics*, vol. 30, no. 6, pp. 3389–3401, 2015.

[20] P. Sreekumar and V. Khadkikar, "A new virtual harmonic impedance scheme for harmonic power sharing in an islanded microgrid," *IEEE Transactions on Power Delivery*, vol. 31, no. 3, pp. 936–945, 2016.

[21] M. B. Delghavi and A. Yazdani, "Islanded-mode control of electronically coupled distributed-resource units under unbalanced and nonlinear load conditions," *IEEE Transactions on Power Delivery*, vol. 26, no. 2, pp. 661–673, 2011.

[22] T. Vandoorn, B. Meersman, J. De Kooning, and L. Vandevelde, "Controllable harmonic current sharing in islanded microgrids: Dg units with programmable resistive behavior toward harmonics," *IEEE Transactions on Power Delivery*, vol. 27, no. 2, pp. 831–841, 2012.

[23] X. Wang, F. Blaabjerg, and Z. Chen, "Autonomous control of inverter-interfaced distributed generation units for harmonic current filtering and resonance damping in an islanded microgrid," *IEEE Transactions on Industry Applications*, vol. 50, no. 1, pp. 452–461, 2014.

[24] P. S. Georgilakis and N. D. Hatziargyriou, "Optimal distributed generation placement in power distribution networks: models, methods, and future research," *IEEE Transactions on power systems*, vol. 28, no. 3, pp. 3420–3428, 2013.

[25] M. A. Azzouz and E. El-Saadany, "Multivariable dg impedance modeling and reshaping for impedance stabilization of active distribution networks," *IEEE Transactions on Smart Grid*, 2016.

[26] P. S. Georgilakis and N. D. Hatziargyriou, "A review of power distribution planning in the modern power systems era: Models, methods and future research," *Electric Power Systems Research*, vol. 121, pp. 89–100, 2015.

[27] A. Piccolo and P. Siano, "Evaluating the Impact of Network Investment Deferral on Distributed Generation Expansion," *IEEE Transactions on Power Systems*, vol. 24, no. 3, pp. 1559–1567, 2009.

[28] D. T. Wang, L. F. Ochoa, and G. P. Harrison, "DG impact on investment deferral: Network planning and security of supply," *IEEE Transactions on Power Systems*, vol. 25, no. 2, pp. 1134–1141, 2010.

[29] D. Q. Hung, N. Mithulananthan, and R. C. Bansal, "Analytical expressions for DG allocation in primary distribution networks," *IEEE Transactions on Energy Conversion*, vol. 25, no. 3, pp. 814–820, 2010.

[30] L. F. Ochoa, A. Padilha-Feltrin, and G. P. Harrison, "Evaluating distributed generation impacts with a multiobjective index," *IEEE Transactions on Power Delivery*, vol. 21, no. 3, pp. 1452–1458, 2006.

[31] Y. M. Atwa, E. F. El-Saadany, M. M. A. Salama, and R. Seethapathy, "Optimal Renewable Resources Mix for Distribution System Energy Loss Minimization," *IEEE Transactions on Power Systems*, vol. 25, no. 1, pp. 360–370, 2010.

[32] I. Ziari, G. Ledwich, A. Ghosh, and G. Platt, "Optimal distribution network reinforcement considering load growth, line loss, and reliability," *IEEE Transactions on Power Systems*, vol. 28, no. 2, pp. 587–597, 2013.

[33] G. Munoz-Delgado, J. Contreras, and J. M. Arroyo, "Joint expansion planning of distributed generation and distribution networks," *IEEE Transactions on Power Systems*, vol. 30, no. 5, pp. 2579–2590, 2015.

[34] M. Alotaibi and M. Salama, "An Incentive-Based Multistage Expansion Planning Model for Smart Distribution Systems," *IEEE Transactions on Power Systems*, vol. 8950, no. c, 2018.

[35] A. Kumar and W. Gao, "Optimal distributed generation location using mixed integer non-linear programming in hybrid electricity markets," *IET Generation, Transmission & Distribution*, vol. 4, no. 2, p. 281, 2010.

[36] A. Keane and M. O'Malley, "Optimal Allocation of Embedded Generation on Distribution Networks," *IEEE Transactions on Power Systems*, vol. 20, no. 3, pp. 1640–1646, 2005.

[37] A. Ameli, S. Member, S. Bahrami, S. Member, and F. Khazaeli, "A Multiobjective Particle Swarm Optimization for Sizing and Placement of DGs from DG Owner ' s and Distribution Company ' s Viewpoints," vol. 29, no. 4, pp. 1–10, 2014.

[38] M. Heydari, S. Hosseini, and S. Gholamian, "Optimal Placement and Sizing of Capacitor and Distributed Generation with Harmonic and Resonance Considerations Using Discrete Particle Swarm Optimization," *International Journal of Intelligent Systems and Applications*, vol. 5, no. 7, pp. 42–49, 2013.

[39] IEEE Standard 1547.4, "IEEE guide for design, operation, and integration of distributed resource island systems with electric power systems," 2011.

[40] Y. A. Katsigiannis, P. S. Georgilakis, and E. S. Karapidakis, "Hybrid simulated annealing–tabu search method for optimal sizing of autonomous power systems with renewables," *IEEE Transactions on Sustainable Energy*, vol. 3, no. 3, pp. 330–338, 2012.

[41] "Caledonian Technical Reference for IEC 60502 Low Voltage Cables. [Online]. Available:," http://www.caledoniancables.co.uk/Product/IEC60502/Technical%20Reference.html., accessed: 10-Sep-2016.

[42] B. Zhao, X. Zhang, P. Li, K. Wang, M. Xue, and C. Wang, "Optimal sizing, operating strategy and operational experience of a stand-alone microgrid on dongfushan island," *Applied Energy*, vol. 113, pp. 1656–1666, 2014.

[43] T. Ersal, C. Ahn, D. L. Peters, J. W. Whitefoot, A. R. Mechtenberg, I. A. Hiskens, H. Peng, A. G. Stefanopoulou, P. Y. Papalambros, and J. L. Stein, "Coupling between component sizing and regulation capability in microgrids," *IEEE Transactions on Smart Grid*, vol. 4, no. 3, pp. 1576–1585, 2013.

[44] H. E. Farag and E. F. El-Saadany, "Optimum shunt capacitor placement in multi-microgrid systems with consideration of islanded mode of operation," *IEEE Transactions on Sustainable Energy*, vol. 6, no. 4, pp. 1435–1446, 2015.

[45] E. Hajipour, M. Bozorg, and M. Fotuhi-Firuzabad, "Stochastic capacity expansion planning of remote microgrids with wind farms and energy storage," *IEEE transactions on sustainable energy*, vol. 6, no. 2, pp. 491–498, 2015.

[46] D. E. Olivares, A. Mehrizi-Sani, A. H. Etemadi, C. A. Cañizares, R. Iravani, M. Kazerani, A. H. Hajimiragha, O. Gomis-Bellmunt, M. Saeedifard, R. Palma-Behnke

et al., "Trends in microgrid control," *IEEE Transactions on smart grid*, vol. 5, no. 4, pp. 1905–1919, 2014.

[47] A. A. Eajal and M. El-Hawary, "Optimal capacitor placement and sizing in unbalanced distribution systems with harmonics consideration using particle swarm optimization," *IEEE Transactions on Power Delivery*, vol. 25, no. 3, pp. 1734–1741, 2010.

[48] B. R. Pereira, G. R. M. da Costa, J. Contreras, and J. R. S. Mantovani, "Optimal distributed generation and reactive power allocation in electrical distribution systems," *IEEE Transactions on Sustainable Energy*, vol. 7, no. 3, pp. 975–984, 2016.

[49] J. Xiao, L. Bai, F. Li, H. Liang, and C. Wang, "Sizing of energy storage and diesel generators in an isolated microgrid using discrete fourier transform (dft)," *IEEE Transactions on Sustainable Energy*, vol. 5, no. 3, pp. 907–916, 2014.

[50] M. Arriaga, C. A. Caizares, and M. Kazerani, "Long-term renewable energy planning model for remote communities," *IEEE Transactions on Sustainable Energy*, vol. 7, no. 1, pp. 221–231, 2016.

[51] E. Karimi and M. Kazerani, "A Generalized Platform for Optimal Planning of Isolated Microgrids, Considering Operation Constraints," in *IECON 2018-44th Annual Conference of the IEEE Industrial Electronics Society*. IEEE, 2018, pp. 1589–1596.

[52] A. Ehsan and Q. Yang, "Coordinated investment planning of distributed multi-type stochastic generation and battery storage in active distribution networks," *IEEE Transactions on Sustainable Energy*, 2018.

[53] S. Mohamed, M. F. Shaaban, M. Ismail, E. Serpedin, and K. A. Qaraqe, "An efficient planning algorithm for hybrid remote microgrids," *IEEE Transactions on Sustainable Energy*, vol. 10, no. 1, pp. 257–267, 2018.

[54] H. Alharbi and K. Bhattacharya, "Stochastic optimal planning of battery energy storage systems for isolated microgrids," *IEEE Transactions on Sustainable Energy*, vol. 9, no. 1, pp. 211–227, 2017.

[55] S. Mashayekh, M. Stadler, G. Cardoso, M. Heleno, S. C. Madathil, H. Nagarajan, R. Bent, M. Mueller-Stoffels, X. Lu, and J. Wang, "Security-constrained design of isolated multi-energy microgrids," *IEEE Transactions on Power Systems*, vol. 33, no. 3, pp. 2452–2462, 2017.

[56] A. A. Abdelsalam and E. F. El-Saadany, "Probabilistic approach for optimal planning of distributed generators with controlling harmonic distortions," *IET Generation, Transmission & Distribution*, vol. 7, no. 10, pp. 1105–1115, 2013.

[57] V. R. Pandi, H. Zeineldin, and W. Xiao, "Determining optimal location and size of distributed generation resources considering harmonic and protection coordination limits," *IEEE Transactions on Power Systems*, vol. 28, no. 2, pp. 1245–1254, 2013.

[58] Y. Song, X. Wang, and F. Blaabjerg, "High-frequency resonance damping of DFIG-based wind power system under weak network," *IEEE Transactions on Power Electronics*, vol. 32, no. 3, pp. 1927–1940, 2017.

[59] F. Wang, J. L. Duarte, M. A. Hendrix, and P. F. Ribeiro, "Modeling and analysis of grid harmonic distortion impact of aggregated DG inverters," *IEEE Transactions on Power Electronics*, vol. 26, no. 3, pp. 786–797, 2011.

[60] A. Medina, J. Segundo-Ramirez, P. Ribeiro, W. Xu, K. Lian, G. Chang, V. Dinavahi, and N. Watson, "Harmonic analysis in frequency and time domain," *IEEE Transactions on power delivery*, vol. 28, no. 3, pp. 1813–1821, 2013.

[61] T. Force and G. Chang, "Characteristics and modeling of harmonic sources-power electronic devices," *IEEE Power Engineering Review*, vol. 21, no. 8, pp. 62–63, 2001.

[62] E. Fuchs and M. A. Masoum, *Power quality in power systems and electrical machines*. Academic press, 2011, ch. 7.

[63] M. Valcarel and J. G. Mayordomo, "Harmonic power flow for unbalanced systems," *IEEE Transactions on Power Delivery*, vol. 8, no. 4, pp. 2052–2059, 1993.

[64] D. Xia and G. T. Heydt, "Harmonic power flow studies part i-formulation and solution," *IEEE Transactions on Power Apparatus and systems*, no. 6, pp. 1257–1265, 1982.

[65] S. Herraiz, L. Sainz, and J. Clua, "Review of harmonic load flow formulations," *IEEE Transactions on Power Delivery*, vol. 18, no. 3, pp. 1079–1087, 2003.

[66] B. Smith and J. Arrillaga, "Power flow constrained harmonic analysis in ac-dc power systems," *IEEE Transactions on Power Systems*, vol. 14, no. 4, pp. 1251–1261, 1999.

[67] Y. Sun, C. Dai, J. Li, and J. Yong, "Frequency-domain harmonic matrix model for three-phase diode-bridge rectifier," *IET Generation, Transmission & Distribution*, vol. 10, no. 7, pp. 1605–1614, 2016.

[68] K. Lee, G. Venkataramanan, and T. M. Jahns, "Source current harmonic analysis of adjustable speed drives under input voltage unbalance and sag conditions," *IEEE Transactions on power delivery*, vol. 21, no. 2, pp. 567–576, 2006.

[69] N. Mohan and T. M. Undeland, *Power electronics: converters, applications, and design*. John Wiley & Sons, 2007.

[70] P. Ladoux, G. Postiglione, H. Foch, and J. Nuns, "A comparative study of ac/dc converters for high-power dc arc furnace," *IEEE Transactions on Industrial Electronics*, vol. 52, no. 3, pp. 747–757, 2005.

[71] M. E. Haque, M. Negnevitsky, and K. M. Muttaqi, "A novel control strategy for a variable-speed wind turbine with a permanent-magnet synchronous generator," *IEEE Transactions on Industry Applications*, vol. 46, no. 1, pp. 331–339, Jan 2010.

[72] T. S. Parker and L. Chua, *Practical numerical algorithms for chaotic systems*. Springer Science & Business Media, 2012.

[73] M. Chen, Z. Qian, and X. Yuan, "Frequency-domain analysis of uncontrolled rectifiers," in *Applied Power Electronics Conference and Exposition, 2004. APEC'04. Nineteenth Annual IEEE*, vol. 2. IEEE, 2004, pp. 804–809.

[74] J. G. Mayordomo, Á. Carbonero, L. F. Beites, R. Asensi, and W. Xu, "A contribution towards a general and systematic procedure for modeling line commutated ac/dc converters in the harmonic domain," *IEEE Transactions on Power Delivery*, vol. 24, no. 4, pp. 2415–2427, 2009.

[75] M. Sakui and H. Fujita, "An analytical method for calculating harmonic currents of a three-phase diode-bridge rectifier with dc filter," *IEEE transactions on Power Electronics*, vol. 9, no. 6, pp. 631–637, 1994.

[76] G. Carpinelli, F. Iacovone, A. Russo, P. Varilone, and P. Verde, "Analytical modeling for harmonic analysis of line current of vsi-fed drives," *IEEE Transactions on Power Delivery*, vol. 19, no. 3, pp. 1212–1224, 2004.

[77] K. Lian, B. K. Perkins, and P. Lehn, "Harmonic analysis of a three-phase diode bridge rectifier based on sampled-data model," *IEEE Transactions on Power Delivery*, vol. 23, no. 2, pp. 1088–1096, 2008.

[78] Y. Sun, G. Zhang, W. Xu, and J. G. Mayordomo, "A harmonically coupled admittance matrix model for ac/dc converters," *IEEE Transactions on Power Systems*, vol. 22, no. 4, pp. 1574–1582, 2007.

[79] J. Yong, L. Chen, and S. Chen, "Modeling of home appliances for power distribution system harmonic analysis," *IEEE Transactions on Power Delivery*, vol. 25, no. 4, pp. 3147–3155, 2010.

[80] N. Zhou, J. Wang, Q. Wang, and N. Wei, "Measurement-based harmonic modeling of an electric vehicle charging station using a three-phase uncontrolled rectifier," *IEEE Transactions on Smart Grid*, vol. 6, no. 3, pp. 1332–1340, 2015.

[81] Z. Bing, K. J. Karimi, and J. Sun, "Input impedance modeling and analysis of line-commutated rectifiers," *IEEE Transactions on Power Electronics*, vol. 24, no. 10, pp. 2338–2346, 2009.

[82] H. Atighechi, S. Chiniforoosh, S. Ebrahimi, and J. Jatskevich, "Using multiple reference frame theory for considering harmonics in average-value modeling of diode rectifiers," *IEEE Transactions on Energy Conversion*, vol. 31, no. 3, pp. 872–881, 2016.

[83] J. G. Mayordomo, L. F. Beites, Á. Carbonero, X. Yang, and W. Xu, "An analytical procedure for calculating harmonics of three-phase uncontrolled rectifiers under non-ideal conditions," *IEEE Transactions on Power Delivery*, vol. 30, no. 1, pp. 144–152, 2015.

[84] J. G. Mayordomo, L. F. Beites, X. Yang, and W. Xu, "A detailed procedure for harmonic analysis of three-phase diode rectifiers under discontinuous conduction mode and nonideal conditions," *IEEE Transactions on Power Delivery*, vol. 33, no. 2, pp. 741–751, 2018.

[85] P. Lehn and K. Lian, "Frequency coupling matrix of a voltage-source converter derived from piecewise linear differential equations," *IEEE Transactions on Power Delivery*, vol. 22, no. 3, pp. 1603–1612, 2007.

[86] J. M. Guerrero, L. G. De Vicuña, J. Matas, M. Castilla, and J. Miret, "Output impedance design of parallel-connected ups inverters with wireless load-sharing control," *IEEE Transactions on industrial electronics*, vol. 52, no. 4, pp. 1126–1135, 2005.

[87] M. Savaghebi, A. Jalilian, J. C. Vasquez, and J. M. Guerrero, "Autonomous voltage unbalance compensation in an islanded droop-controlled microgrid," *IEEE Transactions on Industrial Electronics*, vol. 60, no. 4, pp. 1390–1402, 2013.

[88] J. He, Y. W. Li, F. Blaabjerg, and X. Wang, "Active harmonic filtering using current-controlled, grid-connected dg units with closed-loop power control," *IEEE Transactions on Power Electronics*, vol. 29, no. 2, pp. 642–653, 2014.

[89] K. Lian and P. Lehn, "Steady-state solution of a voltage-source converter with full closed-loop control," *IEEE Transactions on Power Delivery*, vol. 21, no. 4, pp. 2071–2081, 2006.

[90] K. L. Lian and P. Lehn, "Steady-state simulation methods of closed-loop power converter systems—a systematic solution procedure," *IEEE Transactions on Circuits and Systems I: Regular Papers*, vol. 59, no. 6, pp. 1299–1311, 2012.

[91] A. A. Van Der Meer, M. Ndreko, M. Gibescu, and M. A. van der Meijden, "The effect of frt behavior of vsc-hvdc-connected offshore wind power plants on ac/dc system dynamics," *IEEE Transactions on Power Delivery*, vol. 31, no. 2, pp. 878–887, 2016.

[92] P. Lehn, "Exact modeling of the voltage source converter," *IEEE Transactions on Power Delivery*, vol. 17, no. 1, pp. 217–222, 2002.

[93] M. M. A. Abdelaziz, H. E. Farag, E. F. El-Saadany, and Y. A.-R. I. Mohamed, "A novel and generalized three-phase power flow algorithm for islanded microgrids using a newton trust region method," *IEEE Transactions on Power Systems*, vol. 28, no. 1, pp. 190–201, 2013.

[94] F. Mumtaz, M. Syed, M. Al Hosani, and H. Zeineldin, "A novel approach to solve power flow for islanded microgrids using modified newton raphson with droop control of dg," *IEEE Transactions on Sustainable Energy*, vol. 7, no. 2, pp. 493–503, 2016.

[95] A. Eajal, M. A. Abdelwahed, E. El-Saadany, and K. Ponnambalam, "A unified approach to the power flow analysis of ac/dc hybrid microgrids," *IEEE Transactions on Sustainable Energy*, vol. 7, no. 3, pp. 1145–1158, 2016.

[96] A. A. Hamad, M. A. Azzouz, and E. F. El Saadany, "A sequential power flow algorithm for islanded hybrid ac/dc microgrids," *IEEE Transactions on Power Systems*, vol. 31, no. 5, pp. 3961–3970, 2016.

[97] J. Wang, J. Yan, Y. Xu, and K. Huang, "Power flow calculation method for isolated microgrid considering the influence of harmonic power," *The Journal of Engineering*, vol. 2017, no. 14, pp. 2615–2621, 2017.

[98] "519-2014-ieee recommended practice and requirements for harmonic control in electric power systems," *IEEE Std 519-2014*, pp. 1–29, 2014.

[99] "Electromagnetic compatibility (EMC) - Part 3-4: Limits - Limitation of emission of harmonic currents in low-voltage power supply systems for equipment with rated current greater than 16 A, IEC Standard 61000-3-4:1998."

[100] "Electromagnetic compatibility (EMC) - Part 2-2: Environment - Compatibility levels for low-frequency conducted disturbances and signalling in public low-voltage power supply systems, IEC Standard 61000-2-2:2002."

[101] "Ieee standard definitions for the measurement of electric power quantities under sinusoidal, nonsinusoidal, balanced, or unbalanced conditions," *IEEE Std 1459-2010*, pp. 1–50, March 2010.

[102] "Power cables with extruded insulation and their accessories for rated voltages from 1 kV (Um= 1,2 kV) up to 30 kV (Um= 36 kV) – Part 1: Cables for rated voltages of 1 kV ((Um= 1,2 kV) and 3 kV (Um= 3,6 kV), IEC Standard 60502-1:2004."

[103] P. Rodríguez, A. Luna, I. Candela, R. Mujal, R. Teodorescu, and F. Blaabjerg, "Multiresonant frequency-locked loop for grid synchronization of power converters under distorted grid conditions," *IEEE Transactions on Industrial Electronics*, vol. 58, no. 1, pp. 127–138, 2011.

[104] J. Matas, M. Castilla, J. Miret, L. G. de Vicuña, and R. Guzman, "An adaptive prefiltering method to improve the speed/accuracy tradeoff of voltage sequence detection methods under adverse grid conditions," *IEEE Transactions on Industrial Electronics*, vol. 61, no. 5, pp. 2139–2151, 2014.

[105] Y. F. Wang and Y. W. Li, "Three-phase cascaded delayed signal cancellation pll for fast selective harmonic detection," *IEEE Transactions on Industrial Electronics*, vol. 60, no. 4, pp. 1452–1463, 2013.

[106] R. Teodorescu, F. Blaabjerg, U. Borup, and M. Liserre, "A new control structure for grid-connected lcl pv inverters with zero steady-state error and selective harmonic compensation," in *Applied Power Electronics Conference and Exposition, 2004. APEC'04. Nineteenth Annual IEEE*, vol. 1. IEEE, 2004, pp. 580–586.

[107] M. A. Azzouz and E. F. El-Saadany, "Multivariable grid admittance identification for impedance stabilization of active distribution networks," *IEEE Transactions on Smart Grid*, vol. 8, no. 3, pp. 1116–1128, 2017.

[108] J.-N. Paquin, C. Dufour, and J. Bélanger, "A hardware-in-the-loop simulation platform for prototyping and testing of wind generator controllers," in *CIGRÉ Canada Conference on Power Systems Winnipeg*, 2008.

[109] A. Yamane, W. Li, J. Bélanger, T. Ise, I. Iyoda, T. Aizono, and C. Dufour, "A smart distribution grid laboratory," in *IECON 2011-37th Annual Conference on IEEE Industrial Electronics Society*. IEEE, 2011, pp. 3708–3712.

[110] O. Crăciun, A. Florescu, I. Munteanu, A. I. Bratcu, S. Bacha, and D. Radu, "Hardware-in-the-loop simulation applied to protection devices testing," *International Journal of Electrical Power & Energy Systems*, vol. 54, pp. 55–64, 2014.

[111] C. Dufour and J. Bélanger, "On the use of real-time simulation technology in smart grid research and development," *IEEE Transactions on Industry Applications*, vol. 50, no. 6, pp. 3963–3970, 2014.

[112] G. M. Masters, *Renewable and efficient electric power systems*. John Wiley & Sons, 2013.

[113] Y. Li, D. M. Vilathgamuwa, and P. C. Loh, "Design, analysis, and real-time testing of a controller for multibus microgrid system," *IEEE Transactions on power electronics*, vol. 19, no. 5, pp. 1195–1204, 2004.

[114] H. Mahmood, D. Michaelson, and J. Jiang, "Accurate reactive power sharing in an islanded microgrid using adaptive virtual impedances," *IEEE Transactions on Power Electronics*, vol. 30, no. 3, pp. 1605–1617, 2014.

[115] NERC Standard, "TOP-004–2: Transmission Operations," *North American Electric Reliability Corporation*, 2007.

[116] S. A. Arefifar, Y. A.-R. I. Mohamed, and T. El-Fouly, "Optimized multiple microgrid-based clustering of active distribution systems considering communication and control requirements," *IEEE Transactions on Industrial Electronics*, vol. 62, no. 2, pp. 711–723, 2014.

[117] P. CODE and C. PRIX, "Electromagnetic compatibility (EMC)–Part 3-7: Limits–Assessment of emission limits for the connection of fluctuating installations to MV, HV and EHV power systems," 2008.

[118] Y. Song, X. Wang, and F. Blaabjerg, "Impedance-based high-frequency resonance analysis of DFIG system in weak grids," *IEEE Transactions on Power Electronics*, vol. 32, no. 5, pp. 3536–3548, 2016.

[119] Z. Miao, "Impedance-model-based SSR analysis for type 3 wind generator and series-compensated network," *IEEE Transactions on Energy Conversion*, vol. 27, no. 4, pp. 984–991, 2012.

[120] P. Krause, O. Wasynczuk, S. Sudhoff, and S. Pekarek, *Analysis of electric machinery and drive systems*. Wiley, 2013.

[121] P. Vas, *Sensorless vector and direct torque control*. Oxford Univ. Press, 1998.

[122] Y. Song and F. Blaabjerg, "Wide frequency band active damping strategy for DFIG system high frequency resonance," *IEEE Transactions on Energy Conversion*, vol. 31, no. 4, pp. 1665–1675, 2016.

[123] M. A. Alotaibi and M. M. Salama, "An incentive-based multistage expansion planning model for smart distribution systems," *IEEE Transactions on Power Systems*, vol. 33, no. 5, pp. 5469–5485, 2018.

[124] Task Force, "The IEEE Reliability Test System," *IEEE Transactions on Power Systems*, vol. 14, no. 3, pp. 1010–1020, Aug 1999.

[125] A. A. Hamad, M. E. Nassar, E. F. El-Saadany, and M. Salama, "Optimal configuration of isolated hybrid AC/DC microgrids," *IEEE Transactions on Smart Grid*, vol. 10, no. 3, pp. 2789–2798, 2018.

[126] H. M. Ahmed, A. B. Eltantawy, and M. M. Salama, "A planning approach for the network configuration of AC-DC hybrid distribution systems," *IEEE Transactions on Smart Grid*, vol. 9, no. 3, pp. 2203–2213, 2016.

[127] M. F. Shaaban, S. Mohamed, M. Ismail, K. A. Qaraqe, and E. Serpedin, "Joint planning of smart EV charging stations and DGs in Eco-friendly remote hybrid microgrids," *IEEE Transactions on Smart Grid*, vol. 10, no. 5, pp. 5819–5830, 2019.

[128] M. E. Baran and F. F. Wu, "Optimal capacitor placement on radial distribution systems," *IEEE Transactions on power Delivery*, vol. 4, no. 1, pp. 725–734, 1989.

[129] R. Abu-Hashim, R. Burch, G. Chang, M. Grady, E. Gunther, M. Halpin, C. Harziadonin, Y. Liu, M. Marz, T. Ortmeyer, V. Rajagopalan, S. Ranade, P. Ribeiro, T. Sim, and W. Xu, "Test systems for harmonics modeling and simulation," *IEEE Transactions on Power Delivery*, vol. 14, no. 2, pp. 579–587, April 1999.

[130] A. Bonner, T. Grebe, E. Gunther, L. Hopkins, M. Marz, J. Mahseredjian, N. Miller, T. Ortmeyer, V. Rajagopalan, S. Ranade *et al.*, "Modeling and simulation of the propagation of harmonics in electric power networks. 1. concepts, models, and simulation techniques," *IEEE Transactions on Power Delivery*, vol. 11, no. 1, pp. 452–465, 1996.

[131] Y. Sun, G. Zhang, W. Xu, and J. G. Mayordomo, "A non-iterative harmonic power flow method for accurate harmonic calculations," in *Harmonics and Quality of Power, 2008. ICHQP 2008. 13th International Conference on.* IEEE, 2008, pp. 1–6.

[132] M. H. Rashid, *Power electronics handbook.* Butterworth-Heinemann, 2017.

[133] R. Ridley, "Second-Stage LC Filter Design," *Switching Power Magazine*, vol. 9, pp. 14–20, 2000.

[134] A. Koran, K. Sano, R.-Y. Kim, and J.-S. Lai, "Design of a photovoltaic simulator with a novel reference signal generator and two-stage LC output filter," *IEEE Transactions on Power Electronics*, vol. 25, no. 5, pp. 1331–1338, 2010.

[135] M. Grotzbach and R. Redmann, "Line current harmonics of VSI-fed adjustable-speed drives," *IEEE Transactions on Industry Applications*, vol. 36, no. 2, pp. 683–690, 2000.

[136] M. H. Moradi and M. Abedini, "A combination of genetic algorithm and particle swarm optimization for optimal dg location and sizing in distribution systems," *International Journal of Electrical Power & Energy Systems*, vol. 34, no. 1, pp. 66–74, 2012.

[137] "Caledonian Technical Reference for IEC 60502 Low Voltage Cables. [Online]. Available:," http://www.caledonian-cables.co.uk/Product/IEC60502/Technical%20Reference.html., accessed: 16-May-2019.

[138] S. Chiniforoosh, H. Atighechi, A. Davoudi, J. Jatskevich, A. Yazdani, S. Filizadeh, M. Saeedifard, J. Martinez, V. Sood, K. Strunz *et al.*, "Dynamic average modeling of front-end diode rectifier loads considering discontinuous conduction mode and unbalanced operation," *IEEE Transactions on Power Delivery*, vol. 27, no. 1, pp. 421–429, 2012.

[139] G. Sewell, *Computational methods of linear algebra.* World Scientific Publishing Company, 2014.

[140] E. W. Cheney and D. R. Kincaid, *Numerical mathematics and computing*. Cengage Learning, 2012.

[141] S. Tripathy, G. D. Prasad, O. Malik, and G. Hope, "Load-flow solutions for ill-conditioned power systems by a newton-like method," *IEEE Transactions on Power apparatus and Systems*, no. 10, pp. 3648–3657, 1982.

[142] "MATLAB. [Online]. Available:," https://www.mathworks.com/help/symbolic/digits.html, accessed: 8-May-2019.

[143] R. Torquato, Q. Shi, W. Xu, and W. Freitas, "A monte carlo simulation platform for studying low voltage residential networks," *IEEE Transactions on Smart Grid*, vol. 5, no. 6, pp. 2766–2776, 2014.

[144] J. Molina and L. Sainz, "Compact fluorescent lamp modeling for large-scale harmonic penetration studies," *IEEE Transactions on Power Delivery*, vol. 30, no. 3, pp. 1523–1531, 2015.

[145] R. Krishnan, *Electric motor drives: modeling, analysis and control*. Prentice Hall, 2001.

[146] R. T. Force, "The ieee reliability test system-1996," *IEEE Trans. Power Syst*, vol. 14, no. 3, pp. 1010–1020, 1999.

[147] E. Karimi, "A generalized optimal planning platform for microgrids of remote communities considering frequency and voltage regulation constraints," *PhD Thesis, University of Waterloo*, 2017.

[148] A. Khodaei and M. Shahidehpour, "Microgrid-based co-optimization of generation and transmission planning in power systems," *IEEE Transactions on Power Systems*, vol. 28, no. 2, pp. 1582–1590, 2013.

[149] A. Khodaei, S. Bahramirad, and M. Shahidehpour, "Microgrid planning under uncertainty," *IEEE Transactions on Power Systems*, vol. 30, no. 5, pp. 2417–2425, 2015.

[150] M. Yilmaz and P. T. Krein, "Review of the impact of vehicle-to-grid technologies on distribution systems and utility interfaces," *IEEE Transactions on power electronics*, vol. 28, no. 12, pp. 5673–5689, 2013.

[151] G. Heydt, "Thevenin's theorem applied to the analysis of polyphase transmission circuits," *IEEE Transactions on Power Delivery*, vol. 32, no. 1, pp. 72–77, 2017.

[152] A. T. Eseye, M. Lehtonen, T. Tukia, S. Uimonen, and R. J. Millar, "Optimal energy trading for renewable energy integrated building microgrids containing electric vehicles and energy storage batteries," *IEEE Access*, vol. 7, pp. 106 092–106 101, 2019.

[153] E. Ebrahimzadeh, F. Blaabjerg, X. Wang, and C. L. Bak, "Efficient approach for harmonic resonance identification of large wind power plants," in *Power Electronics for Distributed Generation Systems (PEDG), 2016 IEEE 7th International Symposium on*. IEEE, 2016, pp. 1–7.

[154] J. G. Mayordomo, L. Beites, R. Asensi, F. Orzaez, M. Izzeddine, and L. Zabala, "A contribution for modeling controlled and uncontrolled ac/dc converters in harmonic power flows," *IEEE transactions on Power Delivery*, vol. 13, no. 4, pp. 1501–1508, 1998.

[155] Y.-S. Tzeng, "Harmonic analysis of parallel-connected 12-pulse uncontrolled rectifier without an interphase transformer," *IEE Proceedings-Electric Power Applications*, vol. 145, no. 3, pp. 253–260, 1998.

[156] S. Yang, J. Wang, and W. Yang, "A novel 24-pulse diode rectifier with an auxiliary single-phase full-wave rectifier at dc side," *IEEE Transactions on Power Electronics*, vol. 32, no. 3, pp. 1885–1893, 2017.

[157] A. Conn, N. Gould, and P. Toint, "Trust region methods. mps-siam series on optimization, siam," *Google Scholar*, 2000.

[158] D. Basic, "Input current interharmonics of variable-speed drives due to motor current imbalance," *IEEE Transactions on Power Delivery*, vol. 25, no. 4, pp. 2797–2806, 2010.

[159] W. Gao, E. Solodovnik, R. Dougal, G. Cokkinides, and A. S. Meliopoulos, "Elimination of numerical oscillations in power system dynamic simulation," in *Eighteenth Annual IEEE Applied Power Electronics Conference and Exposition, 2003. APEC'03.*, vol. 2. IEEE, 2003, pp. 790–794.

[160] J. Arrillaga and C. Arnold, "Computer analysis of power systems," 1990.

[161] L. Brancik, "Techniques of matrix exponential function derivative for electrical engineering simulations," in *2006 IEEE International Conference on Industrial Technology*. IEEE, 2006, pp. 2608–2613.

[162] C. Van Loan, "Computing integrals involving the matrix exponential," *IEEE transactions on automatic control*, vol. 23, no. 3, pp. 395–404, 1978.

[163] D. O. Boillat, T. Friedli, J. Mühlethaler, J. W. Kolar, and W. Hribernik, "Analysis of the design space of single-stage and two-stage lc output filters of switched-mode ac power sources," in *2012 IEEE Power and Energy Conference at Illinois*. IEEE, 2012, pp. 1–8.

[164] V. Vlatkovic, D. Borojevic, and F. C. Lee, "Input filter design for power factor correction circuits," *IEEE Transactions on Power Electronics*, vol. 11, no. 1, pp. 199–205, 1996.

[165] A. T. Eseye, D. Zheng, H. Li, and J. Zhang, "Grid-price dependent optimal energy storage management strategy for grid-connected industrial microgrids," in *2017 Ninth Annual IEEE Green Technologies Conference (GreenTech)*. IEEE, 2017, pp. 124–131.

[166] K. Lian and T. Huang, "Admittance matrices of voltage source converters for distributed generators," in *2014 International Power Electronics Conference (IPEC-Hiroshima 2014-ECCE ASIA)*. IEEE, 2014, pp. 2195–2201.

APPENDICES

Appendix A

Chapter 3 Parameters

The parameters of the test microgrid used in Chapter 3 are listed in Table A.1.

Table A.1: Microgrid Parameters.

Feeders: $L_1 = 25\ \mu$H, $R_1 = 0.35\ \Omega$, $L_2 = 225\ \mu$H, $R_2 = 0.25\ \Omega$,
Common Load: $I_3 = 18.2$ A, $I_5 = 13.6$ A, $I_7 = 9.1$ A, $I_9 = 6.4$ A $I_{11} = 5.6$ A
Local Load: Bridge rectifier with $L = 0.2$ H, $R = 19.6\ \Omega$
DG Ratings: 5 kVA, Single-Phase, 220 V, 60 Hz
DG Interfacing Filter: $L_f = 1$ mH, $R_f = 0.1\ \Omega$, $C_f = 20\ \mu$F
PR Controllers: $\omega_{cut,h} = 1.0$, $K_{rh} = 2000$, $K_{pv} = 12$, $K_D = 60$
***ω*−*P* and *V*−*Q* Droop Characteristics:** $D_p = 0.001$, $D_q = 0.005$, $L_{v1} = 4.5$ mH, $R_{v1} = 0.1\ \Omega$

G_h–I_h Droop Characteristics

h	**3**	**5**	**7**	**9**	**11**
$G^{min}_{DG,h,i}$	1.4	1	0.8	0.6	0.5
$G^{max}_{DG,h,1}$	2.6	2.6	2.3	1.7	1.5

Appendix B

Chapter 4 Parameters

Nonlinear loads' harmonic spectrum and DFIG data used in Chapter 4 are listed in Tables B.1 and B.2, respectively.

Table B.1: Harmonic Spectrum for Nonlinear Loads

Harmonic Order	1	5	7	11	13	17	19
Magnitude (%)	100	4	4	2	2	1.5	1.5
Phase Angle	-5.00°	-55.68°	-84.11°	-143.56°	-175.58°	111.39°	68.30°
Harmonic Order	23	25	29	31	35	37	
Magnitude (%)	0.6	0.6	0.6	0.6	0.3	0.3	
Phase Angle	-24.61°	-67.64°	-145.46°	176.83°	97.40°	54.36°	

Table B.2: DFIG Data (All in P.U.)

L_g	0.1980	L_f	0.1980
C_f	0.0197	L_s	0.0923
L_m	3.9528	L'_{lr}	0.0996
r_s	0.0049	r'_r	0.0055
K_p	0.3361	K_i	8.4016
ω_r	1.2	F	0

Appendix C

Chapter 5 System Parameters

Test system parameters used in Chapter 5 are given in Tables C.1, C.2, and C.3.

Table C.1: Rectifiers with Single-Stage LC Filters

For DCM	For CCM
$L = 0.1\,mH$, $R = 9\,m\Omega$, $L_{dc} = 0.1\,mH$, $R_{dc} = 1\,m\Omega$, $C = 0.5\,mF$, $R_{inf} = 10^5\,\Omega$, $R_{off} = 10^8\,\Omega$, $R_{on} = 10^{-4}\,\Omega$, $R_l = 25\,\Omega$	$L = 2\,mH$, $R = 9\,m\Omega$, $L_{dc} = 2\,mH$, $R_{dc} = 0.5\,\Omega$, $C = 1\,mF$, $R_{inf} = 10^5\,\Omega$, $R_{off} = 10^8\,\Omega$, $R_{on} = 10^{-4}\,\Omega$, $R_l = 25\,\Omega$
$\omega = 2\pi 60\,rad/s$, $V_1 = 120\sqrt{2}\,V$, $V_{-1} = 0.03V_1$,$V_{-2} = 0.01V_1$, $V_4 = 0.015V_1$, $V_{-5} = 0.06V_1$, $V_7 = 0.05V_1$, $V_{-11} = 0.035V_1$, $V_{13} = 0.03V_1$	$\omega = 2\pi 60\,rad/s$, $V_1 = 120\sqrt{2}\,V$, $V_{-1} = 0.03V_1$, $V_{-2} = 0.025V_1$, $V_4 = 0.02V_1$, $V_{-5} = 0.06V_1$, $V_7 = 0.05V_1$, $V_{-11} = 0.035V_1$, $V_{13} = 0.03V_1$
$\phi_1 = 0°$, $\phi_{-1} = -40°$, $\phi_{-2} = -30°$, $\phi_4 = -20°$, $\phi_{-5} = 10°$, $\phi_7 = -30°$, $\phi_{-11} = 80°$, $\phi_{13} = -170°$	$\phi_1 = 0°$, $\phi_{-1} = -40°$, $\phi_{-2} = -30°$, $\phi_4 = -20°$, $\phi_{-5} = 10°$, $\phi_7 = -30°$, $\phi_{-11} = 80°$, $\phi_{13} = -170°$

Table C.2: Rectifiers with Two-Stage LC Filters

For DCM	For CCM
$L = 0.1\,mH$, $R = 9\,m\Omega$, $L_{dc,1} = 0.1\,mH$, $L_{dc,2} = 0.1\,mH$, $R_{dc,1} = 1\,m\Omega$, $R_{dc,2} = 1\,m\Omega$, $C_1 = 0.5\,mF$, $C_2 = 0.5\,mF$, $R_{inf} = 10^5\,\Omega$, $R_{off} = 10^8\,\Omega$, $R_{on} = 10^{-4}\,\Omega$, $R_l = 25\,\Omega$	$L = 2\,mH$, $R = 9\,m\Omega$, $L_{dc,1} = 1\,mH$, $L_{dc,2} = 1\,mH$, $R_{dc,1} = 0.25\,\Omega$, $R_{dc,2} = 0.25\,\Omega$, $C_1 = 0.5\,mF$, $C_2 = 0.5\,mF$, $R_{inf} = 10^5\,\Omega$, $R_{off} = 10^8\,\Omega$, $R_{on} = 10^{-4}\,\Omega$, $R_l = 25\,\Omega$
$\omega = 2\pi 60\,rad/s$, $V_1 = 120\sqrt{2}\,V$, $V_{-1} = 0.01V_1$, $V_{-2} = 0.01V_1$, $V_4 = 0.01V_1$, $V_{-5} = 0.06V_1$, $V_7 = 0.05V_1$, $V_{-11} = 0.035V_1$, $V_{13} = 0.03V_1$	$\omega = 2\pi 60\,rad/s$, $V_1 = 120\sqrt{2}\,V$, $V_{-1} = 0.03V_1$, $V_{-2} = 0.025V_1$, $V_4 = 0.02V_1$, $V_{-5} = 0.06V_1$, $V_7 = 0.05V_1$, $V_{-11} = 0.035V_1$, $V_{13} = 0.03V_1$
$\phi_1 = 0°$, $\phi_{-1} = -40°$, $\phi_{-2} = -30°$, $\phi_4 = -20°$, $\phi_{-5} = 10°$, $\phi_7 = -30°$, $\phi_{-11} = 80°$, $\phi_{13} = -170°$	$\phi_1 = 0°$, $\phi_{-1} = -40°$, $\phi_{-2} = -30°$, $\phi_4 = -20°$, $\phi_{-5} = 10°$, $\phi_7 = -30°$, $\phi_{-11} = 80°$, $\phi_{13} = -170°$

Table C.3: Rectifiers in Low X/R Ratio

$L = 3.4\,mH$, $R = 2.572\Omega$, $C = 2\,mF$, $R_{off} = 10^8\,\Omega$, $R_{on} = 10^{-4}\,\Omega$, $R_l = 140\,\Omega$
$\omega = 2\pi 60\,rad/s$, $V_1 = 120\sqrt{2}\,V$, $V_{-1} = 0.03V_1$, $V_{-2} = 0.025V_1$, $V_4 = 0.02V_1$, $V_{-5} = 0.06V_1$, $V_7 = 0.05V_1$, $V_{-11} = 0.035V_1$, $V_{13} = 0.03V_1$
$\phi_1 = 0°$, $\phi_{-1} = -40°$, $\phi_{-2} = -30°$, $\phi_4 = -20°$, $\phi_{-5} = 10°$, $\phi_7 = -30°$, $\phi_{-11} = 80°$, $\phi_{13} = -170°$

Appendix D

Chapter 6 System Parameters

Test system parameters used in Chapter 6 are given in Tables D.1 and D.2.

Table D.1: Lines' Parameters.

From bus	To bus	R_{line} (Ω)	X_{line} (Ω)
4	5	0.050	0.042
5	6	0.067	0.009
1	4	0.034	0.252
5	2	0.050	0.126
6	3	0.056	0.316

Table D.2: DGs' and Loads' Parameters.

Loads' Parameters:
1. Linear load: 38.25 kW and 5.93 kVAr.
2. Nonlinear Load: R=0.001 Ω, L=0.5 mH, C=1000 μF.
DGs' Parameters
1. Filter: L_f = 1 mH, R_f = 0.1 Ω, C_f = 20 μF.
2. Controller: a) Droop Gains: $m^P = 111\times10^{-6}$, $m^Q=1000\times10^{-6}$. b) Voltage Loop PR Controller: ω_{cut}=4 rad/s, K_i=200, K_p=5. c) Current Loop Controller: K_c=100.